MECHANICS OF CARBON NANOTUBES (CNTS) AND THEIR COMPOSITES

by

Huapei Wan

A dissertation submitted to the Graduate Faculty in Mechanical Engineering in partial fulfillment of the requirements for the degree of Doctor of Philosophy, The City University of New York

2008

UMI Number: 3296962

UMI Microform 3296962

ProQuest Information and Learning Company
300 North Zeeb Road
P.O. Box 1346
Ann Arbor, MI 48106-1346

This manuscript has been read and accepted for the Graduate Faculty in Engineering in satisfaction of the dissertation requirement for the degree of Doctor of Philosophy.

Date	Professor Feridun Delale
Date	Professor Mumtaz K. Kassir

Professor Benjamin Liaw

Professor Ali Sadegh

Associate Professor Jackie Li

Professor Allan Lau

THE CITY UNIVERSITY OF NEW YORK

Abstract

MECHANICS OF CARBON NANOTUBES (CNTS) AND THEIR COMPOSITES

by

Huapei Wan

Advisor: Professor Feridun Delale

In this thesis, the mechanical behavior of carbon nanotubes (CNTs) and the reinforced composites was studied using the continuum mechanics models. For single-walled nanotubes (SWNTs), a structural model based on molecular mechanics was developed. The model was then extended by considering the van der Waals forces to the study of multi-walled nanotubes (MWNTs). The current models were verified through many calculations and comparisons. As an application, the buckling behavior of carbon nanotubes (SWNTs and MWNTs) under axial compression and bending were studied. Another portion of the thesis was contributed to the continuum mechanics modeling of CNTs reinforced. The new contribution of the current work to the nanotube mechanics is a new strategy of correlating molecular potentials with strain energies of the structural members: beam and spring. In contrast to the existing model, the out-of-plane motion (inversion) of the covalent bond was distinguished from the in-plane motion in the current model. Consequently, the bending stiffness of the graphite layer can be correctly described. In addition, several key issues involved in the study of buckling behavior of CNTs under axial compression and bending loads were discussed. The role of geometrical perturbation on the onset of compressive buckling was well identified. For bending buckling, the buckling was found to be sensitive to the boundary conditions (BCs) applied at the ends of the nanotube. The continuum mechanics analysis of CNTs reinforced composites showed that a critical nanotube length was required in order to fully transfer the load between the high stiffness tube and the matrix. The effects of the tube length and the interphase on the effective properties of the reinforced composite were also discussed.

ACKNOWLEDGEMENTS

This dissertation would not have been possible without the help and support of a number of people. Perhaps the individual to whom I am most indebted is Professor Feridun Delale, who has been my advisor, mentor and a source of support throughout years of my graduate study. His patience and willingness as a teacher to develop my understanding and comprehension of the topics is greatly appreciated. It has been an honor to work with professor Delale, and I will always be grateful for his help. In addition, I would like to thank my PhD's committee members in the City College of New York (CCNY): Professor Ali Sadegh, Professor Benjamin Liaw, and associate professor Jackie Li for their various suggestions and insightful advice throughout the years. Also, it is my honor to have Professor Allan Lau from Drexel University to be one of my committee members.

There have been a number of people at CCNY whose assistance has been valued. I would also like to thank Dr. Lianxi Shen for his advice in the modeling work. He was always willing to share his expertise and discussion. Special thanks are reserved for Dr. Minwei Gong, for his help in providing high performance and parallel computation environment. I am also grateful for Dr. Shigeo Maruyama (Univ. of Tokyo) in providing software package of coordinate generator (WRAPPING) for the carbon nanotube.

During my time at the City College of New York, various members (Dr. Hale Ergun, Dr. Savvas Xanthos, Dr. Yanxiong Liu, Dr. Thomas Cheung, Mr. Ercan Sevkat, Mr. Morris Koffi,) in the ME Department are to be thanked for their supports and friendship.

I would also like to especially thank my parents and wife for their unconditional support as I pursued this goal.

TABLE OF CONTENTS

LIST OF FIGURES

LIST OF TABLES

CHAPTER 1 : INTRODUCTION

First discovered by Iijima in 1991, the carbon nanotubes (CNTs) have played a central role in leading the overall progress of nanoscale science and technology during the past decade. CNTs represent a new class of nanoscale material. Their many extraordinary mechanical and electronic properties are essentially due to their unique geometric and chemical structures, which have been intensively studied through both experimental and theoretical approaches. Their applications such as nanoscale transistor, electromechanical actuator, biomolecular and chemical sensor, and high resolution probe in device fabrication have been supplemented with their use as reinforcement in nanocomposites and field emission arrays in the material development arena. Our understanding of the mechanical properties of CNTs has greatly improved through more than a decade of investigations. The intrinsic mechanical properties of CNTs, such as their stiffness, strength and deformability, have been relatively well investigated and understood; other mechanics-related properties of CNTs, such as buckling instability, interface mechanics, etc., have also being examined and a comprehensive knowledge of them is beginning to emerge.

In this chapter, an overview of CNTs and CNTs reinforced composites is given, with a focus on the mechanical properties and the corresponding modeling approaches.

1.1 Molecular Structure of Carbon Nanotubes

A CNT can be geometrically described as a seamless cylinder rolled from a graphene sheet (Figure 1.1), called a single-walled carbon nanotube (SWNT). The tube may be

closed at its ends by endcaps of hemispheres of fullerenes (Figure 1.2). In general, the smooth interface shown is not possible because a hemispherical geometry is often precluded by other nanotubes structures, but they are naturally closed by endcaps of some sort. Depending on synthesis conditions, multi-walled carbon nanotubes (MWNTs) can also be obtained. A MWNT can be thought as multiple nested cylinders consisting of rolled graphene sheets (Figure 1.3). The tubes discovered by Iijima (1991) were MWNTs. Individual SWNTs are not chemically stable and often bundle together to form nanotube ropes or bundles (Figure 1.4). The tubes in the bundle or within a MWNT interact through the weak non-bonded van der Waals forces with an ideal spacing of 3.4 Å, the same distance as the layer separation found in graphite. They remain free to slide and rotate independently with only small resistive forces. Thus, it is expected that tension and torsion loads will not significantly transfer from outer tube walls to inner tube walls.

The primary structural unit of a nanotube is a hexagonal ring which consists of σ sigma and π bonds (Figure 1.5). Each atom is bonded to its nearest 3 neighbors, at approximately 120 degrees in plane angles. The primary bonds between these atoms are hybridized sp2 bonds, or σ bonds. These bonds are very strong and produce excellent in-plane properties of the nanotube. The π-bonds are delocalized bonds and are much weaker; however they are centered, symmetrically about 0.33 Å from the central axis of the sigma bond. Thus they are primarily responsible for the out of plane properties, such as the wall bending stiffness. Pentagonal and heptagonal ring structures are also possible. A combination of these structures, termed the 5-7-7-5 defect (Figure 1.6), is proposed to be a pathway for plastic deformations and termed the Stone-Wales transformation (A.J. Stone and D.J. Wales, 1986). Quantum Mechanics (QM) simulations have also shown evidence of structural holes in nanotubes, which subsequently lower the nanotube stiffness and strength (D. Troya, 2003).

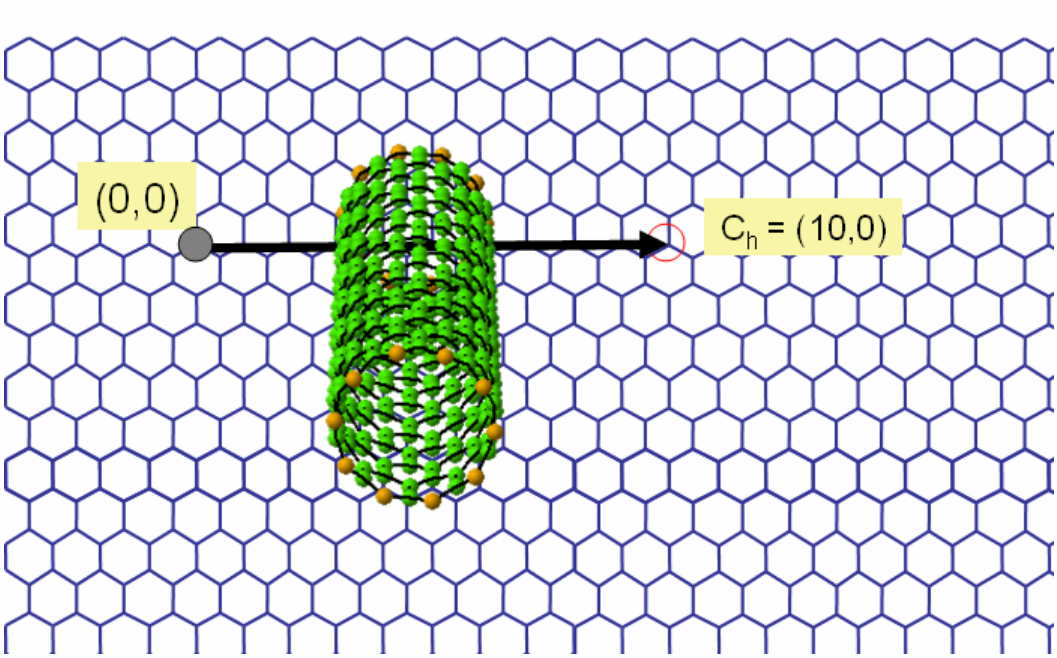

Figure 1.1: A single-walled carbon nanotube with zigzag chirality (10,0)

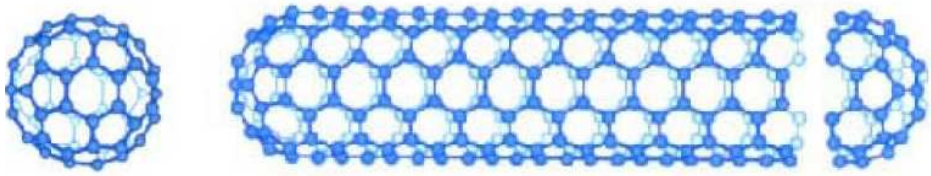

Figure 1.2: Atomic structures of a C60 fullerene (left) and a (5,5) nanotube (right)

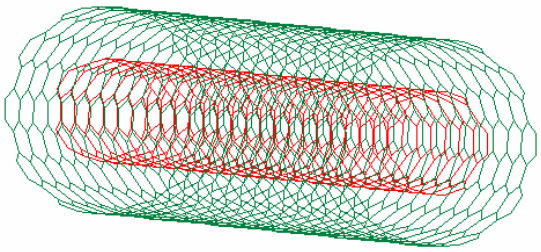

Figure 1.3: A double-walled nanotube (DWNT) with (5,5)@(10,10) chirality

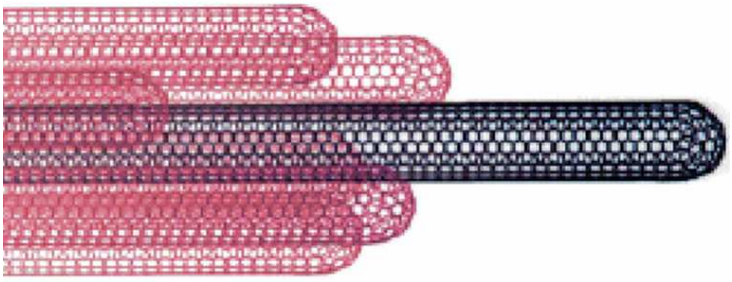

Figure 1.4: Nanotube bundles of SWNTs

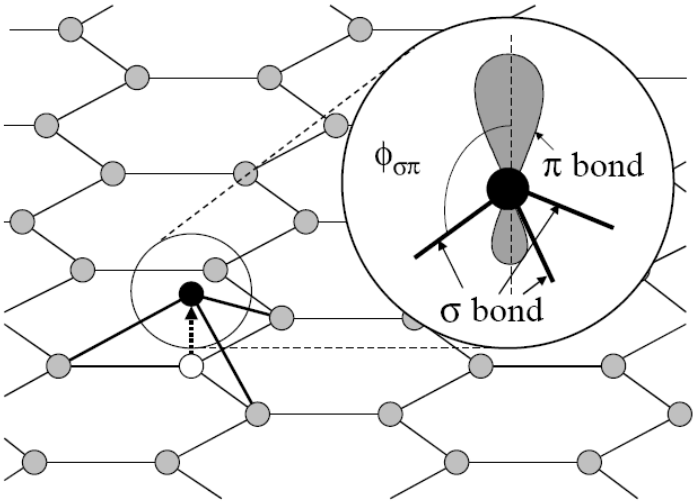

Figure 1.5: Schematics of the bonds and structure

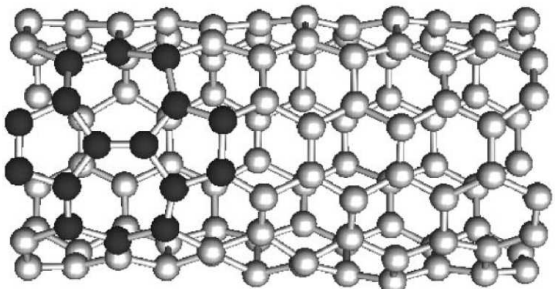

Figure 1.6: The Stone-Wales transformation (5-7-7-5)

The type of SWNTs can be uniquely identified by the rollup angle (termed helicity or chirality) and the diameter of the hexagon ring structure. The White notation (C. White, 1992) is commonly used to classify a nanotube structure. In this notation, the basal vector ($\mathbf{a}_1, \mathbf{a}_2$), is followed (Figure 1.7). The number of hexagon cells in the $\mathbf{a}_1$ and $\mathbf{a}_2$ directions when traveling once around the tube is recorded as (*m*, *n*) and is used to identify the type of SWNT. In this way, both the diameter and the helical angle θ can be also defined:

$$d_{CNT} = \sqrt{3}/\pi a_{C-C}\sqrt{m^2+mn+n^2} \quad , \tag{1.1}$$

and

$$\theta = \tan^{-1}\sqrt{3}n/(2m+n)\,, \tag{1.2}$$

where, a_{C-C} is the carbon-carbon lattice constant (about 0.142nm).

It is the combination of the chiral symmetry and the unique properties of graphene that ultimately determines many unprecedented mechanical and electrical properties of CNT. For example, armchair nanotubes are formed when *n* = *m* and the chiral angle is 30° (Figure 1.8). Zigzag nanotubes are formed when either *n* or *m* is zero and the chiral angle is 0°. All other nanotubes, with chiral angles intermediate between 0° and 30°, are known as chiral nanotubes. Armchair SWNT is electrically conductive while zigzag SWNT is an insulator. Mechanical properties of the tube such as Young's modulus show some dependence on the tube chirality especially when the tube diameter is small (less than 1 nm).

Nanotubes with different molecular structures, such as BN and BC3 or 'white carbon' nanotubes (generalized as $B_xC_yN_z$), have also been created (E.C. Hernandez, 1998). The fundamental feature required for nanotube creation is the hexagonal atomic ring structure. These tubes have been found to have lower mechanical properties, but also possess other desirable qualities for certain applications. For example, 'white carbon' nanotubes, which still have about 68~75% the modulus of CNTs (E.C. Hernandez, 1998), are electrically inactive and therefore desirable for nanocomposites material

applications which need an insulating material.

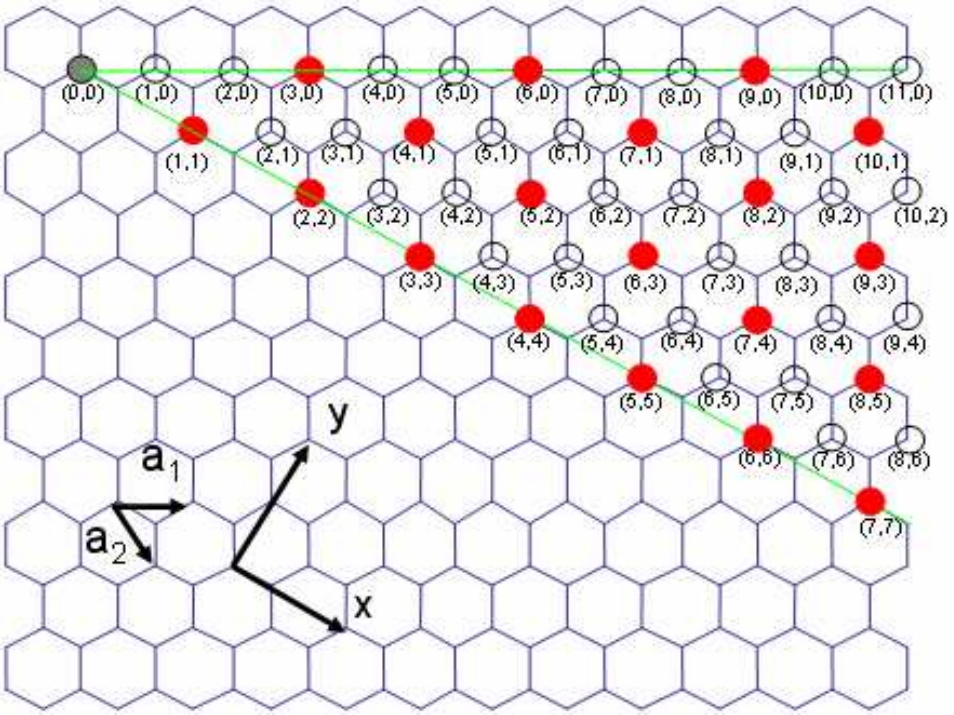

Figure 1.7: Lattice structure of a graphite sheet

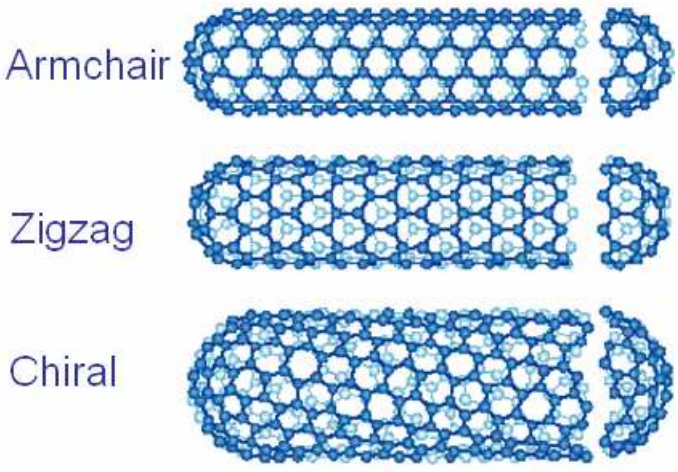

Figure 1.8: Single walled nanotubes with different chiral structures

1.2 Mechanical Properties of Carbon Nanotubes

Carbon nanotube has played a central role in leading the overall progress of nanoscale science and nanotechnology during the last decade. Many unprecedented mechanical and electrical properties of CNT have been discovered. For example, the axial Young's modulus of the CNT is found to be around 1000 GPa. CNT has been modeled and measured as having the highest tensile yield strength, as high as 170 GPa, among existing materials. CNT can either be metallic and semiconducting depending on its chiral symmetry and due to quantum confinement effect; SWNT has been demonstrated to be a ballistic conductor even at room temperature, where electrons propagate through the CNT effectively with the absence of any scattering over several hundreds nanometers; and the electronic and chemical properties of CNT can be effectively modulated by the local structural deformation of CNT. In the following, we will focus on the mechanical properties of CNTs.

Much of the initial work studying the mechanical properties of nanotubes consisted of computational methods including molecular dynamics calculations based on empirical potentials, the tight-binding-based approaches, and the first principles of quantum mechanics. These models are primarily used to study SWNTs because of the increase in computational resources necessary to model systems comprised of a larger number of atoms. There are also a few continuum mechanics models based on the principle of molecular mechanics. Typically these studies have found nominal values for the axial Young's modulus on the order of 1000 GPa (assuming a shell thickness of 0.34 nm), with values for the Poisson ratio approximately 0.16 to 0.30. Values of Young's modulus for SWNT bundles were between 0.4 and 0.8 TPa. The shear modulus of SWNTs is found to be about half of that of the Young's modulus (0.5 TPa). The strength of the nanotube is around 100 GPa. Most of these models assumed defect-free nanotubes. Nanotubes with significant number of defects (such as those produced via CVD methods) are expected to have much lower values.

More recently, a great deal of progress has been realized in manipulating and testing individual nanotubes and nanotube bundles. In general, the experimental results have validated the computational predictions. The reader is referred to a recent review paper of M. Yu (2004) about the experimental techniques.

1.3 Applications

With the rapid progress in the synthesis of large quantity and high quality CNTs, many researchers have also begun to focus on the manufacturing and engineering of CNTs for developing new composite materials and electronic products. For example, CNTs can be used as a filler phase (reinforcement) in a host material. A great deal of interest in CNTs reinforced composites for structural applications exists due to a number of potential benefits that are predicted with such materials. For instance, the high stiffness of CNTs makes them perhaps the ultimate high-stiffness reinforcing material. Tensile strength of the CNTs reinforced composites is increased by an order of magnitude (compared to traditional composites) due to the high elastic strain (as large as 5%) of CNTs filler. The high stiffness- and strength-weight ratios suggest the possibility of substantial weight savings for weight-critical applications. In addition to their outstanding mechanical properties, CNTs have also been shown to possess exceptional electrical and heat-related properties, suggesting materials that may be designed to meet mechanical as well as secondary material property specifications. Despite these potential benefits, a number of critical issues must be overcome before the full benefit of such materials can be realized. Such issues include: high cost of CNT synthesis, poor bonding between the nanotube and the host materials, dispersion and alignment of CNTs within the composites.

Other notable examples include large scale CNT field emission array for flat panel displays. Results have shown that the nanometer-size, large aspect ratio and the high electrical/thermal conductivity of CNTs allow a CNT field emission array to be

operated at very low threshold voltage and with very small power consumption. Nanotubes could also be used to replace current micro-electronic materials (MEMs) as the beam structure, reducing MEM sizes even further. The physical properties such as the conductance of CNTs can be significantly changed by the occurrence of buckling, which lead to potential applications of CNTs as the next-generation nanoelectronic devices (nanotransistors), nanofluid components (nanovalves), and reversible elements in nanoelectromechanical systems (NEMS) by switching between the buckled state and normal state of the CNTs. MWNTs have been proposed as cylindrical bearings due to the ability of their walls to slide freely. Molecular modeling research has also been performed which studied the feasibility of using the tubes as shafts for nano-gears. CNTs have also been proposed as nanoscale drug dispensers.

The rapid advance of CNT-related applications in many fronts can not obviously be captured by the few examples above. Many of these potential applications are to be demonstrated and supported by both experimental and theoretical investigations.

1.4 Modeling of Carbon Nanotubes

To study the mechanical behavior of CNTs, many theoretical modeling approaches have been developed. Depending on their feasibilities, these approaches can be categorized at various scales, loosely from the smallest to the largest scale, including molecular (atomistic) simulations, coarse grain simulations, continuum mechanics, composite micro-mechanics, and component level structural mechanics. With the development of more accurate force field and numerical algorithms, MD simulations have been shown to play an important role in revealing the mechanical behavior of CNTs. The major techniques include classical molecular dynamics (MD), tight-binding molecular dynamics (TBMD) and density functional theory (DFT). In principle, any problem associated with molecular or atomic motions can be simulated

by these modeling techniques. However, due to their huge computational tasks, practical applications of these atomistic modeling techniques are limited to systems containing a small number of molecules or atoms and are usually confined to studies of relatively short-lived phenomena, from picoseconds to nanoseconds.

A few continuum mechanics models were also proposed, in which a carbon nanotube is modeled as a thin cylindrical shell or beam (B.I. Yakobson, 1996; V.M. Harik, 2000; C. Ru, 2000). In treating the CNT as a continuous material, an effective thickness has to be defined in order to derive material properties such as Young's modulus, shear modulus, bending modulus. Yakobson found that the compressive buckling of a SWNT can be fairly described by the continuum theory of buckling of thin-shell cylinder (B.I. Yakobson, 1996). He then stated one of the early results on nanomechanics, "*the laws of continuum mechanics are amazingly robust and allow one to treat even intrinsically discrete objects only a few atoms in diameter.*" This allowed subsequent researchers to utilize continuum mechanics to classify CNT material properties with more confidence. For example, the compressive buckling behavior of SWNTs and MWNTs have been studied by column-buckling theory with or without the surrounding media by a group of researchers (C. Ru, 2000 a,b; C. Wang, 2004). The drawback of these approaches is that they can not characterize the discrete lattice structure of the CNTs and their accuracy has to be confirmed by atomistic simulations.

Another category of research located between continuum mechanics and molecular mechanics is a series of work based on the molecular mechanics of carbon nanotubes, where the interactions between carbon atoms can be expressed by continuum functions of the atomic displacements. This category of modeling can be further divided into two tracks: explicit (either analytical or numerical) solution and finite element simulation. In the framework of molecular mechanics, energy approaches have been adopted to derive the analytical solution of effective elastic constants of SWNTs (T. Chang and H. Gao, 2003; L. Shen and J. Li, 2004) and MWNTs (L. Shen and J. Li, 2005; T. Chang, 2006). These methods take into account of periodical piece

of the nanotube; however the length effect which is pertinent to the buckling problem can not be considered. Consequently, they are not feasible to study the length-dependent buckling behavior of the CNTs. Finite element method that incorporates the molecular structural model of CNTs has also been developed (G.M. Odegard, 2001; C. Li, 2002). The C-C bonds in the CNT are replaced by structural elements such as truss rods (G.M. Odegard, 2001) and beams (C. Li, 2002) in these molecular mechanics (MM) based approaches. The sectional properties of the truss or beam members are derived from molecular mechanics theory where the potentials of the covalent bond are represented as functions of the change of geometrical variables (such as length, bend angle, twist angle). The properties of CNTs can then be obtained through finite element analysis of the structural assembly constructed by beam elements or truss elements. However, the bending stiffness of the graphite layer in a CNT is either not addressed (in truss model) or incorrectly addressed (in beam model). Therefore, they are not suitable to simulate the problems where the local bending is very dominant such as local buckling of the CNT. This drawback is addressed in detail in Chapter 2.

In the present work, a modified structural model based on C. Li's work (C. Li and T. Chou, 2002) is developed. The major difference from the original structural model is the establishment of relationship between the beam sectional properties and the bending stiffness of the graphite layer. By changing the circular cross-section of the beam element in the original beam mode (C. Li and T. Chou, 2002) into the rectangular cross-section, we can distinguish the two different bending of the bond: in-plane and out-of-plane. As a consequence, a new set of sectional properties of the beam element can be obtained. Therefore, the current model can be used as a tool to simulate the mechanical behavior where the local bending of the graphite layer in the CNT has to be considered. When incorporated in the finite element analysis, the current model can be more efficient (than MD and MM) in performing numerical (virtual) experiments to study the effective mechanical properties (Young's modulus, shear modulus, etc) and the buckling behavior of CNTs.

1.5 Methodology

The basic procedure used to study the mechanical behavior of CNTs and their reinforced composites is summarized below.

(1) Develop a new molecular structural model based on molecular mechanics and the model of C. Li (2003).

(2) Perform virtual experiments such as tension, torsion, and bending to simulate the elastic properties (such as Young's modulus, shear modulus and bending stiffness) of SWNTs and MWNTs.

(3) Perform virtual experiments such as compression and bending to simulate the buckling behavior of SWNTs and MWNTs.

(4) Analyze the volume representative element of CNTs reinforced composite for effective mechanical properties of the composite.

The first step, the development of a modified beam model will be explained in detail in Chapter 2. The second and third steps will be addressed in chapters 3 and 4 respectively. In chapter 5, CNT reinforced composites are studied by continuum mechanics simulations.

CHAPTER 2 : A STRUCTURAL MODEL FOR CARBON NANOTUBES

2.1 Introduction

Continuum mechanics is found to be “amazingly robust” and “allow(s) one to treat even intrinsically discrete objects only a few atoms in diameter.” (B.I. Yakobson, 1996). Especially with the help of the principle of molecular mechanics, a few analytical continuum models (G.M. Odegard, 2002; T. Chang and H. Gao, 2003; L. Shen and J. Li, 2004; T. Chang, 2006) have been developed to predict the mechanical behavior of carbon nanotubes (CNTs). Consequently, the mechanical properties of CNTs can be obtained more efficiently and faster than molecular dynamics simulation, with fairly reasonable accuracy. Predictions of effective elastic properties of CNTs such as the Young’s modulus through both analytical and numerical solutions are found to be in good agreement with MD simulations and experimental measurements. Structural models of CNTs have also been developed (G.M. Odegard 2002; C. Li and T. Chou, 2003) where the covalent bonds between atoms can be modeled by structural members such as truss rods or beams. Such structural models favor the atomistic-level finite element analysis in solving complicated deformations. As a result, CNTs, either modeled as systems for the broad study of effective properties in low dimensionality or as a unique device having excellent mechanical properties, can be studied by numerical (virtual) experiments. In the current chapter, a new structural mechanics model will be developed to obtain a better approximation of the molecular potentials of CNTs. Thus, it is expected that the model can be used as a tool to predict the mechanical behavior of CNTs more accurately than the existing structural models.

In the following sections, first an introduction of the principle of molecular mechanics is given. Then the existing structural models (beam-model) of the single-walled carbon nanotube and the current modification are introduced. Then, the modified structural model is extended to multi-walled carbon nanotubes where the van del Waals interactions between the subtubes are also modeled as a continuum structural member: non-linear springs.

2.2 Structural Model of SWNTs Based on Molecular Mechanics – *Beam Model*

Atomic interactions become dominant during the investigation of mechanical properties at near molecular scales. Quantum and molecular mechanics aim to correlate the atomic positions to the system's energy. From the viewpoint of molecular mechanics, the atomic nuclei in a carbon nanotube can be regarded as material points whose motions are regulated by force fields generated by electron-nucleus interactions and nucleus-nucleus interactions. The force fields can be expressed in forms of steric potential energies which solely depend on the relative positions of the nuclei constituting the molecule. Due to cumbersome calculations, it is preferred to neglect the electronic structure by applying the Born-Oppenheimer approximation. Consequently, the energy is defined only as a function of the nuclear positions irrespective of the electronic structure. In general, the total potential energy of the system can be expressed as sum of individual energy terms as,

$$E = E_\rho + E_\theta + E_\omega + E_\tau + E_{VDW} + E_{EL} \tag{2.1}$$

where E_ρ, E_θ, E_ω, and E_τ are energies associated with bond-stretching, angle-variation, inversion and torsion, respectively (Figure 2.1). E_{VDW} and E_{EL}, are associated with van der Waals and electrostatic interactions (both are also termed as non-bond interactions). A wealth of literature is available to determine the reasonable

functional forms of these potential energy terms (Rappe et al., 1992; Brenner, 1990; Cornell et al.1995). Therefore, various functional forms may be used for these energy terms, depending on the particular material and the load conditions under consideration.

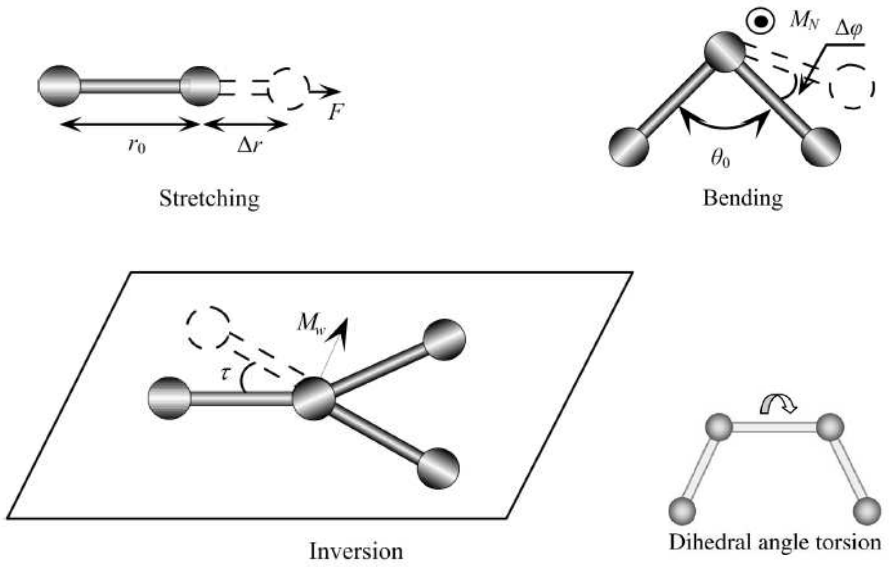

Figure 2.1: Inter-atomic interactions in molecular mechanics

In general, for covalent systems, the main contributions to the total steric energy come from the first four terms while the non-bond interaction potentials can be neglected,

$$E = E_\rho + E_\theta + E_\omega + E_\tau . \tag{2.2}$$

Under the assumption of small deformation, the first two terms E_ρ, E_θ can be expressed by harmonic functions,

$$E_\rho = \frac{1}{2}\sum_{bonds} k_r (\Delta r_i)^2 \tag{2.3}$$

$$E_\theta = \frac{1}{2}\sum_{angles} k_\theta (\Delta\theta_i)^2 \tag{2.4}$$

where Δr_i is the elongation of bond *i* and k_r is referred to as the force constant associated with bond stretching. $\Delta\theta_i$ and k_θ are the variance of angle and the associated force constants between two bonds.

The potential associated with bond inversion can also be described by harmonic function,

$$E_\omega = \sum_{bonds} \frac{k_\omega}{2}(\Delta\omega_i)^2 , \tag{2.5}$$

where $\Delta\omega_i$ is the inversion angle and k_ω is referred to as the force constant associated with bond inversion.

The torsional energy in molecular mechanics is primarily used to correct the remaining energy terms rather than to represent a physical process. Therefore, the torsional potential is not necessary in all molecular mechanics force field unless the total system energy needs to be adjusted to achieve the desired energy profile (e.g., to agree with experiment or rigorous quantum mechanical calculations).Torsional potential is usually modeled by a periodic function such as a cosine series expansion:

$$E_\tau = \sum_{bonds} \frac{V_n}{2}\left[1+\cos\left(n\phi-\gamma\right)\right], \tag{2.6a}$$

where V_n is a parameter which controls the amplitude of the curve, *n* the parameter of periodicity, and γ an angle which shifts the entire curve along the rotation angle axis (ϕ). The parameters are determined through curve fitting. For carbon nanotube and graphene, *n*=2 and $\gamma = 180^o$. Assuming small angle changes, (2.6a) can also be written as a harmonic function of the twist angle $\Delta\phi$,

$$E_\tau = \sum_{bonds} \frac{k_\tau}{2} (\Delta\phi)^2 , \qquad (2.6b)$$

where k_τ is the torsional force constant.

In the existing beam-model of CNTs (C. Li and T. Chou 2003), for convenience and simplicity, the potentials associated with the dihedral angle torsion and the improper torsion (inversion) are merged into a single equivalent term,

$$E_{torsion} = E_\omega + E_\tau = \frac{1}{2} \sum_{angles} k_\tau^* (\Delta\phi_i)^2 , \qquad (2.7)$$

where $\Delta\phi_i$ is the angle change of bond twisting and k_τ^* is the force constant of bond torsion. Note that, this assumption actually neglects the potential of bond inversion.

Motivated by the format of these energy functions, it is assumed that structural members (truss rod and beam) can be used to mimic the covalent bonds when the CNT is subjected to mechanical loads. Therefore, the discrete molecular structure of a SWNT can be modeled by a frame-like structure. The covalent bonds between two nearest-neighboring carbon atoms act like load-bearing beam members whereas an individual carbon atom acts as the joint of the beam (Figure 2.2). To establish a linkage between the structural model and molecular mechanics formulation, the energy equivalency relationship between strain energy of the structural model and the molecular potential of the lattice structure is used. As a result, the sectional properties of the beam member can be derived. The details (given by C.Li and T. Chou, 2003) are summarized as follows.

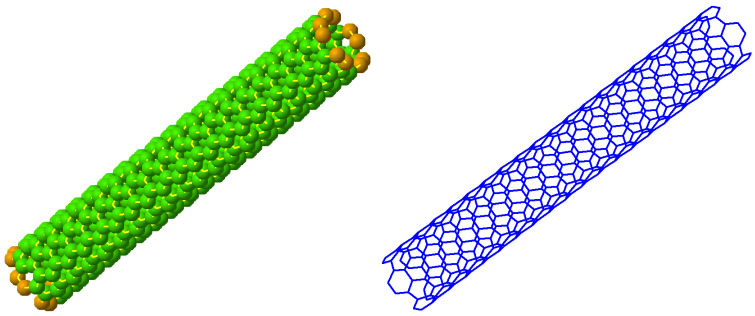

Figure 2.2: Structural model of a SWNT

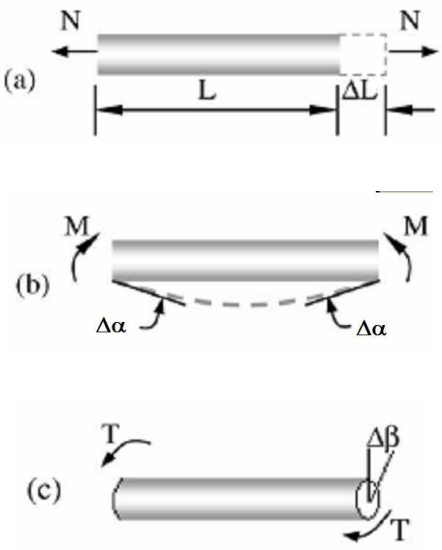

Figure 2.3: Tension, bending and torsion of a beam element

According to the theory of classical structural mechanics, the strain energy of a uniform beam of length L subjected to pure axial force N (Figure 2. 3a) is

$$U_1 = \frac{1}{2}\frac{EA}{L}(\Delta L)^2 \ , \tag{2.8}$$

where ΔL is the axial deformation under stretching. The strain energy of a uniform beam under pure bending moment M (Figure 2. 3b) is

$$U_2 = \frac{1}{2}\frac{EI}{L}(2\Delta\alpha)^2, \tag{2.9}$$

where $\Delta\alpha$ denotes the rotational angle at the ends of the beam. The strain energy of a uniform beam under pure torsion T (Figure 2.3 c) is

$$U_3 = \frac{1}{2}\frac{GJ}{L}(\Delta\beta)^2, \tag{2.10}$$

where $\Delta\beta$ is the relative rotation between the ends of the beam.

From Eqs. (2.2), (2.3), (2.7) and (2.8)-(2.10), a direct relationship between the structural mechanics parameters EA, EI and GJ and the molecular mechanics parameters kr, k_θ, k_τ can be deduced as follows:

$$\frac{EA}{L} = k_r \qquad \frac{EI}{L} = k_\theta \qquad \frac{GJ}{L} = k_\tau^* \tag{2.11 a, b, c}$$

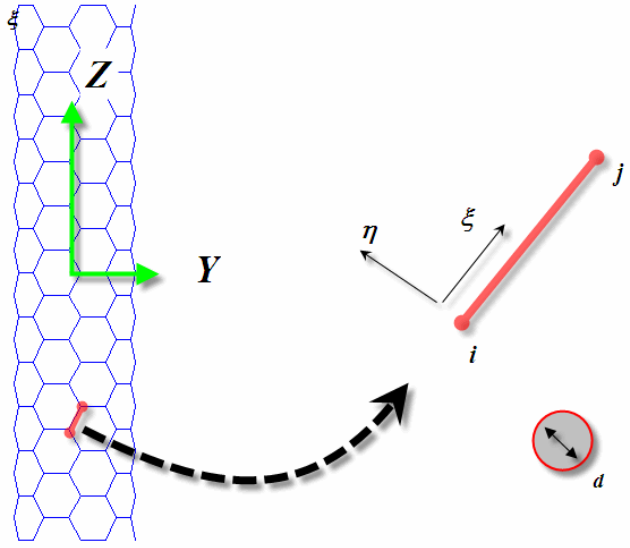

Figure 2.4: The beam members in the structural model of the SWNT (C. Li, 2003)

It is noted that for the carbon-carbon covalent bond, the equilibrium bond length $L = a_{C-C} = 0.142$ nm. Therefore, as long as the force constants k_r, k_θ, k_τ are known,

the stiffness constants EA, EI, GJ can be readily determined. For convenience, a solid circular section of certain diameter (d) is assumed for each beam member (Figure 2.4). As a result, the sectional properties E, G, I, J, d, A can be obtained by solving a set of close-formed equations as follows. First we express *A, I, J* in terms of *d*:

$$A = \pi d^2/4, \quad I = I_{\eta\eta} = I_{\zeta\zeta} = \pi d^4/64, \quad J = \pi d^4/64. \tag{2.12}$$

Combined with equations (2.11a,b, and c), the following is obtained:

$$d = \sqrt{\frac{16k_\theta}{k_r}}, \quad A = \pi\frac{k_\theta}{k_r}, \quad I = \frac{\pi}{4}\left(\frac{k_\theta}{k_r}\right)^2, \quad E = \frac{k_r^{\,2}a_{C-C}}{4\pi k_\theta}, \tag{2.13a,b,c,d}$$

$$G = \frac{k_\tau^{\,*}k_r^{\,2}a_{C-C}}{8\pi k_\theta^{\,2}} \tag{2.13e}$$

From atomistic computations,

$$\frac{k_r}{2} = 469 \text{ kcal mol}^{-1} \text{ Å}^{-2} = 3.26\times10^{-7}\frac{\text{nJ}}{\text{bond nm}^2} \tag{2.14}$$

$$\frac{k_\theta}{2} = 63 \text{ kcal mol}^{-1} \text{ rad}^{-2} = 4.38\times10^{-10}\frac{\text{nJ}}{\text{angle rad}^2} \tag{2.15}$$

Thus from (2.13 a, b, c and d),

$$E = 5.488\times10^3 \text{ GPa}, \quad d = 0.146 \text{ nm}, \quad A = 0.017 \text{ nm}^2, \quad I = 2.268\times10^{-5} \text{ nm}^4. \tag{2.16}$$

It can be seen from (2.13), only the shear modulus *G* depends on $k_\tau^{\,*}$. In the reference, it is assumed that

$$\frac{k_\tau}{2} = 20 \text{ kcal mol}^{-1} \text{ rad}^{-2} \tag{2.17}$$

This results in a shear modulus,

$$G = 0.871 \times 10^3 \ \text{GPa} \quad . \tag{2.18}$$

And the Poisson's ratio can be calculated from $G = E/2(1+\nu)$ as,

$$\nu = 2.15 . \tag{2.19}$$

This Poisson's ratio is unusual for a traditional material. However, C. Li and T. Chow (2003) pointed out that the influence of k_τ on carbon nanotube Young's modulus shown to be very weak. Accordingly, it was stated that the value of Poisson's ratio of the beam element is not important. In our derivation, as will be shown later, a realistic value of Poisson's ratio will be used.

The accuracy and feasibility of the model has been verified (C. Li and T. Chou, 2003) by predictions of the effective mechanical constants (Young's modulus, shear modulus) of graphite and CNTs. However, by neglecting the inversion term E_ω in the total molecular energy, the above mentioned *beam-model* can not reproduce the mechanical response of graphite and CNTs under bending. In what follows we derive a *modified beam model* in which the inversion potential in the molecular system can be considered in a simple way.

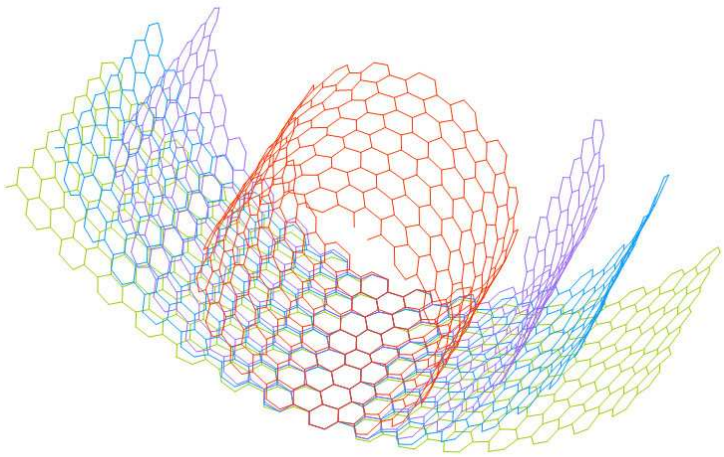

Figure 2.5: Rolling of a graphite sheet into a tube

2.3 A Modified Structural Model of SWNTs – *Modified Beam Model*

In this section, the bending stiffness of a graphite sheet (and the wall of a SWNT) and its impact in the continuum modeling of SWNTs is introduced first. Then an explicit solution of the bending stiffness is given which leads to a modified structural model (*modified beam model*) of SWNTs based on the above mentioned beam-model.

Since the potential associated with bond inversion is neglected in the above approach(C. Li and T. Chou, 2003), the bending resistance for the graphite layer of a CNT can not be appropriately addressed. In fact, as mentioned later in the present paper, the bending stiffness calculated from the sectional properties of the beam element given in (C. Li and T. Chou, 2003) is almost two times of the actual value. Also according to atomistic simulations (D. Robertson, 1992; Miyamoto, 1994 a, b; Kurti, 1998; Hernadez, 1998; Sanchez-Portal, 1999) of rolling a graphite layer (Figure 2.5) and other analysis (C. Ru, 2000; L. Shen and J. Li, 2004) , it seems that the CNT wall is very "soft" in resisting bending deformation. To describe the bending stiffness of CNTs by the continuum expression ($D_e = E_{CNT} t^3 / 12(1-\nu^2)$, where E, t, ν are the Young's modulus, thickness and Poisson's ratio of the CNT wall), one has to use a special set of (E_{CNT}, t) with typically values of (4.7~5.5TPa, 0.066~0.089nm), suggested in literatures (B. Yakobson, 1996; A. Pantano, 2004; X. Zhou, 2000). Note that a different set of (E_{CNT}, t) is used in describing the axial stiffness of the tube, typically (1TPa, 0.34nm).

In the present work, the beam model developed by Li&Chou is modified such that the circular cross-section of the beam element is replaced by rectangular section (Figure 2.6). The potential associated with bond inversion is taken into account through an in-direct way since the bond inversion in a CNT can not be directly described for a single beam element. The strain energy of rolling a graphite sheet into a nanotube is derived and compared to the results of atomistic simulations. Consequently, a

close-formed solution of the sectional properties of the beam element can be obtained.

$$A = bh,\ \ I_{\zeta\zeta} = \frac{1}{12}b^3 h,\ \ I_{\eta\eta} = \frac{1}{12}bh^3,\ \ J = I_{\eta\eta} + I_{\zeta\zeta} \tag{2.20}$$

The correlations of energies associated with bond stretching, bending and torsion are then rewritten as,

$$\frac{EA}{a_{C-C}} = k_r \qquad \frac{EI_{\zeta\zeta}}{a_{C-C}} = k_\theta,\ \ \frac{G(I_{\zeta\zeta} + I_{\eta\eta})}{a_{C-C}} = k_\tau. \tag{2.21 a, b, c}$$

Because the shear modulus *G* is not important (as also pointed out in (C. Li and T. Chou, 2003), and that the value of torsional force constant k_τ is not well determined from MD simulations, the third equation in Eqn. (2.21) is not considered in the present model. Instead, we assume the Poisson's ration (ν) of the beam element to be 0.3 and the shear modulus can then be obtained as

$$G = E/2(1+\nu). \tag{2.22}$$

The out-of-plane moment of inertia ($I_{\eta\eta}$) is derived from the equivalent strain energy (obtained from the structural model) of rolling a graphite layer and the rolling energy computed from atomistic simulations. For convenience, symmetric cases are considered which resulting an analytical solution for $I_{\eta\eta}$. By rolling a graphite sheet along symmetric direction, armchair or zigzag carbon nanotube can be obtained. In the following, these two cases are analyzed respectively, although a same solution of $I_{\eta\eta}$ can be found.

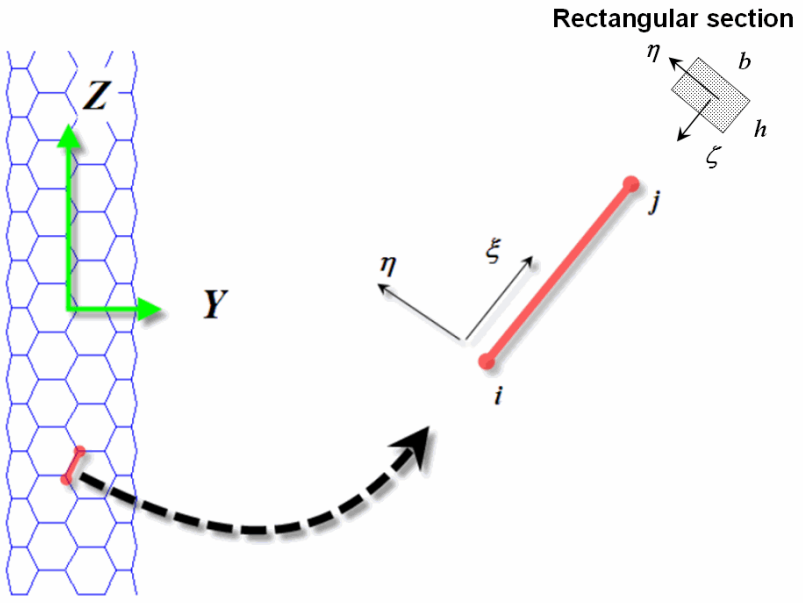

Figure 2.6: Modified beam element with rectangular section

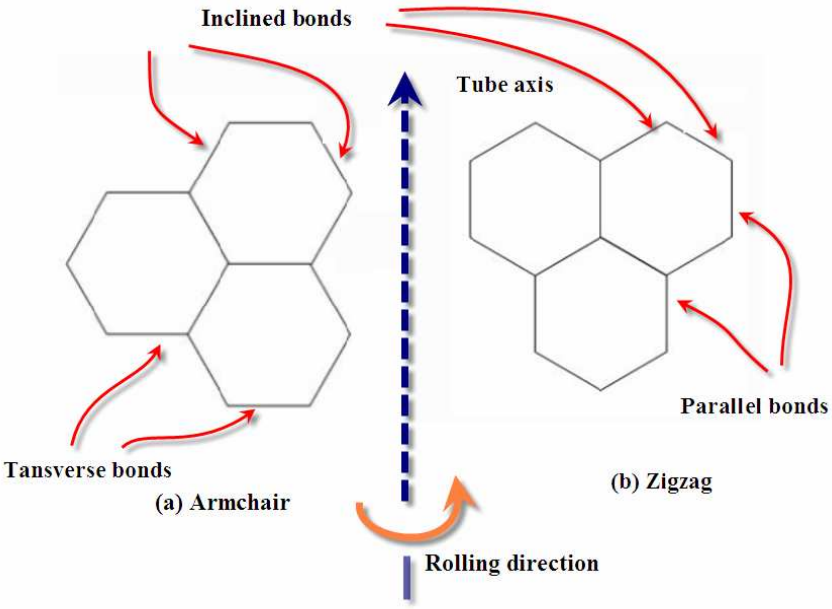

Figure 2.7: Roll a graphite layer into armchair or zigzag nanotube

Armchair nanotube (n, n)

When rolling the graphite into an armchair nanotube, it is assumed that only the "inclined bonds" and the "transverse bonds" (perpendicular to the tube axis) (Figure 2.7 a) contribute to the bending resistance. Whereas the other bonds are not bent since they are parallel to the axis of rolling. Therefore, the total strain energy is the sum of strain energies of bending of inclined bonds. If the number of inclined bonds in an armchair nanotube (n, n) is denoted as γ, then the number of transverse bonds (perpendicular to the tube axis) is $\lambda = \gamma / 2$. The total number of carbon atoms in the tube is,

$$N = \gamma + 2n . \tag{2.23}$$

From structural mechanics, the strain energy of a single transverse bond subject to bending moment M is

$$u_{o1} = \int_0^{a_{C-C}} \frac{M^2}{2EI} dl = \frac{2EI_{\eta\eta} a_{C-C}}{{d_{CNT}}^2}, \tag{2.24}$$

where a_{C-C} is the bond length (=0.142 nm) and E is the Young's modulus of the beam element.

The strain energy due to pure bending for a single inclined bond is

$$u_{o2} = \int_0^{a_{C-C}} \frac{(M/2)^2}{2EI} dl = \frac{EI_{\eta\eta} a_{C-C}}{2{d_{CNT}}^2} . \tag{2.25}$$

The total energy per atom is,

$$U^*_{bend} = \left(\frac{\gamma}{2} \frac{2EI_{\eta\eta} a_{C-C}}{{d_{CNT}}^2} + \gamma \frac{EI_{\eta\eta} a_{C-C}}{2{d_{CNT}}^2} \right) / N = \frac{3\gamma EI_{\eta\eta} a_{C-C}}{2{d_{CNT}}^2 (\gamma + 2n)} . \tag{2.26}$$

For a very long tube $\gamma >> n$, and the strain per atom due to the rolling of a graphite layer is given as,

$$U_{bend}^{*} = \frac{3EI_{\eta\eta}a_{C-C}}{2d_{CNT}^{2}} \quad . \tag{2.27}$$

It is noted that the above derived bending energy is proportional to $(1/d_{CNT}^{2})$ which agrees with the conclusion of MD simulations. The values of energy per atom are available (although they are slight differences from different simulations) for a wide range of nanotubes with different diameters, according to MD simulations. If we denote the value as $\overline{U}_{bend}/d_{CNT}^{2}$, then

$$U_{bend}^{*} = \frac{3EI_{\eta\eta}a_{C-C}}{2d_{CNT}^{2}} = \frac{\overline{U}_{bend}}{d_{CNT}^{2}}. \tag{2.28}$$

Therefore,

$$EI_{\eta\eta} = \frac{2\overline{U}_{bend}}{3a_{C-C}}. \tag{2.29}$$

Recalling that in the beam model,

$$EA/a_{C-C} = k_r \quad . \quad \text{(where } k_r = 2\times 3.26\times 10^{2}\ \frac{\text{nN nm}}{\text{nm}^{2}}\text{)}. \tag{2.30}$$

And, $I_{\eta\eta} = bh^{3}/12$, $A = bh$,

$$h = \sqrt{\frac{8\overline{U}_{bend}}{a_{C-C}^{2}k_r}}. \tag{2.31}$$

Using the results of Robertson (1992) for a (4, 4) SWNT, $\overline{U}_{bend}/d_{CNT}^{2}$=0.26 eV (or 0.0417 nN nm) where d_{CNT} = 0.542 nm, we obtain $h = 0.086$ nm.

Zigzag nanotube (n, 0)

Following a similar process for zigzag nanotubes, the same expression as above is

obtained for *h*. Assuming the number of inclined bonds is γ, then the total number of atoms in the zigzag tube is,

$$N = \gamma - \frac{3}{4}n \quad . \tag{2.32}$$

The bending strain energy of a single inclined bond can be expressed as a function of the tube diameter d_{CNT},

$$u_o = \frac{3EI_{\eta\eta}a_{C-C}}{2{d_{CNT}}^2}. \tag{2.33}$$

The total strain energy per atom is given as

$$U_{bend}^{\ *} = \gamma \frac{3EI_{\eta\eta}a_{C-C}}{2{d_{CNT}}^2} / N = \frac{3EI_{\eta\eta}\gamma a_{C-C}}{2(\gamma - \frac{3}{4}n){d_{CNT}}^2}. \tag{2.34}$$

For a very long tube, $\gamma >> n$, and the bending energy per atom is given as,

$$U_{bend}^{\ *} = \frac{3EI_{\eta\eta}a_{C-C}}{2{d_{CNT}}^2} \quad . \tag{2.35}$$

This is exactly the same expression obtained for an armchair nanotube. Thus,

$$h = \sqrt{\frac{8\overline{U}_{bend}}{{a_{C-C}}^2 k_r}}$$

<u>Sectional properties of the beam element in the modified beam model</u>

From the above derivation, the sectional properties of the beam element in the present work are obtained as follows:

Table 2.1: The sectional properties of the modified beam mdoel

$b = 0.127$ nm	$h = 0.086$ nm	$A = 0.011$ nm^2
$I_{\eta\eta} = 6.732\times10^{-6}$ nm^4	$I_{\zeta\zeta} = 1.468\times10^{-5}$ nm^4	
$E = 8476.836$ GPa	$G = 3260.322$ GPa	$\nu = 0.3$

Finite element verification

The rolling energy per atom is computed by numerical experiment through finite element analysis in which the modified beam model with the sectional properties listed in Table 2.1 is used. Different types of nanotubes have been studied and compared to the atomistic simulations in the literature (Table 2.2). It is shown that the FEA results agree very well with the atomistic computations. It is also noted that in the finite element analysis, the structure experiences large rotation. This means that the modified beam model is suitable for studying the large rotation problem of nanotubes.

It must be noted that using the sectional properties given by Li & Chou (2003) in (2.16), the calculated rolling energy per atom is about two times of those from the current results. Therefore, their model can not be used for predicting the mechanical behavior of CNTs when bending deformation of the graphite layer is induced (such as local buckling of the nanotube).

Table 2.2: Comparison of the rolling energy per atom obtained from MD simulation and the current FE calculations

Tube	d_{CNT} (nm)	**Rolling energy per atom** (eV)					
		Miyamoto 1994	Robertson 1992	Kürti 1998	Sánchez-Portal 1999	Hernandez 1998	**FEA results (present)**
(3,3)	0.407	-	0.442	-	-	-	**0.441**
(6, 0)	0.47	0.33	-	-	-	-	**0.342**
(4, 4)	0.543	0.265	0.26	-	0.26	0.275	**0.261**

(7, 0)	0.548	0.26	-	-	-	0.27	**0.258**
(8, 0)	0.626	0.19	-	-	-	-	**0.187**
(5,5)	0.678	-	0.17	-	0.162	-	**0.17**
(9, 0)	0.705	0.14	-	0.159		-	**0.157**
(10,0)	0.783	-	-	0.128	0.138	-	**0.126**
(6,6)	0.814	-	0.12	-	0.113	-	**0.117**
(8, 4)	0.829	-		-	0.12	-	**0.113**
(7,7)	0.949	-	0.08	-	-	-	**0.086**
(8, 8)	1.085	-	-	0.069	0.0613	0.075	**0.066**
(15,0)	1.174	-	-	0.057	-	-	**0.056**

Bending stiffness of the graphite layer

The effective bending stiffness of SWNT shell can also be expressed as function of the sectional properties of the beam element. For a cylindrical thin shell rolled up from a plate, the strain energy is, $U = 2\pi D_e L / d$, where, L, d are the length and diameter of the cylindrical shell. D_e is the effective bending stiffness of the shell. If a graphite sheet is assumed to be a continuum plate and the CNT is assumed to be a cylindrical thin shell, then the strain energy per atom can be expressed as $U_0 = 2\pi D_e L_{CNT} / (N d_{CNT})$. Take the (n, n) armchair tube for example, the atom number for a L_{CNT} long tube is $4nL_{CNT} / (\sqrt{3} a_{C-C})$. Note that $d_{CNT} = 3a_{C-C} n / \pi$, then Eqn. (21) can be rewritten as, $U_0 = 3\sqrt{3} D_e a_{C-C}^2 / (2 d_{CNT}{}^2)$.

Compare with the MD simulation from (Robertson, 1992), we obtained $D_e = 1.46$ eV. This is in agreement with the result in (L. Shen and J. Li, 2004) where $D_e = 1.395\,\text{eV}$.

Also the bending stiffness of the graphite layer can be expressed as function of the sectional properties of the beam element as $D_e = EI_{\eta\eta} / \sqrt{3} a_{C-C}$. It is noted that the same conclusion can be drawn for zigzag nanotubes. And the bending stiffness

calculated from the original beam model is about 3.18 eV, which overestimated the actual value.

2.4 Extended Model for Multi-Walled Carbon Nanotube (MWNT)

2.4.1 Construction Method

The structural model outlined above for SWNTs can be extended to simulate the mechanical behavior of multi-walled carbon nanotubes (MWNTs). It is well known that the interlayer interactions are weak non-bond molecular forces (so called van der Waals forces). Attraction occurs when a pair of atoms approaches each other within a certain distance, whereas they repulse each other as the atomic distance becomes short. The van der Waals interaction is modeled by the general Lennard–Jones '6–12'' potential (Lennard–Jones, 1924), which provides a smooth transition between the attraction and repulsion regions. The general LJ 6-12 potential is commonly expressed as

$$U(r) = 4\varepsilon\left[\left(\frac{\sigma}{r}\right)^{12} - \left(\frac{\sigma}{r}\right)^{6}\right], \tag{2.36}$$

where r is the distance between interacting atoms, ε and σ are the Lennard-Jones parameters ($\sigma = 0.34\text{nm}$ and $\varepsilon = 0.0556\,\text{kcal/mol}$). The potential $U(r)$ is usually truncated at an inter-atomic distance of 2.5σ without a significant loss of accuracy (see Figure 2.8) .

Based on the Lennard–Jones potential, the van der Waals force between interacting atoms can be derived by differentiating (2.36) with respect to r:

$$F(r) = \frac{dU(r)}{dr} = -24\frac{\varepsilon}{\sigma}\left[2\left(\frac{\sigma}{r}\right)^{13} - \left(\frac{\sigma}{r}\right)^{7}\right]. \tag{2.37}$$

The variations of the van der Waals force with the distance between two interacting

atoms are illustrated in Figure 2.9. From (2.37), when the force is zero, we can obtain the equilibrium distance between two atoms: $r = \sigma/(0.5)^{1/6} = 0.382$ nm .

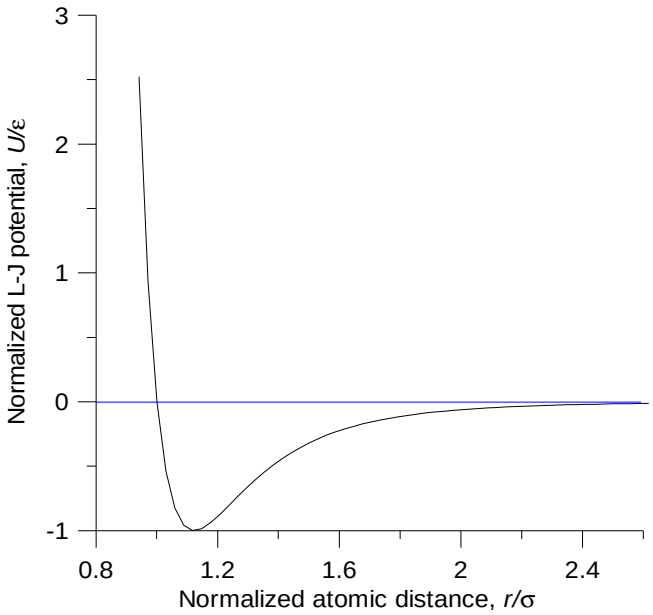

Figure 2.8: L-J 6-12 potential.

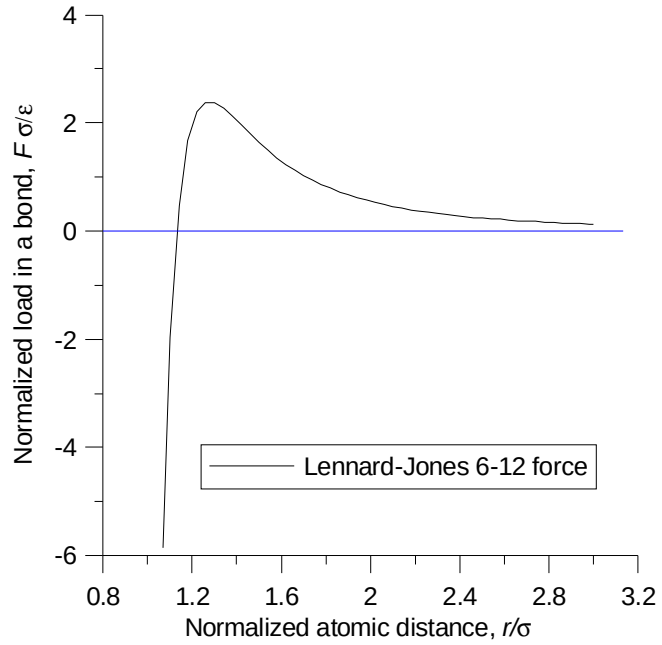

Figure 2.9: L-J 6-12 force.

To simulate the van der Waals interaction between the graphite layers, artificial

structural members between pairs of atoms of the nearest-neighboring graphite layer in a MWNT are created. Since the van der Waals forces (2.37) are non-linear, one can use the non-linear spring element (SPRINGA) in ABAQUS 6.5. The element needs the input of the force-deformation ($f - \delta L$) curve which is limited to 20 points (Figure 2.11). The curve can be calculated using (2.37) for different initial atomic distance.

Since 20 points may be too few to describe the highly non-linear van der Waals force, another choice is to use the User-Defined Subroutine (UMAT) in ABAQUS to describe the constitutive relationship explicitly. For this purpose, a subroutine (UMAT-VDW) is developed to simulate the van der Waals force by truss elements. With the help of the subroutine, the influence distance of the van der Waals forces can be set very long so that the sliding between two graphite layers can be simulated.

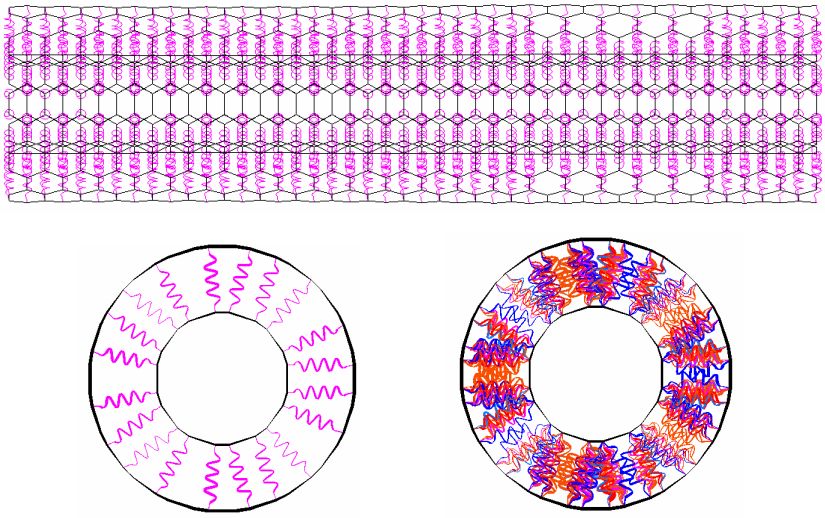

Figure 2.10: Illustration of non-linear spring elements between graphite layers in a DWNT.

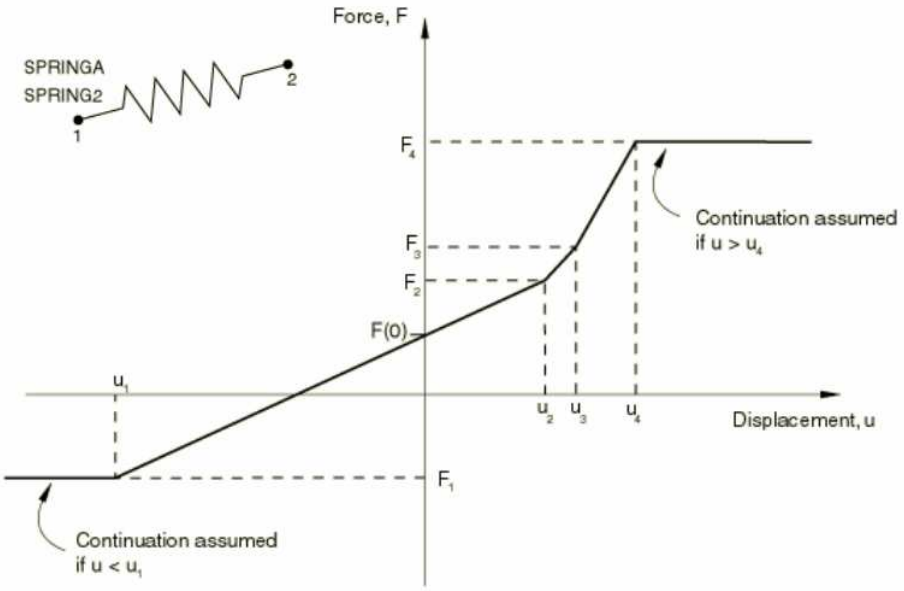

Figure 2.11: Nonlinear SPRING element and the force–relative displacement relationship in ABAQUS.

It is noted that even though the behavior of the spring element is high non-linear, no particular effort is needed in control the convergence of solution. For tension problem of the nanotube, since the interlayer deflection is very small, the van der Waals force is relatively small compared to the rigidity of the tube wall. For buckling problem of the nanotube, since small load step and damping solution control parameters have to be adopted, no extra consideration of convergence is needed for the nonlinear behaviors of the spring elements.

As a result, the structural model developed previously is extended to simulate the mechanical behavior of MWNTs. In the modified model, each nested SWNT is replaced with an assembly of beam elements, whereas the interlayer interactions are modeled by numerous non-linear spring elements or truss element with user-defined material properties (UMAT-VDW). Although the van der Waals forces exist also between tubes other than the nearest neighboring tubes, it may be assumed that such interactions are much weaker. Therefore, in the current study, only the interaction

between the nearest-neighboring layers is considered.

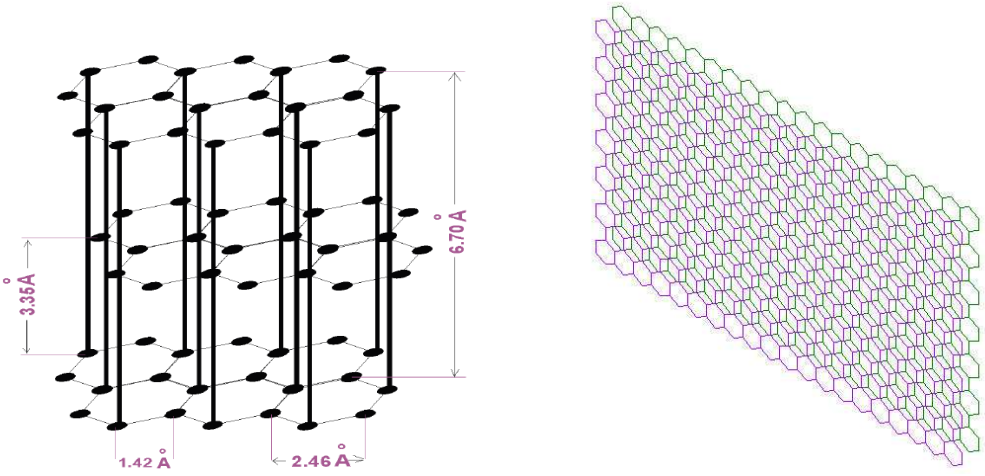

Figure 2.12: (a) Ab stacking of graphite layers; (b) Two graphite layers

2.4.2 Verification of the modified model

The feasibility of the extended structural model to study multi-layer graphite structures is verified by the following examples: (a) Interlayer pressure between two graphite layers; (b) Load transfer between two layers in a DWNT; (c) Interlayer shear strength in a DWNT.

(a) Interlayer pressure between two graphite layers

In order to validate the model, the pressure between two graphite layers is studied. As shown in Figure 2.12 b, two graphite layers in AB registry with an initial spacing of 0.34nm are constructed by beam elements. Graphite as a layered material consists of chemically inert layers which are held together by the weak van der Waals forces. Layers are built up by a honeycomb arrangement of the carbon atoms which are strongly covalently bonded to each other. Neighboring layers are shifted relative to each other by an AB AB AB stacking sequence (Figure 2.12 a). This stacking sequence gives rise to two non-equivalent carbon atom sites within the 2D surface

unit cell: One carbon atom (A-site) has a neighboring carbon atom directly below in the next layer whereas the other carbon atom (B-site) is located above the center (hollow site) of the sixfold carbon ring in the second layer.

As shown in Figure 2.12 b, the in-plane geometry is held fixed, and the inter-layer distance is changed. The computed pressure, as a function of the distance change, is studied. The results are compared with published experimental data by Zhao and Spain (1989) who gave the pressure / interlayer-distance relation as,

$$p(r) = \frac{36.5}{6}\left[\left(\frac{0.34}{r}\right)^{10} - \left(\frac{0.34}{r}\right)^{4}\right] \text{ GPa}, \tag{2.38}$$

where r is the distance given in the unit of nm. The results are plotted in Figure 2.13. It can be seen that the current results agree very well with the experimental data especially in the repulsive region. Note that the experimental measurement was carried out under compression load.

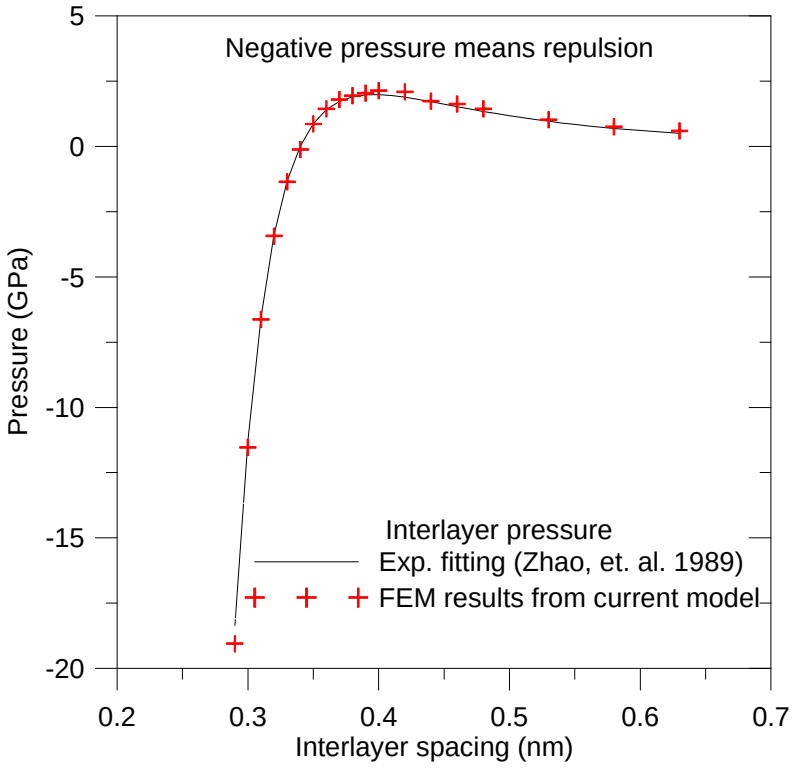

Figure 2.13: Pressure between two graphite layers

(b) Mechanical load transfer between layers of a DWNT

Also to validate the model, the mechanical load transfer from the outer layer in a DWNT to the inner layer is presented here. As shown in Figure 2.14, a DWNT (5,5)@(10,10) is studied. The outer tube is fixed whereas the inner tube is inserted into the outer tube from one end and then pulled out from the other end. The so called capillary force is plotted as a function of the relative sliding length between tubes (Figure 2.15).

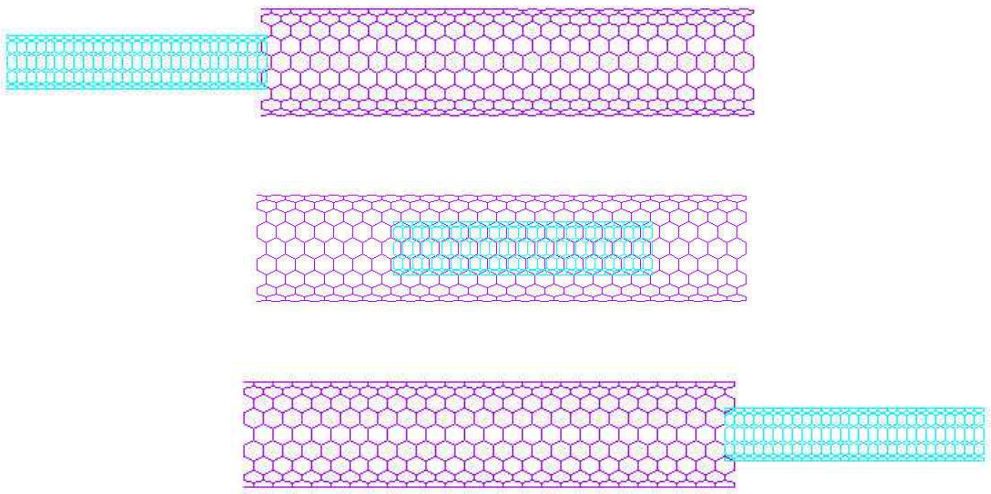

Figure 2.14: Capillary interaction in a DWNT

As expected, when the inner tube is far from the outer tube ends, the force oscillates as the inner tube approaches the outer tube. This mode illustrates the regime where there is only “shear” contribution to the force, since the contact area remains the same. Further displacement of the inner tube gives rise to an increase in the force due to a decrease in the overlap area, i.e., the capillary component appears. Notice that due to a long-range nature of the interlayer interaction, with the cutoff for the van der Waals interaction being about 0.68 nm in our model, the force gradually increases to a

constant level. The retracting force was found to be about 0.8 nN, which is in good agreement of the molecular dynamics results (given by M. Huhtala, 2004) and also in agreement with the experimental values reported by Akita (2003).

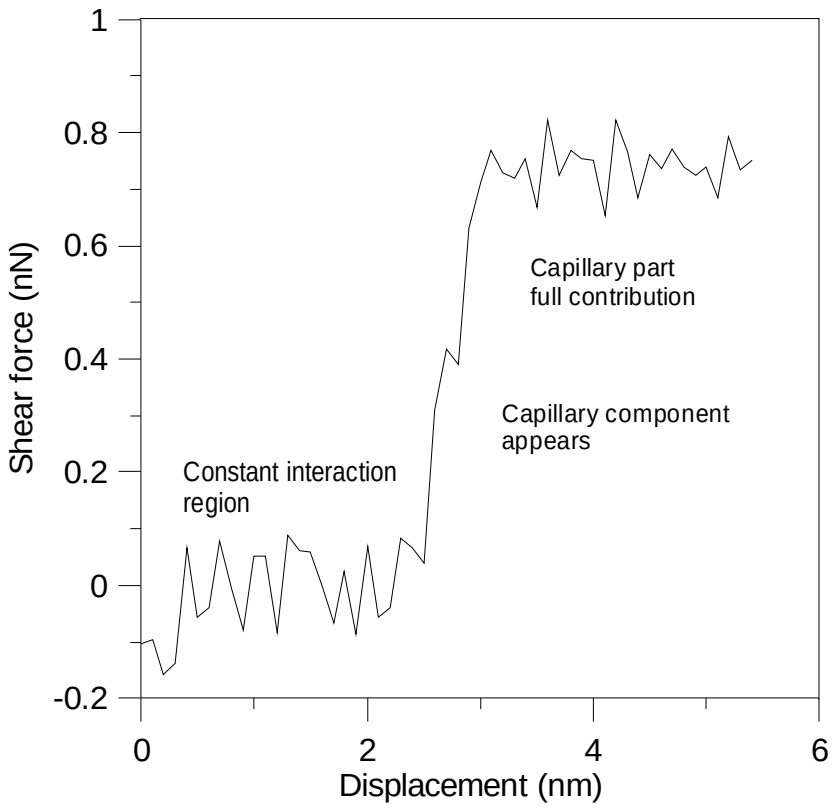

Figure 2.15: Capillary forces between two nested CNT layers in a DWNT

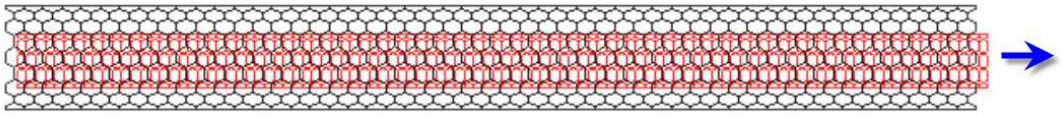

Figure 2.16: Pull out test of a DWNT

(C) Interlayer Shear Strength in a DWNT

In this case, a long (12.6nm) DWNT ((5,5)@(10,10)) is studied to reveal the interlayer shear between the nanotube layers (Figure 2.16). The outer tube is fixed. The inner tube is pulled out from the outer tube. The shear force as a function of the pull out distance is plotted in Figure 2.17. As shown in the figure, the shear force quickly increases to a constant value of about 0.8 nN. The shear strength between tubes is then calculated by dividing the shear force by the tube surface, which gives a constant shear stress of about 15 MPa. Compared to the strength of the MWNT (>1GPa), the interlayer shear strength is very small.

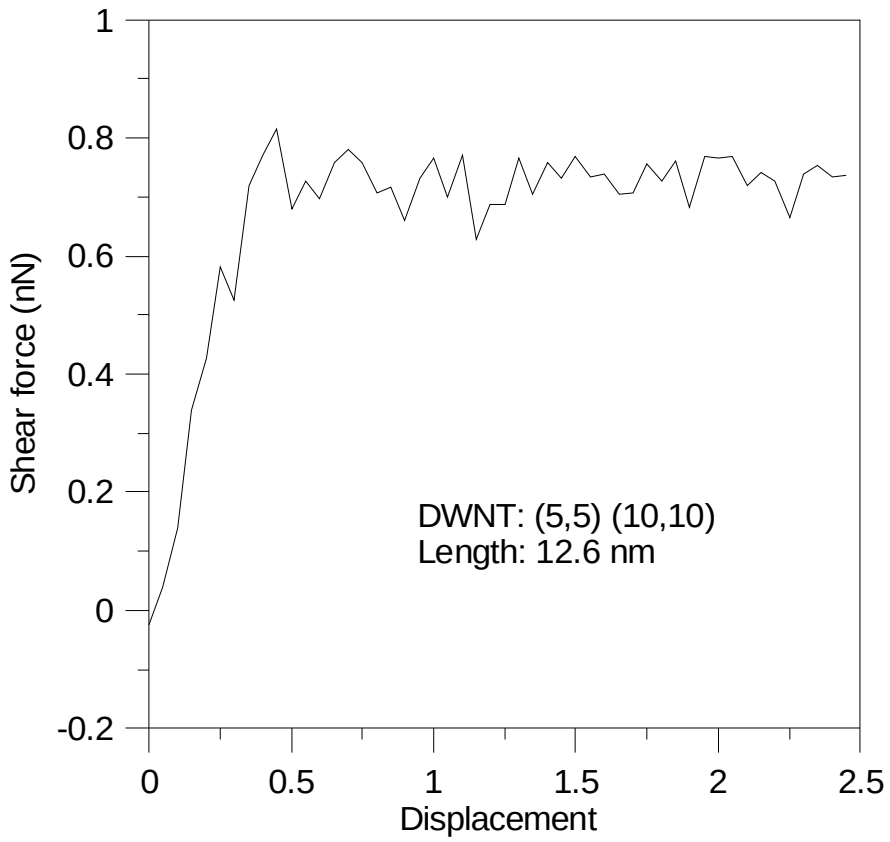

Figure 2.17: Shear stress between two layers in a DWNT (5,5)(10,10)

It is noted that during the insertion and pullout process, reestablishment of the van der Waals interaction between atomic pairs is performed. Because of the sliding movement, new van der Waals pairs come into being and the weak van der Waals

interactions vanish. Therefore, “live” and “dead” technique of elements is adopted in order to simulate the large scale sliding deformation and the mechanical response. Since the ABAQUS Standard module does not support this technique, the current simulation is performed in ANSYS (V10.0). A similar user-defined subroutine is developed for ANSYS using its User-Programmable Features. Also note that the link element (LINK181) is used in ANSYS.

2. 5 Summary

In this chapter, the principle of molecular mechanics is introduced. The structural model (beam-model) of the single-walled carbon nanotube based on the molecular mechanics (developed by Li & Chou, 2003) is investigated which leads to the current model: a modified structural model of the SWNT. Essential to the modified model is the change of the cross-section of the beam element from circular to rectangular. As a result, the bending stiffness of the graphite layer in a CNT can be accurately represented by the modified model. The derivation of the section properties of the rectangular beam element is given based on the energy method, in which the strain energy of rolling a graphite layer into a SWNT is obtained analytically and compared to the results from molecular dynamics simulations.

The modified model is then extended for the study of multi-walled carbon nanotubes (MWNTs) in which the van del Waals interaction between the nested tubes in a MWNT is modeled by a truss element (or spring element) with nonlinear properties derived from Lennard–Jones expression of the van der Waals potential. Numerical experiments such as compression of two graphite layers and sliding of two nanotubes in a double-walled nanotube confirm the validity of the extended model.

CHAPTER 3 : ELASTIC PROPERTIES OF CARBON NANOTUBES

3.1 Introduction

The mechanical properties of carbon nanotubes (CNTs) have been studied through more than a decade worth of both experimental and theoretical studies. In most studies, CNTs have been treated as a model system for the broad study of effective properties in low dimensionality. For example, a CNT can be modeled as a solid beam whose mechanical properties can be characterized by effective constants such as Young's modulus, shear modulus, Poisson's ratio, bending stiffness, etc. A CNT can also be treated as a transversely isotropic continuum (L. Shen and J. Li, 2004) with five effective constants, $\overline{E}_{11}, \overline{\nu}_{12}, \overline{G}_{12}, \overline{K}_{23}$ and $\overline{G}_{23}$ (axial Young's modulus, major Poisson's ratio, longitudinal shear modulus, and plane-strain bulk and in-plane shear moduli). The dependencies of these constants on the CNT's size and chirality have been extensively investigated. In general, the constants depend on the tube size of SWNTs when the tube diameter is small. The current work is, of cause, not intended to simply repeat these results but rather, through the prediction of these effective constants (such as the Young's modulus, shear modulus) to demonstrate the validity of the present model. Furthermore in our simulations, the CNT is treated as a unique object rather than an effective model. Therefore, the application of the current model is not limited to determination of mechanical constants, but can also be extended to the numerical analysis of CNT based devices such as the CNT probe tip used in atomic force microscopy.

The first section of this chapter will present the predictions of effective elastic properties of SWNTs, such as axial Young's modulus, shear modulus and bending stiffness. It is noted that the bending stiffness of SWNTs (and MWNTs) is rarely studied in the literature, to the knowledge of the author. The same elastic properties will be predicted for multi-walled carbon nanotubes in the second part of this chapter.

3.2 Elastic Properties of Single-Walled Nanotubes (SWNTs)

3.2.1 Axial Young's modulus of SWNTs

To predict the axial Young's modulus of a SWNT, numerical tensile experiment is performed. As shown in Figure 3.1 a, bottom end of the nanotube is fixed and an axial force *P* is applied at other end.

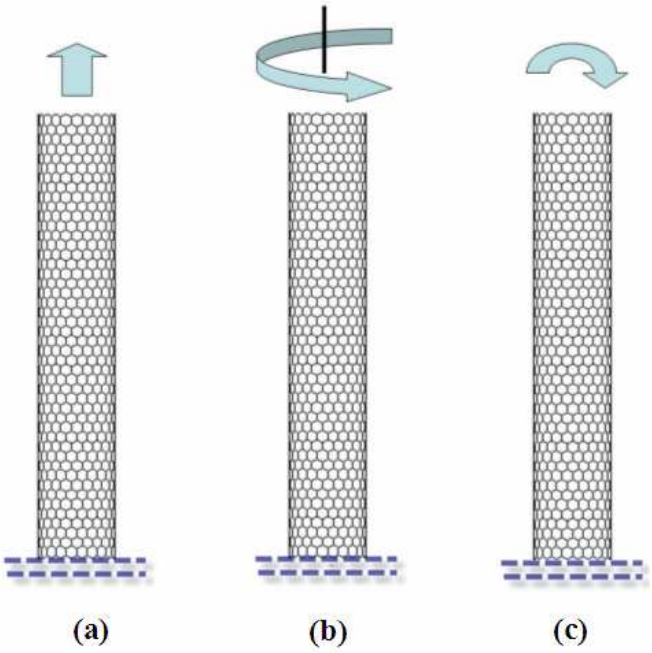

Figure 3.1: Numerical experiments of a SWNT (a) tension; (b) torsion; and (c) bending.

The Young's modulus of the tube can be expressed as the ratio of the normal stress to the normal strain in the axial direction,

$$Y = \frac{P / A_0}{dL / L}, \tag{3.1}$$

where, P stands for the total force acting on the atoms at one end of the tube. dL and L represent the change in tube length and the original length. By assuming an effective thickness t=0.34nm (the interlayer spacing of graphite), the cross sectional area of the tube (A_0) is:

$$A_0 = \pi d_{CNT} t \tag{3.2}$$

where d_{CNT} is the tube diameter.

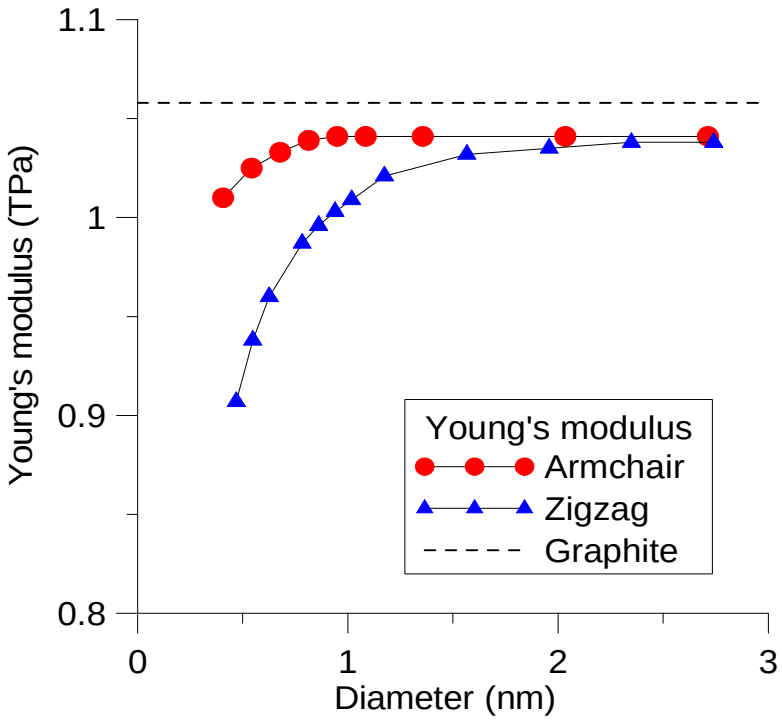

Figure 3.2: Young's modulus of SWNTs versus tube diameter

The result for the Young's modulus as a function of nanotube diameter is plotted in Figure 3.2. Both armchair and zigzag types of CNTs are considered. From the plot, it can be seen that for both armchair and zigzag CNTs, the Young's modulus increases as the tube diameter increases. However, when the tube diameter is greater than 1.5nm, the Young's modulus converges to limiting value, to 1.042TPa for armchair

CNT and 1.035TPa for zigzag CNT. Also the Young's modulus of an armchair tube is slightly higher than that of a zigzag tube. But both of them are close to the in-plane stiffness of a graphite sheet (1.058TPa calculated from the current model) as the tube diameter becomes larger.

The size dependence of Young's modulus seen in Figure 3.2 agrees with conclusions from other methods (T. Chang and H. Gao, 2003; C. Li and T. Chou, 2003; L. Shen and J. Li, 2004; P. Liu, 2004). However, in Li & Chou's work, the Young's modulus of the zigzag tube is higher than that of armchair, which is different from the current finding and Shen and Li's results.

3.2.2 Shear modulus of SWNTs

Experimental measurement of shear modulus of CNTs is not available due to technical difficulties. The shear modulus of a hollow or solid cylinder is the only property which is relevant to the torsion angle per unit length when subjected to a torque. Numerical experiment of twisting a carbon nanotube (Figure 3.1b) is performed to predict the shear modulus of SWNTs in the present work. The SWNT is assumed to be subjected to a torque at one end and is constrained at the other end. Based on the theory of elasticity at the macroscopic scale, the shear modulus of the tube is given as,

$$S = \frac{TL_0}{J_0\theta}, \tag{3.3}$$

where, T stands for the applied torque at one end of the tube, θ represents the twist angle and J_0 is the effective polar moment of inertia of the cross section. Assuming a tube thickness of t=0.34 nm, the polar moment of inertia is obtained as,

$$J_0 = \frac{\pi}{64}\left[(d_{CNT}+t)^4 - (d_{CNT}-t)^4\right] \tag{3.4}$$

The result of the shear modulus as a function of the nanotube diameter is plotted in Figure 3.3.

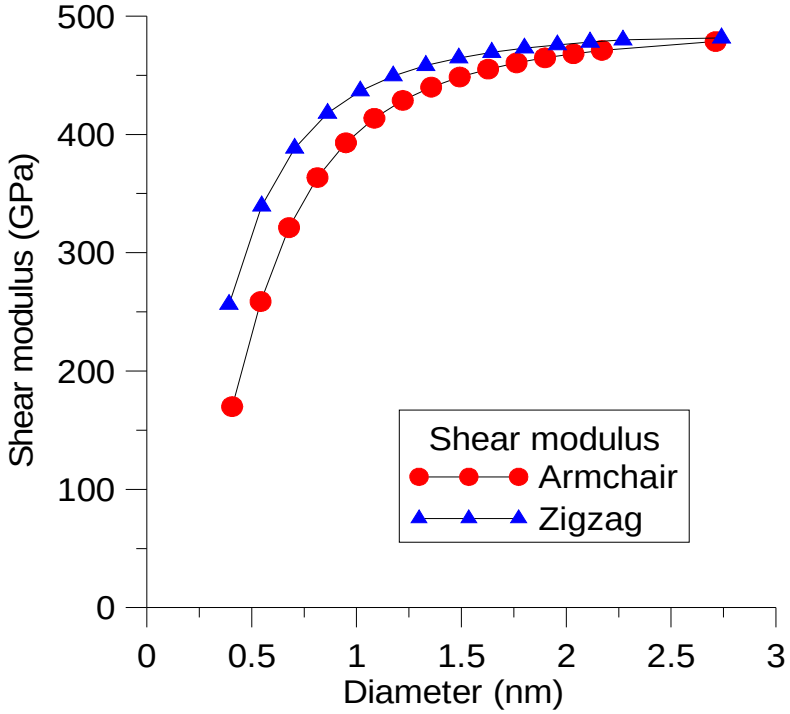

Figure 3.3: Shear modulus of SWNTs versus tube diameter

From Figure 3.3, it can be seen that the shear modulus of SWNTs behaves similarly to the Young's modulus in that it increases with the tube diameter for small tube diameters. At larger diameters (>2nm), the shear modulus becomes insensitive to the tube diameter. There is also somewhat effect of tube chirality (considering the armchair SWNTs and zigzag SWNTs with similar diameters). Unlike the Young's modulus, the shear modulus of the zigzag tube is larger than that of armchair tube for small tube (diameter). As the tube diameter becomes larger, they converge to a certain value of about 490GPa.

The present work agrees with the results of atomistic computation of P. Lu (1997), which is about 478MPa for larger tube diameter, and Popov's result (2000) which is 500GPa.

3.2.3 Bending stiffness of SWNTs

In experimental measuring the Young's modulus of CNTs, the beam theory is adopted where the CNT is treated as a continuum beam member (E.W. Wong, 1996; A. Krishnan, 1998) with the bending stiffness derived from the beam theory. For a beam with hollow cylindrical cross section, it is given as,

$$EI = \pi E\left[(d_{CNT} + t)^4 - (d_{CNT} - t)^4\right]/64, \tag{3.5}$$

where t is the wall thickness of the nanotube ($t = 0.34$ nm) and d_{CNT} is the diameter of the nanotube. The following study will check the feasibility of this approximation.

A numerical experiment is designed to obtain the bending stiffness of the nanotube. As shown in Figure 3.1c, the top end of the nanotube is rotated by a bending angle (θ) whereas the bottom end is constrained. The reaction moment can be obtained from numerical simulation. Then the effective bending stiffness of the nanotube can be given as,

$$D_e = \frac{ML}{\theta}, \tag{3.6}$$

where, the L is the tube length. The comparison of EI and D_e is shown in the Table 3.1, for armchair SWNTs. When calculating *EI*, the Young's modulus is estimated from the simulations in Section 3.2.1 (1.01 TPa to 1.042TPa depending on the tube diameter). The aspect ratio of the tube (L/d_{CNT}) in all simulations is about 10 to exclude the influence of tube length. The results using the original beam-model are also listed in the table for comparison.

Table 3.1: Effective bending stiffness of SWNT (armchair)

tube	d_{CNT} (nm)	EI (10^{-24} N.m^2)	D_e (10^{-24} N.m^2)	*Original beam model***
(3,3)	0.407	15.557	9.396	10.029
(4,4)	0.542	30.282	23.161	23.566
(5,5)	0.678	53.504	44.697	45.994
(6,6)	0.814	87.033	74.365	77.545
(7,7)	0.949	132.043	119.932	122.251
(8,8)	1.085	193.757	180.653	182.212
(9,9)	1.221	272.619	255.446	257.605
(10,10)	1.356	368.847	347.688	348.564
(15,15)	2.034	1203.962	1173.693	1147.655

*** The value is obtained by calculations using the original sectional properties (given by C. Li and T. Chou 2003)*

From the table, it is seen that the effective bending stiffness can be overestimated by using *EI* for nanotubes with small diameter. The difference can be as much as 50% for tubes with small diameter (0.4nm). The bending stiffness of the tube is dominated by the in-plane stiffness of the nanotube wall since no big difference between the current beam model and the existing beam model (C. Li and T. Chou, 2003) is observed. It is noted that the CNTs considered in the experimental work (Wong, 1996; Krishnan, 1998) have much larger diameters, therefore the effective bending stiffness for beam member can be fairly accurate.

3.3 Elastic Properties of Multi-Walled Nanotubes (MWNTs)

3.3.1 Axial Young's modulus of MWNTs

The Young's modulus of a multi-walled carbon nanotube is also studied using the same method developed for SWNTs. If the thickness of each tube layer is taken as the interlayer spacing of graphite (t=0.34nm), the effective cross-sectional area of the

tube is given as,

$$A_0 = \frac{\pi}{4}\left[(d_o + 0.34)^2 - (d_i - 0.34)^2 \right], \tag{3.7}$$

where d_o, d_i represent the outmost tube diameter and the innermost tube diameter, respectively (see Figure 3.4). The Young's modulus is then expressed as,

$$Y = \frac{P / A_0}{dL / L}, \tag{3.8}$$

where P stands for the total force acting on the atoms at one end of the MWNT. dL and L represent the change of tube length and the original length.

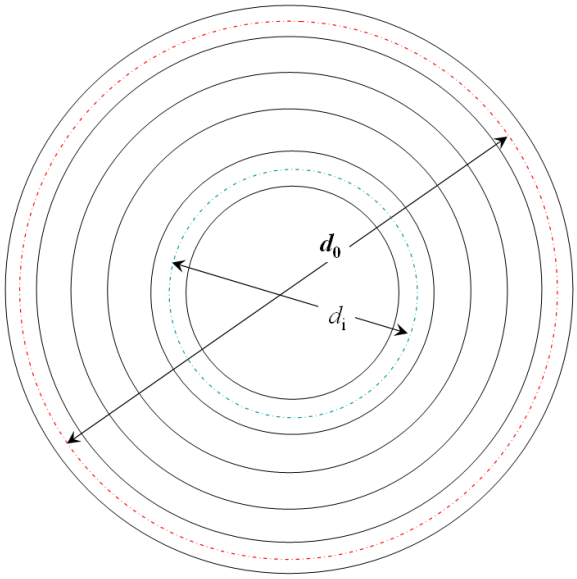

Figure 3.4: Diameters of a MWNT

In this section, first the Young's modulus of the double-walled carbon nanotube is simulated. The outer diameter of the DWNT is changed to study the effect of tube size. For convenience it is assumed that both layers are commensurate, ie., both tubes have either armchair chirality or zigzag chirality, although incommensurate MWNTs are more commonly observed in experiments.

Figure 3.5 shows the variation of the Young's modulus of DWNTs considering different outer diameters of DWNTs. As shown in the figure, there is a slight increase in the Young's modulus as the diameter increases. The Young's modulus of DWNTs is generally higher (about 9%) than that for single-walled carbon nanotubes. To study the effect of van der Waals force on the Young's modulus, a model is constructed without considering the van der Waals interaction between tubes. That is, a (5, 5) tube independently nested in a (10, 10) tube is studied. The resulting Young's modulus is 1.037TPa, which is the average of Young's moduli of (5,5) SWNT (1.033TPa) and (10, 10) SWNT (1.041 TPa). However, when van der Waals forces are taken into account, the Young's modulus obtained (1.122TPa) is higher than that of either constituent tube.

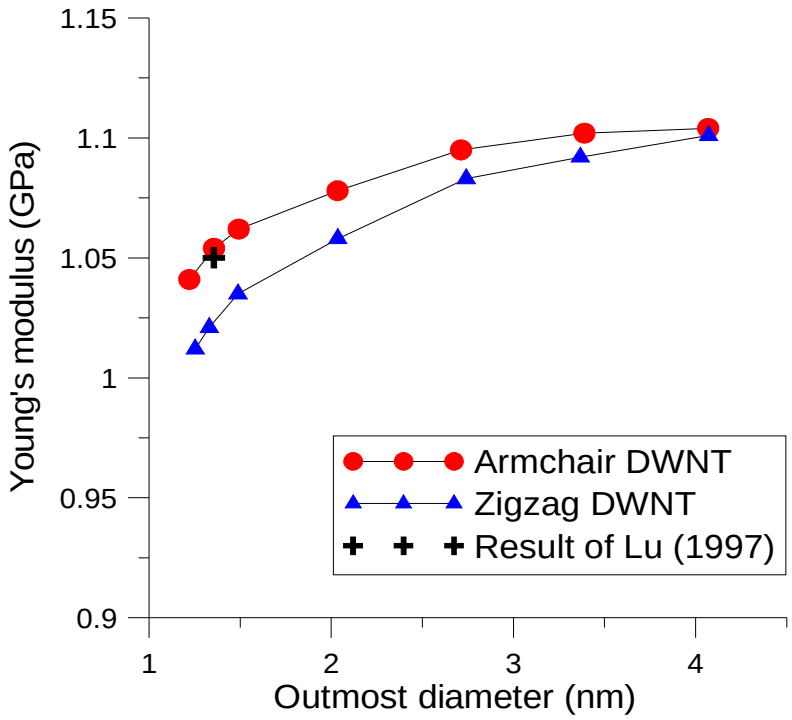

Figure 3.5: The effect of tube diameter and tube chirality on the Young's modulus of DWNTs

The result for the DWNT (5, 5)@(10, 10) is compared with the result of J. Lu (1997) using the empirical force-constant model. The present result (1.122TPa) is slightly higher than his prediction (1.05 TPa)). It is noted that the Young's moduli obtained by

J. Lu (1997) are generally lower than those obtained in other theoretical predictions. While Lu's results show an increase of about 11% for the DWNT's modulus relative to that of SWNT, the present result shows a 9% increase only.

The effect of the number of layers in a MWNT is also studied. The outmost diameter of the MWNT is fixed. For convenience, the outmost layer of the tube is assumed to be (25, 25) with a diameter of 3.39 nm for the armchair MWNT and for the zigzag MWNT, the outer tube is assumed to be (43, 0) with a diameter of 3.37nm (Table 3.2). The Young's modulus of MWNTs as a function of the number of layers in the tube is plotted in Figure 3.6. The maximum number of layers considered is five.

Table 3.2: The MWNTs used in the computations

Layers	Armchair	Zigzag
1	(25,25)	(43,0)
2	(20,20)(25,25)	(34,0)(43,0)
3	(15,15)(20,20)(25,25)	(25,0)(34,0)(43,0)
4	(10,10)(15,15)(20,20)(25,25)	(16,0)(25,0)(34,0)(43,0)
5	(5,5)(10,10)(15,15)(20,20)(25,25)	(7,0) (16,0)(25,0)(34,0)(43,0)

Figure 3.6 shows that as the number of layers in a MWNT increases, the Young's modulus increases but converges to a value of about 1.13 TPa for both armchair and zigzag MWNTs. Also implied is that the effect of chirality is weaker as the number of layers in a MWNT increases. That means the MWNT becomes more homogeneous with more layers.

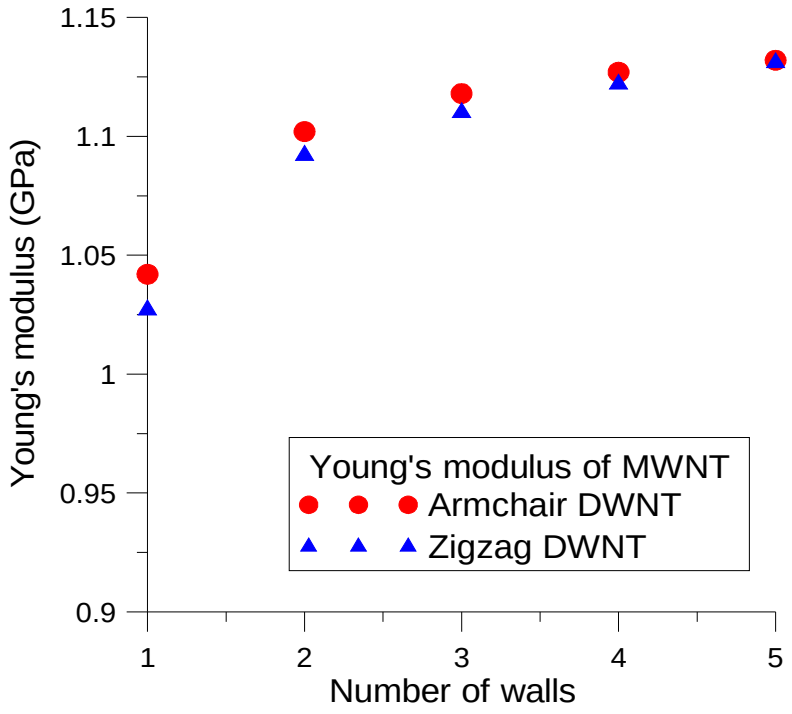

Figure 3.6: The effect of the number of tube layers on the Young's modulus.

3.3.2 Shear modulus of MWNT

To predict the shear modulus of MWNTs, the numerical experiment of twisting a MWNT is performed. It is assumed that the torque T is applied only on the outermost wall of the MWNT. The loading is transferred to the inner tubes through the shear stress in the circumferential direction caused by the van der Waals interactions corresponding to the relative torsion among tubes. The shear modulus of the MWNT can then be expressed as:

$$S = \frac{TL_0}{J_0\theta}, \tag{3.9}$$

where the polar moment of inertia, J_0 is expressed as,

$$J_0 = \frac{\pi}{2}\left[\left(\frac{d_0 + t}{2}\right)^4 - \left(\frac{d_i - t}{2}\right)^4\right], \tag{3.10}$$

where d_0 and d_i are the diameters of the outmost and innermost tubes (see Figure 3.4)

and t is the thickness of single layer ($t = 0.34$ nm).

The double-walled carbon nanotube (DWNT) is studied first. Figure 3.7 shows the variation of the shear modulus with the diameter of the outmost tube. It is seen that as the diameter increases, the shear modulus of the DWNT increases slightly. However, compared to that of a SWNT with the same diameter, the shear modulus of a DWNT is about 10% smaller in general.

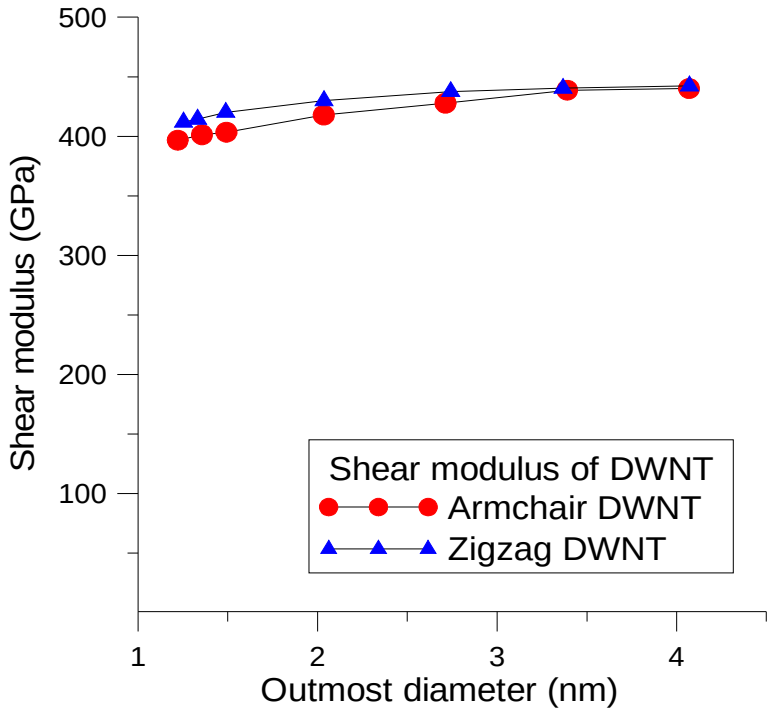

Figure 3.7: Shear modulus of a DWNT versus outmost tube diameter

The variation of the shear modulus with the number of layers in a multi-walled carbon nanotube is also studied (Figure 3.8). The innermost tube is fixed as an armchair tube (5, 5). Then a MWNT with n layers can be expressed as $(5n, 5n)_{n=1,2..5}$. It is seen that the shear modulus of a MWNT decreases with the number of layers of the MWNT. However, the value converges to 430 GPa for a MWNT with more than 5 layers.

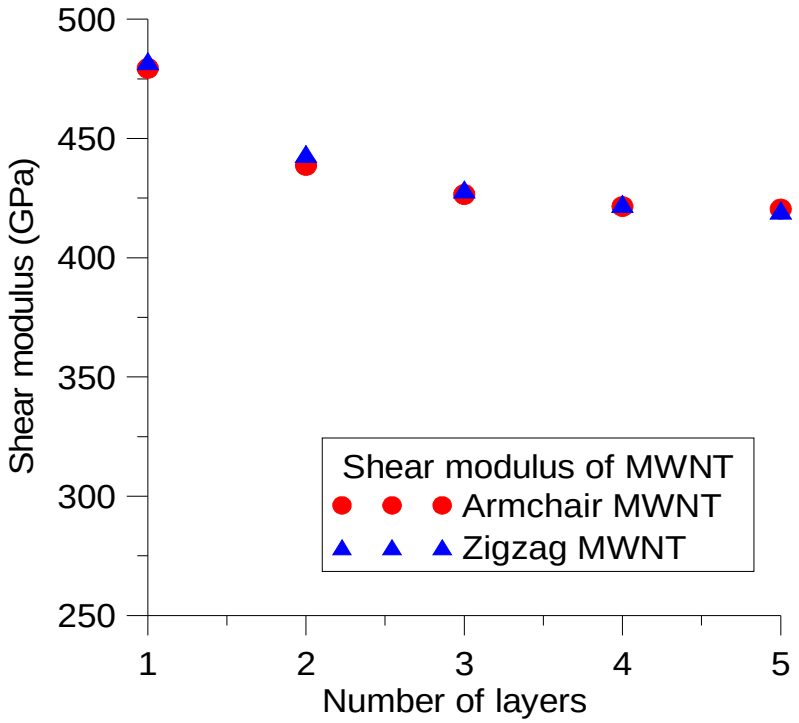

Figure 3.8: Shear modulus of a MWNT versus the number of layers

3.3.3 The effective bending stiffness of MWNTs

The effective bending stiffness of MWNTs is studied here by numerical experiment of bending of a MWNT. Similar to that of SWNTs, the bending angle (θ) is applied at one end of a MWNT, whereas the other end is constrained. The reaction moment is *M*. The effective bending stiffness of an MWNT is then obtained as $D_e = ML/\theta$. The value of *EI* is also calculated where the moment of inertia of the cross-section of a MWNT is given by $I = \left[(d_0 - t)^2 - (d_0 - t)^2\right]/64$.

The effective bending stiffness of DWNTs is then simulated. Tables 3.3 and 3.4 list the bending stiffness for DWNTs of armchair and zigzag types, respectively. From the tables, it is seen that the bending stiffness of a DWNT increases as the tube diameter increases. A DWNT is more bending resistant that a SWNT with the same outer diameter. The bending stiffness can be effectively approximated by *EI* when the tube

diameter is larger than 3nm with an error less than 10%.

Table 3.3: Effective bending stiffness of DWNTs (armchair)

DWNT	Outmost diameter (nm)	EI (10^{-24} N.m^2)	D_e DWNT (10^{-24})N.m^2)	D_e of SWNT
(5,5)@(10,10)	1.356	405.684	388.151	347.688
(10,10)@(15,15)	2.034	1507.594	1481.495	1173.693
(15,15)@(20,20)	2.712	4018.665	3938.564	2786.558
(20,20)@(25,25)	3.39	8285.804	8183.053	5428.174

Table 3.4: Effective bending stiffness of DWNTs (zigzag)

DWNT	Outmost diameter (nm)	EI (10^{-24} N.m^2)	D_e (DWNT) (10^{-24} N.m^2)	D_e (SWNT)
(7,0)@(16,0)	1.253	325.963	290.914	265.87
(16,0)@(25,0)	1.958	1385.637	1295.848	1146.610
(25,0)@(34,0)	2.662	3794.144	3600.274	2518.471
(34,0)@(43,0)	3.367	8162.595	8124.53	5140.844

3. 4 Summary

In this chapter, the mechanical properties of carbon nanotubes (SWNTs and MWNTs) have been studied. Effective constants such as the axial Young's modulus, shear modulus and bending stiffness have been obtained through numerical experiments (axial tension, torsion and bending). The following is a brief summary of the results.

(a) The axial Young's modulus of a SWNT is found to be around 1 TPa. For SWNTs with small diameters (<1nm), the value shows dependence on the tube diameter (and certainly on tube chirality) in that smaller SWNTs have smaller Young's modulus. The armchair tube is found to be slightly more rigid than the zigzag tube especially when the tube diameter is small.

(b) The shear modulus of MWNTs is predicted to be less than half of that of the Young's modulus. Also similar dependence on the tube diameter is found for tubes with small diameter (<1nm). Armchair tubes have smaller shear modulus than the zigzag tube, in contrast to the value of Young's modulus.

(c) The effective bending stiffness (D_e) of a SWNT as a structural beam member is also studied. The results indicate that D_e can be approximated by *EI* for tubes with large diameters (>3nm), where

$$I = \pi\left[(d+t)^2 - (d-t)^2\right]/64.$$

(d) The Young's modulus and shear modulus of MWNTs have been predicted. The results show similar dependence on tube diameter and chirality as was found for SWNTs. Both Young's modulus and shear modulus of DWNTs are slightly higher than those of SWNTs with similar size.

(e) The bending stiffness of DWNTs is also studied. It is found out that for DWNTs with outer diameter larger than 3nm, the effective bending stiffness of the tube can be approximated by the continuum value *EI*.

CHAPTER 4 : BUCKLING BEHAVIOR OF CARBON NANOTUBES

4.1 Introduction

Buckling of carbon nanotubes (CNTs) have been observed in experiments where the tubes act either as stand-alone or load-bearing elements embedded in host materials (Figure 4.1). Buckling can be driven by large deformations in the form of axial compression, bending and torsion applied on a carbon nanotube. For CNTs in nanoscale devices and CNT reinforced composites, buckling can be induced by large stress and deformation due to thermal or lattice mismatch between different materials. Since CNTs are very resilient, their buckling behavior is elastic i.e., it can be completely recovered after unloading, as suggested both by experimental and theoretical studies (P. Poncharal, 1999; M.R. Falvo, 1997; and T.W. Tombler, 2000). However, the structural integrity of the nanotube can be significantly reduced due to buckling. On the other hand, the physical properties of CNTs such as electrical conductance can be significantly changed by occurrence of buckling (H.W. Postma, 2001), which lead to potential applications of CNTs as the next-generation nanoelectronic devices (nanotransistors) (H.W. Postma, 2001), nanofluid components (nanovalves) (M. Grujicic, 2005), and reversible elements in nanoelectromechanical systems (NEMS) by switching between the buckled and normal states.. Also, the chemical reactivity at the local buckling site (kinks) can be dramatically enhanced. This has been studied both in simulation and experiments (Srivastava, 1999). All these phenomena can have significant impact on the design of NEMs devices, particularly for applications involving manipulations of nanometer-sized objects that might lead to highly local deformation. Therefore, in view of both the mechanical

integrity and applications, it is necessary to understand their buckling mechanisms under mechanical loads. More importantly, such study may provide insights into the way to initiate / control or prevent buckling of CNTs depending on the specific application.

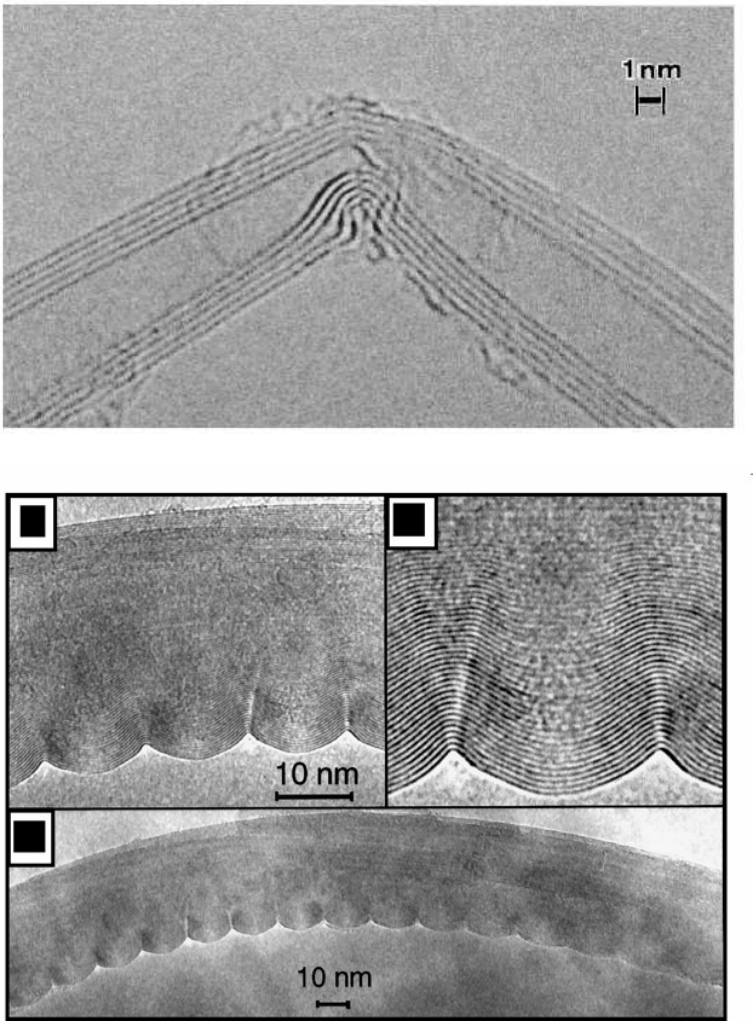

Figure 4.1: Experimental observations of buckling (kinks) of MWNTs by High Resolution Electronic Microscopy (HREM).

Through recent (mostly last few years), our understanding of CNTs' buckling behavior has improved, especially with the help of many theoretical modeling and simulation works. Compared with multi-walled carbon nanotubes (MWNTs), the buckling behavior of SWNTs has been better understood since direct molecular

dynamics (MD) simulations of SWNTs are more economical to perform. Nevertheless, with the help of many continuum, quasi-continuum models and simulations, as well as molecular mechanics simulations both the buckling mode and the critical buckling loads (strain, bending and torsion angles) can be well predicted. For MWNTs, direct simulation of systems with a large number of atoms seems prohibitive due to computational time and cost. To our knowledge, no direct MD simulation for the mechanical behavior of MWNT's with layers more than 7 has been reported in literature. Therefore, continuum models based on multi-shell and multi-beam theories have been developed to study the buckling behavior of MWNTs. Other approaches (including the current molecular structural model developed here) lie between the MD simulations and the continuum models have also been developed. The basic idea of these approaches is the continuum representation of the atomistic potentials based on molecular mechanics (MM), and then solving the buckling problem using continuum mechanics. The advantages of these approaches are their cost-effectiveness (over the direct MD simulations) and their ability to characterize the lattice structure of CNTs (compared to shell-model and beam-model). Owing to these advantages, a comprehensive study of the buckling behavior of CNTs with large degree of freedoms (DOFs) and many layers becomes more practical. In the present work, we will implement the current developed model (molecular mechanics based) into the finite element numerical calculations to study the buckling behavior of CNTs under compression and bending. Issues such as the effect of geometry, size and boundary conditions used in the simulations on the buckling behavior will be studied. Note that these numerical simulations, axial compression and pure bending studied here (as well as in almost all theoretical studies in the literature) are very simple and quite different from the real cases studied experimentally. However, it is expected that through these fundamental case studies, the intrinsic characteristics of buckling behavior of CNTs can be revealed, since the current developed approach can be used to simulate the more complicated cases where CNTs modeled as a structural system are subjected to a combination of compression, bending and torsion.

The text of the chapter is organized as follows. For convenience, a comprehensive overview of the literature about buckling studies of CNTs is not given. Instead, review of the state-of-art work of every topic will be addressed in the respective section. The first part of the chapter will discuss the buckling behavior of SWNTs under compression and bending, respectively. Topics such as the effects of geometrical perturbation, length effect, boundary conditions will be addressed. The second part of the chapter will be devoted to studying the buckling behavior of MWNTs under compression and bending. The effect of thickness of MWNTs on the buckling modes will be considered. Different buckling modes peculiar to MWNTs such as "all-together" mode and "part-forward" mode will be discussed. Finally, a summary will be given to summarize the chapter.

4.2 Axial Compressive Buckling of Single-Walled Carbon Nanotubes (SWNTs)

4.2.1 Literature review

Most studies of the buckling of CNTs in the literature have considered the axial compressive deformation, because it is more fundamental than other deformation modes such as bending and torsion. For bending buckling, kinks (or wrinkles, ripples) can be developed on the compressive side, which is somehow related to the compressive instability of the atomic bonds. When a long slim beam (or column) is subjected to compressive load at the end, it can buckle sideway if a critical load is reached. A SWNT can be viewed both as a beam or a hollow tube depending on the aspect ratio (L/D) and the section ratio (D/t). Therefore, the buckling mode can have three distinct categories. For SWNTs with small aspect ratios and large section ratios, shell-buckling (or kinks, snipping) may develop (Figure 4.2a). Such kinking behavior is local in contrast to beam-buckling (or column-buckling) behavior of SWNTs with large aspect ratios and small section ratios (Figure 4.2c). Besides shell-buckling and beam-buckling, mixed-buckling mode is also possible for SWNTs with relative medium aspect ratios and section ratios (Figure 4.2b).

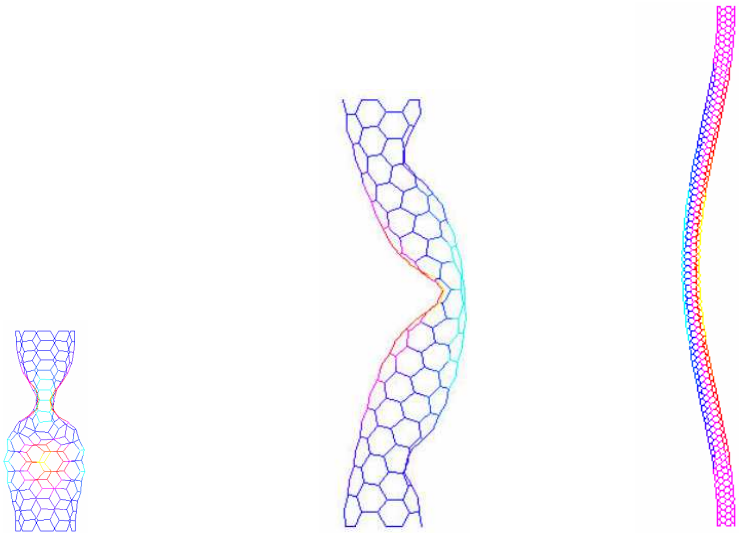

(a) Shell-buckling; (b) Mixed buckling; (c) Beam buckling

Figure 4.2: Different buckling behaviors of a SWNT subjected to axial compressive load.

The experimental study of buckling behavior of CNTs remains a challenge because of the difficulties in manipulating nanostructures. So far, very limited information can be extracted from the recently developed approaches such as nano-indentation of CNTs to determine the critical load of CNTs under compression (H. Qi, 2003; J.F. Waters, 2004). Most studies have been theoretical and numerical which can be roughly divided into three categories: (a) Atomistic simulations based on the molecular dynamics (MD), with either classical or reactive empirical bond order potential; (b) continuum mechanics modeling where CNTs are effectively modeled as a continuum (beams or shells); and (c) molecular mechanics (MM) methods (including MM based structural methods).

In many cases, MD simulations yield direct and accurate results for mechanical behavior of CNTs (such as Young's modulus). However, due to limitation in time and length scales, they are not very efficient in investigating the buckling behavior of long SWNTs, MWNTs, or CNT bundles where a large number of atoms have to be simulated. Direct molecular mechanics computations have also been performed

recently (G. Cao, 2006; A. Sears, 2006). But the solution stability and convergence depend on the selection of load increment in solving the buckling load (strain), as reported by G. Cao (2006). The continuum modeling of beam-buckling and thin-shell buckling, on the other hand (C. Ru, 2002; C. Wang, 2004; X. Wang, 2004; A. Pantano, 2004), offers simple and fast solutions, which includes both analytical and FEM solutions. However the discrete lattice structures of CNTs can not be considered in these models. Therefore the accuracy of the predictions remains questionable. For these reasons, a few analytical and numerical models based on molecular mechanics have been developed (C. Li, 2003; T. Chang 2006) to study the compressive buckling of CNTs, in which the characteristic chiral structures of the CNTs can be addressed and atomic interactions of the discrete structure are represented by continuous potentials. The analytical model developed by T. Chang (2006) can not predict the length effect of the buckling behavior since only representative pieces with a few carbon atoms are considered. A full-length simulation is needed since the buckling can be both local (shell-buckling) and global (beam-buckling) depending on the tube length. The molecular structural model of CNTs (C. Li, 2003) was also used to simulate compressive buckling (C. Li, 2004). However, as stated in the previous chapter, the beam element used in the model can not correctly represent the bending capacity of the nanotube wall. Consequently, the shell-buckling and the mixed-buckling modes of the tube can not be correctly predicted.

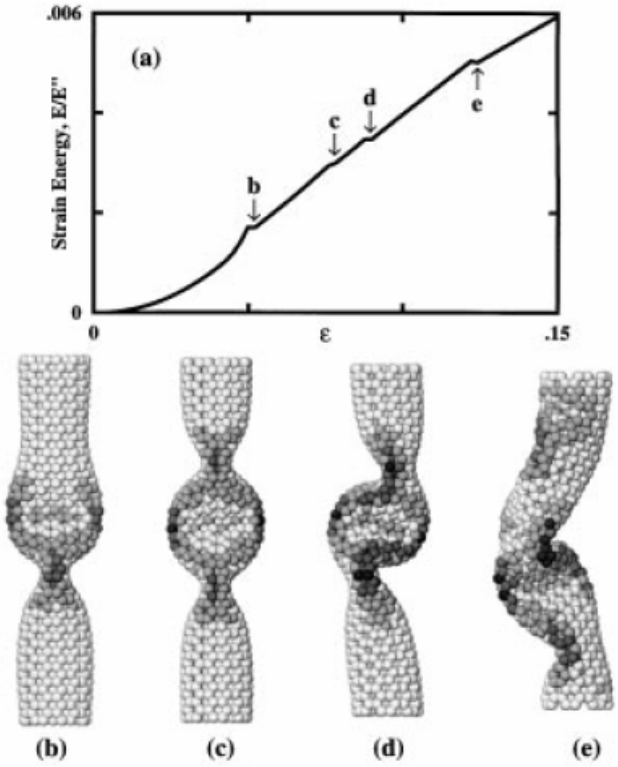

Figure 4.3: Buckling of a (7,7) nanotube under compression, simulated by MD (B. Yakobson, et. al., 1996); tube length is about 6 nm.

Besides the differences in modeling and simulation, many of the conclusions and results of CNTs' buckling behavior are in contradiction with each other. The earliest report on CNT buckling behavior was given by B.Yakobson et al. (1996). Buckling behavior of SWNTs under axial compression, bending and torsion were simulated by MD (Figure 4.3). For example, the axial compressive buckling of a (7, 7) zigzag SWNT (~6 nm long) was studied and it was found that 5% deformation would trigger a so called "two-flattening" pattern buckling in the mid of the tube. The same example was studied many years later by Q. Wang *et al*. (2005), using continuum modeling. It was shown that the first buckling mode would be a "beam-like" mode in which the tube preserves its circular cross section and buckles sideways as a whole. M. Buehler et al. (2004) reported that the critical buckling strain (axial compression) of SWNTs decreases with decreasing tube length, but B.Yakobson et al. (1996) reported length-independence. Moreover, results of critical load (strain or curvature) from

different reports disagree with each other for nanotubes with very similar configurations, which may be due to sensitivity dependence of buckling load on the perturbation imposed on CNTs in order to favor the occurrence of buckling. From these results, it is difficult to deduce a clear relationship between critical buckling loads (compressive strain or bending angle) and the geometry of CNTs, such as the tube chirality, length and diameter.

The onset of buckling shows a strong dependence on the geometrical defects artificially imposed to the perfect crystalline structure of a CNT. In theoretical studies, the initial structures of SWNTs are assumed to be perfect, with carbon atoms located exactly at the equilibrium location (the C-C bond length is about 0.142nm). However, to study the buckling behavior, it is necessary to impose artificial geometric imperfections (geometrical defects) onto the perfect lattice structure of a CNT. Artificial geometrical imperfection can be generated by several approaches: (a) A common practice used in the finite element analysis of postbuckling behavior of a structure is a two-step procedure. As a first step, a linear buckling (or eigenvalue buckling, bifurcation buckling) analysis is performed. Based on the linear buckling modes, a geometric perturbation with slight offset from the perfect structure is imposed artificially in the second step to favor the onset of postbuckling (non-linear) response. (b) Sinusoidal perturbation with a sinusoidal function of different wave numbers on both the circumference and axial directions can also be imposed. Such approach is widely implemented in the buckling analysis using classic thin-shell theory. (c) Random noise-like perturbations can also be adopted, with the advantage that they do not favor a buckling mode. In MD simulations for example, such noise-like perturbation can be created during the process of equilibrium iteration of each load step. The perturbation amplitude in a MD simulation depends on a preset threshold of the net force (very close to zero) between atoms. However, this approach sometimes does not work well, in that they sometimes inhibits the growth of a buckling mode and must be performed numerous times to insure that the lowest critical buckling load (or strain) is found. This can dramatically increase the already

high cost of MD and MM simulations. No matter what perturbation approach is adopted, the mode and amplitude of the perturbation are critical in predicting the buckling of SWNTs. In general, the predicted buckling load increases with decreased perturbation amplitude. On the other hand, if the amplitude of perturbation is fixed, the buckling load and mode may vary with different patterns of geometrical perturbation. Different perturbation patterns have to be attempted to ensure that the lowest buckling load (intrinsic buckling load) is found.

The dependence of the critical load on perturbation has been inadequately discussed so far in the literature, although it was recently mentioned in a few reports. A. Sears (2006) mentioned the dependence on perturbation when they studied the axial compressive buckling of CNTs by MM method. But the perturbation sizes were not properly chosen in that a geometric defect of 0.5% of tube length was chosen for all nanotubes they studied. For longer tubes, the perturbation becomes larger and is thus not acceptable. In the present study it will be shown that choosing a perturbation size based on the number of atoms (or the surface area) of the nanotube would be more reasonable, instead of basing it on the nanotube length only. G. Cao (2006a) in their MM simulation of CNTs under compression argued that the perturbation defects can be accumulated during the equilibrium solution for every incremental step. The accuracy of the prediction depends on the selection of a proper displacement increment. They then gave a solution in another paper (G. Cao,2006b) in which the effect of defect accumulation can be reduced by adopting a targeted molecular mechanics method. However, the perturbation amplitude related to a threshold (nearly zero) of the net force between atoms was not given explicitly. Note such obscurity is common in MD computations as well.

It is the objective of the current section to give a comprehensive study of the buckling of SWNTs under axial compression. Special emphasis is placed on the discussion of perturbation sensitivity and the effect of the size/structure on the buckling behavior.

4.2.2 Simulation method and procedure

Numerical experiments of compressive buckling are carried out in the current work. Two different load cases with different end-restraints are studied: one-end restraint (Figure 4.4 a) and two-end restraint (Figure 4.4 b). In the one-end restraint case, an individual SWNT is clamped at one end and axial load is applied on the other end to generate buckling. This case is similar to the nano-indentation experiment (Qi, 2003) although in the experimental setup lateral bending force is also applied. More often, the two-end constrained case is studied in the literature, where the lateral displacements of both ends of the CNT are restrained and compression is applied. The present study will focus on the two-end restrained case.

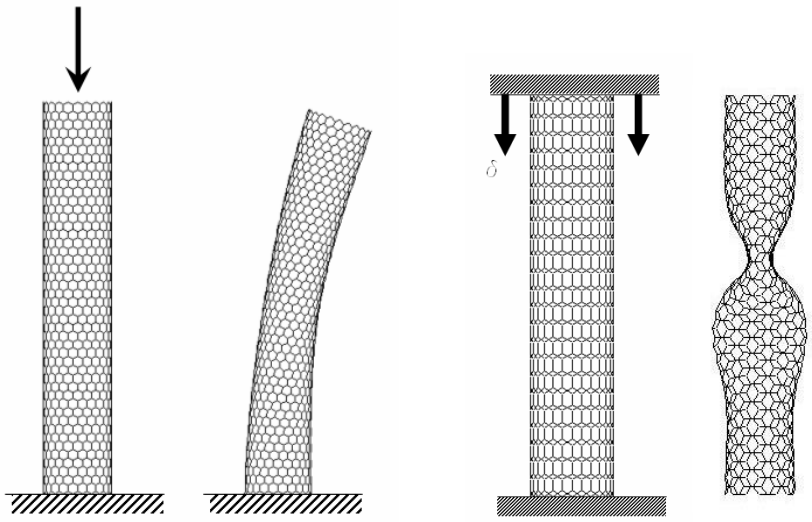

(a) one end clamped; (b) both ends clamped

Figure 4.4: Nanotube under axial compressive load (different end restraints)

The initial structures of SWNTs are assumed to be perfect. The atoms are located exactly at the place of equilibrium and the C-C bond length is assumed to be 0.142nm. The real topological tube defects, such as atomic vacancies or the Stone Wales defects (i.e., pentagon and heptagon pair by rearrangement of the bonds), are not considered although they can significantly reduce the buckling load. Note that by ignoring these

factors in the present study, the fundamental and intrinsic relationship between the critical buckling strain and tube geometrical parameters can be explored. The predicted results may be subsequently revised by incorporating the fitting parameters to include the effects of topological defects, temperature, etc.

The SWNT is constructed by beam elements with the sectional properties derived in Chapter 2. A geometrical perturbation with certain amplitude and mode is imposed on the structure. Compressive strain is gradually imposed until buckling is triggered. With the help of ANSYS Parametric Design Language, a descript code is developed to conveniently generate SWNTs with different size and chirality structures. The structural model with the proper boundary conditions and load is then solved either by ANSYS or ABAQUS (with the self-designed ANSYS-ABAQUS interface).

The buckling can be identified from both observation of the deformed shape of the SWNT (Figure 4.4 b) and from analyzing the strain energy – strain curve. For example, the strain energy as a function of applied strain for a (7, 7) SWNT (~ 6nm long) under compression is plotted in Figure 4.5. It can be seen from the figure that at small strains, the strain energy grows parabolically with strain ($\sim \varepsilon^2$). At buckling, the strain energy abruptly drops about 25% and it enters into the postbuckling stage. The strain energy then increases approximately linearly, until the nanotube buckles the second time (collapse). The mode of post-buckling refers to the configuration in which large lateral deflection of the tube occurs to relieve the compression energy, since bending uses much less strain energy.

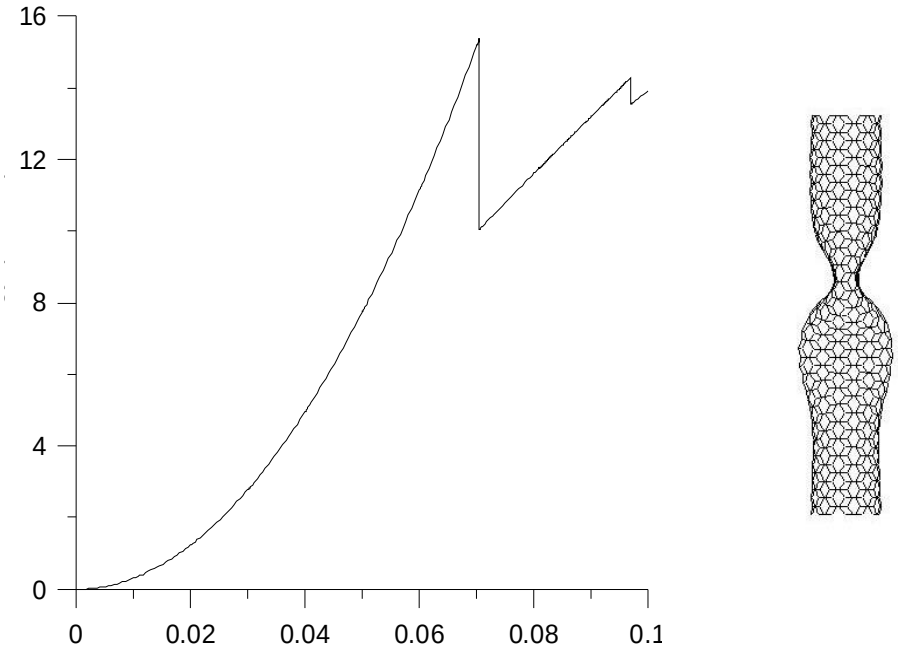

Figure 4.5: Strain energy versus the axial strain of nanotube (7, 7), 6nm long

4.2.3 The effect of perturbation on the compressive buckling behavior of SWNTs

To study the effect of perturbation, the current study will use all three perturbation approaches (a, b, and c) mentioned earlier. For each perturbation method, the effect of the perturbation size (amplitude) and pattern are discussed in detail. The noise-like perturbation (method c) is found not to be very effective. Methods (a) and (b) yield very similar results provided that in method (b) a suitable pair of wave numbers in the circumferential and axial directions is chosen. The details are presented in the following discussion.

(a) Two-step perturbation

In this two-step perturbation approach, first the linear buckling (or eigenvalue buckling, or bifurcation) analysis of a SWNT is carried out by applying a unit axial displacement on the top ring. The first four linear buckling modes are obtained and shown in Figure 4.6. Then the coordinates of the original prefect geometry of the SWNT are regenerated by superimposing the linear buckling shape(s) obtained from

the linear buckling analysis. The amplitude of the perturbation is represented by a certain small multiplier (or percentage) of the imposed linear buckling mode(s). For example, for the i^{th} linear buckling mode, the regeneration of coordinates can be achieved by the command "*UPGEOM, amp, mode_i…*" in ANSYS. In which "*amp*" represents a weight multiplier of the linear buckling mode.

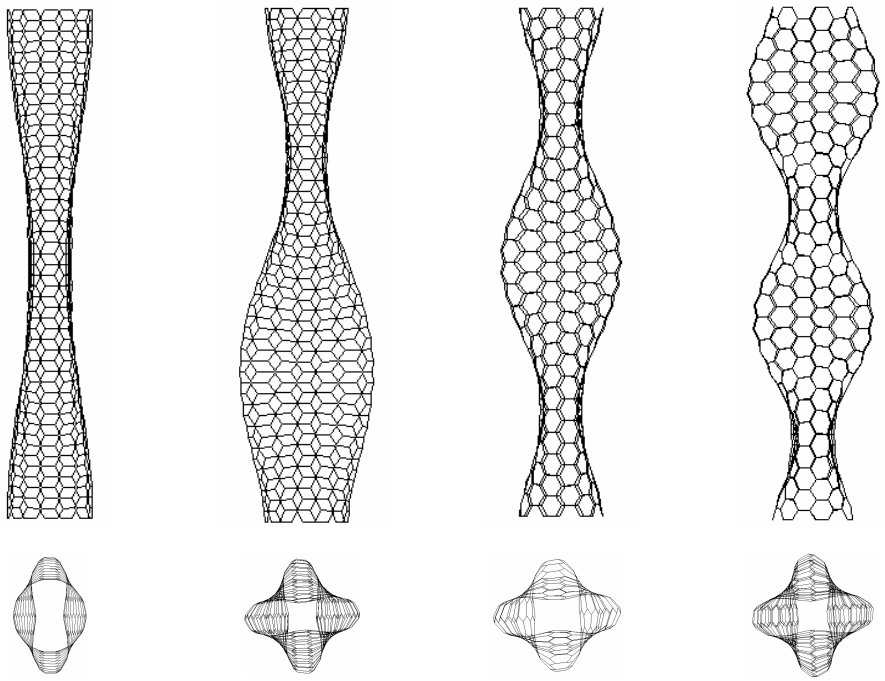

Mode I (One-fin) Mode II (Two-fin) Mode III (Three-fin) Mode IV (Four-fin)

Figure 4.6: The first four buckling modes predicted from linear buckling analysis

In the present study, the amplitude of the perturbation is defined as the lateral change of the atom location relative to the product of the nanotube length and diameter (*L*D*). This is different from that used in (A. Sears, 2006) where the perturbation size is defined relative to the length of the nanotube only (0.5% in their report). Since the nanotube can be viewed as a hollow cylinder (especially those with small aspect ratio and large section ratio), it is more reasonable to measure the perturbation based on both the axial and radial dimensions. The strategy is in agreement with that adopted in MD simulations. As mentioned earlier, the size of noise-like random perturbation generated during the force balance in each step of a MD simulation depends on a

threshold net force (nearly zero). This threshold depends on the size of the problem or number of atoms in the system, which is usually proportional to *L*D*.

The critical strains obtained from different perturbation modes are listed in Table 4. Results corresponding to different perturbation amplitudes for each perturbation mode are also obtained. The two most frequently resulted postbuckling modes are “two-fin” and “three-fin” (Figure 4.7). In Table 4.1, it can be seen that the postbuckling mode shape may not resemble the initial perturbation mode. For example, the perturbation mode I (one-fin) and mode III (three-fin) can trigger postbuckling modes resembling the “three-fin” mode. Mode II (two-fin) and mode IV (four-fin) facilitate the development of the “two-fin” postbuckling mode. The lowest critical strain is found to result from “three-fin” linear buckling perturbation and leads to a “three-fin” postbuckling mode. Therefore, if the intrinsic critical strain is defined as one of the lowest predictions, the intrinsic postbuckling mode of the studied SWNT is a “three-fin” mode, even though the value varies with the imposed perturbation sizes. This conclusion agrees with Yakobson’s continuum mechanics analysis (B.I. Yakobson, 1996) where the lowest buckling strain is associated with the “three-fin” mode.

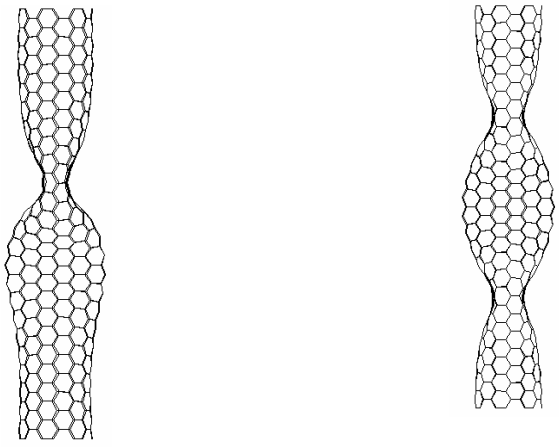

(a) Two-fin (b) Three-fin

Figure 4.7: Two typical postbuckling modes under axial compression

The critical buckling strain is found to increase monotonically with the decrease of perturbation size, no matter what kind of perturbation mode is chosen. No obvious convergence is observed for any mode even when the perturbation size decreases exponentially. Perturbations based on other linear buckling modes and combinations among them have also been attempted systematically. Only postbuckling modes of "two-fin" or "three-fin" are found, however they exhibited large critical strains.

Table 4.1: The effect of the perturbation by "two-step" perturbation for a 6nm long (7, 7) armchair SWNT

Perturbation mode	Amplitude (*L*D)	Critical strain (%)	Postbuckling mode
One-fin	$1*10^{-4}$	6.459	Three-fin
	$1*10^{-5}$	7.005	Three-fin
	$1*10^{-6}$	7.259	Three-fin
	$1*10^{-7}$	7.634	Three-fin
Two-fin	$5.4*10^{-4}$	6.507	Two-fin
	$5.4*10^{-5}$	7.421	Two-fin
	$5.4*10^{-6}$	7.746	Two-fin
	$5.4*10^{-7}$	8.125	Two-fin
Three-fin	$5.4*10^{-4}$	6.108	Three-fin
	$5.4*10^{-5}$	6.961	Three-fin
	$5.4*10^{-6}$	7.629	Three-fin
	$5.4*10^{-7}$	8.12	Three-fin
Four-fin	$5.4*10^{-4}$	6.177	Two-fin
	$5.4*10^{-5}$	7.228	Two-fin
	5.4*10-6	7.738	Two-fin
	$5.4*10^{-7}$	8.119	Two-fin

*** perturbation modes of the tube are shown in Figure 4.7*

A similar simulation is carried out for a 7nm long SWNT (10, 10). The first four linear buckling modes are shown in Figure 4.8. The effect of perturbation size and mode are given in Table 4.2. It can be seen from the table that the "two-fin" mode is the only post-buckling mode for the given (10, 10) nanotube (Figure 4.9) despite the difference of initial perturbation mode. However, the lowest buckling strain is initiated from the same perturbation mode ("two-fin").

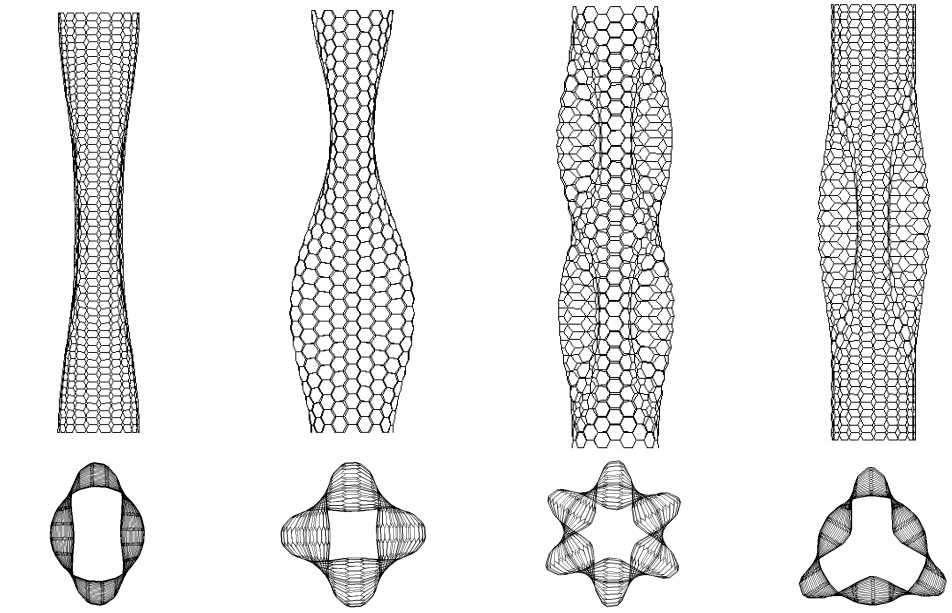

Figure 4.8: The first four linear buckling modes of a 7nm long (10, 10) SWNT

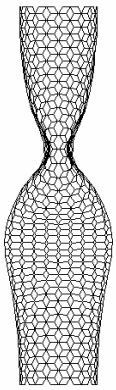

Figure 4.9: Postbuckling mode of a 7nm long (10, 10) SWNT (two-fin).

Table 4.2: The effect of the perturbation using "two-step" perturbation method for a 7nm long (10, 10) armchair SWNT

Perturbation mode	Amplitude (* L*D)	Critical strain (%)	Postbuckling mode
One-fin	$1*10^{-4}$	4.976	Two-fin
	$1*10^{-5}$	5.522	Two-fin
	$1*10^{-6}$	5.909	Two-fin
	$1*10^{-7}$	6.029	Two-fin
Two-fin	$1*10^{-4}$	4.273	Two-fin
	$1*10^{-5}$	5.29	Two-fin
	$1*10^{-6}$	5.409	Two-fin
	$1*10^{-7}$	5.709	Two-fin
Mode III	$1*10^{-4}$	6.134	Two-fin
	$1*10^{-5}$	6.559	Two-fin
	$1*10^{-6}$	6.659	Two-fin
	$1*10^{-7}$	6.309	Two-fin
Mode IV	$1*10^{-4}$	6.222	Two-fin
	$1*10^{-5}$	6.518	Two-fin
	$1*10^{-6}$	6.645	Two-fin
	$6*10^{-7}$	6.771	Two-fin

***perturbation modes of the tube are shown in Fig. 4.8*

(b) Sinusoidal perturbation

Perturbations of sinusoidal format were also considered in the present work. It is assumed that the radial coordinate *R* of each atom is a sinusoidal function of its circumferential and axial locations. Different wave numbers are then assigned, *N* in the circumferential direction and *M* in the axial direction. For an atom at location (*r, θ, z*), the perturbed coordinate (*R*) in polar coordinate system is expressed as $R = R_0 + A_0 \cos(M\theta)\sin(Nz\pi / L)$, where R_0 is the radius of the nanotube and A_0 is the perturbation amplitude. There is no perturbation in the tube axial direction (*Z).* Note that a similar strategy is often adopted in the classic shell theory of axial buckling analysis of the nanotube. The perturbation modes corresponding to different

M and *N* are plotted in Figure 4.10. The first two modes correspond to the first two linear buckling modes (two-fin and three-fin).

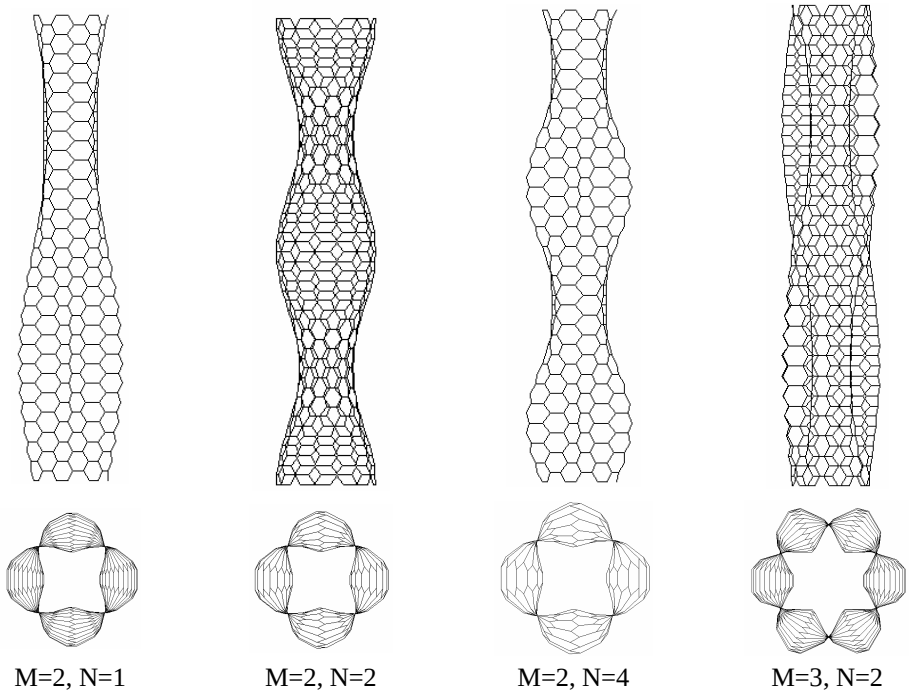

Figure 4.10: The sinusoidal perturbation modes.

For the 6nm long (7, 7) SWNT of 6nm long, the predictions of critical strain corresponding to different perturbation modes (different M and N) and amplitudes are listed in Table 4.3. It can be seen that the lowest critical strain corresponds to the "three-fin" postbuckling mode, which is in agreement with the conclusion reached using the "two-step" perturbation method.

The comparison of predictions using the "two-step method" and "the sinusoidal method" for a given perturbation size (10^{-5} *length) is given in Table 4.4. It can been seen that the predicted buckling strains for perturbations of same size and mode agree very well with each other even thought different perturbation methods are used.

Table 4.3: Critical strain based on sinusoidal perturbation of a 6nm long (7, 7) SWNT

Wave-numbers (M, N)	Perturbation size (*L*D) nm	Critical strain (%)	Postbuckling mode
(1, 1)	10^{-4}	5.759	Three-fin
	10^{-5}	6.078	Three-fin
	10^{-6}	6.56	Three-fin
(1, 2)	10^{-4}	8.108	Three-fin
	10^{-5}	8.81	Three-fin
	10^{-6}	9.16	Three-fin
(1, 3)	10^{-4}	8.01	Three-fin
	10^{-5}	8.61	Three-fin
	10^{-6}	9.03	Three-fin
(1, 4)	10^{-4}	5.909	Three-fin
	10^{-5}	6.115	Three-fin
	10^{-6}	6.61	Three-fin
(2, 1)	10^{-4}	7.259	Three-fin
	10^{-5}	7.76	Three-fin
	10^{-6}	8.029	Three-fin
(2, 2)	10^{-4}	6.72	Two-fin
	10^{-5}	7.209	Two-fin
	10^{-6}	7.709	Two-fin
(2, 3)	10^{-4}	6.36	Three-fin
	10^{-5}	7.	Three-fin
	10^{-6}	7.484	Three-fin
(2, 4)	10^{-4}	6.322	Two-fin
	10^{-5}	7.02	Two-fin
	10^{-6}	7.51	Two-fin
(2, 5)	10^{-4}	6.409	Three-fin
	10^{-5}	7.018	Three-fin
	10^{-6}	7.51	Three-fin

Table 4.4: Comparison between “two-step” perturbation results and sinusoidal perturbation results of a 6nm long (7, 7) SWNT

Perturbation mode	Amplitude (of length)	Critical strain		Postbuckling mode
		Two-step perturb.	Sin. perturb. (M=2, N=3)	
Three-fin	$1*10^{-4}$	6.108	6.097	Three-fin
	$1*10^{-5}$	6.961	7	Three-fin
	$1*10^{-6}$	7.629	7.618	Three-fin
	$1*10^{-7}$	8.12	8.078	Three-fin

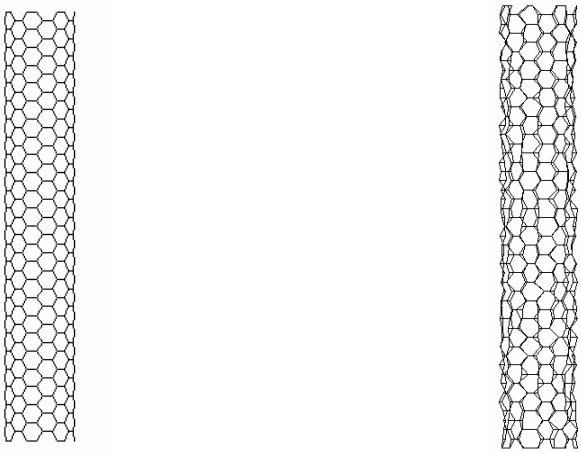

(a) without perturbation (b) with noise-like perturbation

Figure 4.11: (7 7) armchair nanotube with random perturbation in radial direction

(c) Noise-like perturbation

The noise-like random perturbation is discussed here where random geometric variations are imposed on the radial coordinates of each atom. The coordinate of each atom is expressed as, $R = R_0 + rand(0,1)A_0$, where the function $rand(0,1)$ yields a random value between 0 and 1. And A_0 is the amplitude of perturbation. Because of the random variation of the perturbation, the actual perturbation applied is often smaller than the limit A_0. Again the actual size of perturbation is measured based on the size of the nanotube (*L*D*). An example of nanotube shapes with random perturbation is illustrated in Figure 4.11. The effect of the amplitude on the critical strain using random perturbation is shown in Table 4.5. From Table 4.5, it can be seen that both the “three-fin” and the “two-fin” postbuckling modes can develop even with the same level of perturbation size. The critical strains associated with the “three-fin” mode are lower than those for the “two-fin” mode, which means the “three-fin” buckling is the intrinsic buckling mode for the SWNT under consideration. However, even for the same perturbation amplitude and same postbuckling mode, the predicted buckling strain varies randomly. Therefore, for noise-like perturbation, the simulation

has to be performed numerous times to insure that the lowest buckling strain is found. This may also explain the discrepancies between critical strain values obtained by MD simulations in the literature.

Table 4.5: Critical strains predicted by random noise-like perturbation for a 6nm long (7, 7) SWNT

Amplitude (*length)	Critical strain (%)	Postbuckling mode
$1.62*10^{-3}$	5.004	Three-fin
$1.7*10^{-3}$	5.759	Two-fin
$1.7*10^{-3}$	5.222	Two-fin
$0.88*10^{-4}$	7.028	Three-fin
$0.9*10^{-4}$	7.046	Two-fin
$0.9*10^{-4}$	7.6	Two-fin
$1.6*10^{-4}$	6.884	Three-fin
$1.7*10^{-4}$	7.071	Two-fin
$4.5*10^{-4}$	6.709	Three-fin
$4.6*10^{-4}$	6.609	Three-fin
1.6e-5	7.359	Two-fin
$1.6*10^{-5}$	7.306	Three-fin
$0.9*10^{-5}$	7.454	Three-fin
1.3e-6	7.809	Three-fin
$3*10^{-6}$	7.659	Three-fin
$5.5*10^{-6}$	7.61	Two-fin
$8*10^{-7}$	7.953	Three-fin
$1.65*10^{-7}$	8.209	Three-fin

Summary for the effect of perturbation

From the above discussion of perturbation methods, the following conclusions can be drawn:

(a) The “two-step method” and “sinusoidal method” yield similar prediction for the buckling strain for a given perturbation mode. The “sinusoidal method” is more convenient since the linear-buckling analysis is not needed.

(b) Random noise-like perturbation method can also predict the intrinsic postbuckling mode. However, numerous computations have to be performed to ensure that the

lowest value is obtained.

(c) If the intrinsic postbuckling strain is defined as the lowest strain among all predictions based on different perturbation modes but same level of amplitude, then the intrinsic postbuckling mode corresponds to it. Note that the intrinsic postbuckling mode is different for SWNTs with different configurations (dimensions and chiralities). For a 6nm long (7, 7) SWNT, the mode is "three-fin" while for a 7nm (10, 10) SWNT, it is "two-fin" pattern.

(d) The sensitivity of critical buckling strain on the perturbation mode and amplitude explains the discrepancies seen in the literature for critical strains. However, there is somewhat agreement between the present study, MD and MM simulations. For example, the critical strain for a 7nm long (10, 10) SWNT (when perturbation size is 10^{-5} (L*D)) agrees very well with the MD solution given by (Y. Zhang, 2006). The current prediction gives 5.29% for the "two-fin" postbuckling mode, and the MD simulation of (Y. Zhang, 2006) predicts 5.25%. Also for a 6nm long (7,7) SWNT, the current simulation predicts 6.6% for the "three-fin" mode, and the MD simulation of (B.I. Yakobson, 1996) gives 7.6%. More comparisons will be shown in the next section.

4.2.4 The effect of nanotube aspect ratio and section ratio

The effect of tube aspect ratio (L/d_{CNT}) on the buckling behavior of SWNTs under compression is discussed in this section. As mentioned in the literature review, for a long SWNT (large aspect ratio), the buckling strain is length dependent and the classical beam buckling theory can be used to explain this dependence ($\varepsilon_{cr}^{Euler} = \pi I_{CNT} / L^2$, where I_{CNT} stands for the effective bending stiffness of the SWNT). For a short SWNT (small aspect ratio), the buckling strain is length independent but is related to the section ratio (d_{CNT}/t) which can be explained by the classical thin-shell theory ($\varepsilon_{cr}^{shell} = 2t/d_{CNT}\sqrt{3(1-\nu^2)}$, where ν is the effective

Poisson's ratio of the tube (about 0.16)). Although neither the classical beam-buckling nor shell-buckling theories offer good predictions, they can explain the dependence buckling strain on the tube dimensions. More importantly, the buckling strain of a SWNT can be evaluated simply by these formulae by introducing some correction factors to fit the MD or other simulation results. However, for mixed buckling mode (combination of beam-buckling and shell-buckling modes, see Figure 4.2), one has to do simulations.

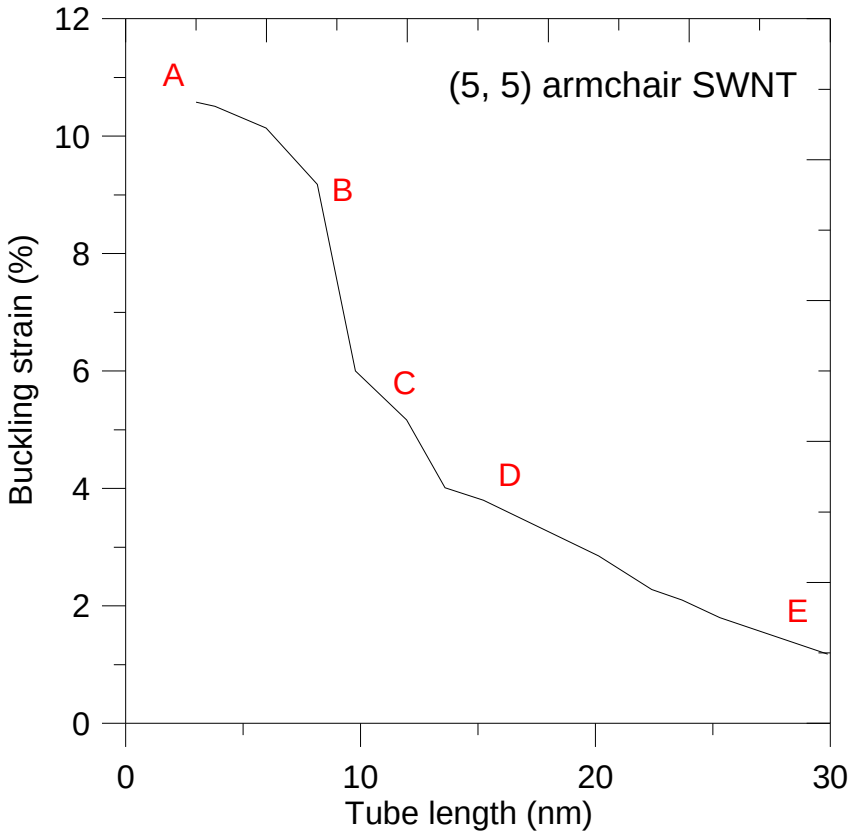

Figure 4.12: Critical strains for a (5, 5) SWNT for different lengths

To reveal the transition of buckling mode with respect to the aspect ratio, the buckling behavior of a (5, 5) armchair SWNT with different lengths is studied. The sinusoidal perturbation method is chosen with an amplitude of 10^{-4} (L*D) for all simulations. The buckling strain as a function of tube length is plotted in Figure 4.12. From the plot, it can be seen that the buckling strain curve displays four distinct segments (AB, BC, CD and DE) which corresponding to the four distinct buckling modes shown in

Figure 4.13. For short tubes with aspect ratios less than 5 (segment AB), the SWNT behaviors as thin-shell (Figure 4.13a) and the buckling strain is not very sensitive to the tube length and the aspect ratio. This is in agreement with the buckling behavior of a continuum thin-shell in principal. Two mixed modes can be generated for longer CNTs, beam-buckling combined with 3-kinks (Figure 4.13b) and 1-kink (Figure 4.13c) which correspond to the segments BC and CD in Figure 4.12. It seems that for CNTs within these aspect ratios the strain energy can be most efficiently released by both global sideway deflection and the local shell buckling. As the tube length becomes very long (segment DE), the nanotube will buckle sideway without local kinks (Figure 4.13d).

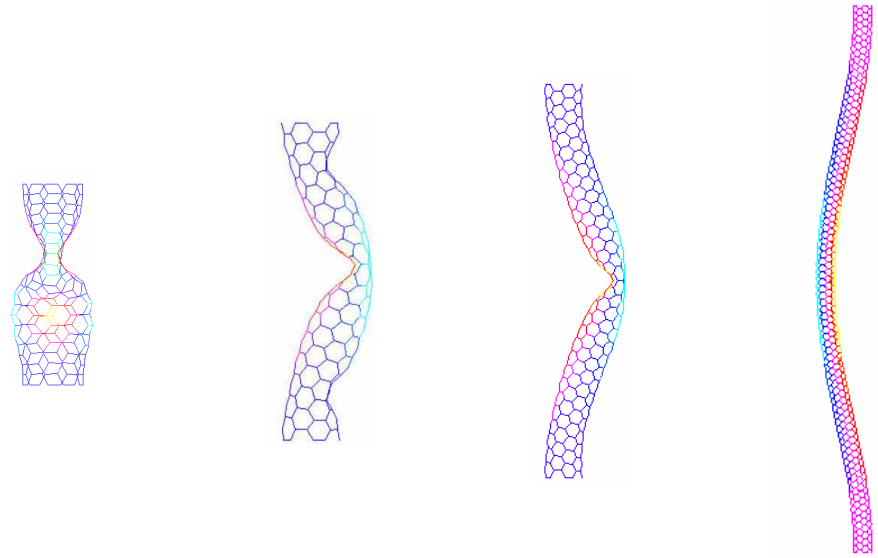

(a) Shell-buckling | (b) Mixed buckling (3-kink sideway) | (c) Mixed buckling (1-kink sideway) | (d) Column buckling (Euler buckling)

Figure 4.13: Postbuckling modes of a (5, 5) armchair nanotube for different tube lengths

To reveal the dependence of section ratio (d_{CNT}/t) on the buckling strain and mode, the compressive buckling behaviors of a series of armchair SWNTs have been simulated: (5, 5), (10, 10), (15, 15), (20, 20) and (25, 25). Also two different aspect

ratios (L/d_{CNT} is approximately 5, 25 respectively) have been considered to reveal the dependence for different buckling modes (beam, shell and mixed modes). The critical strain as a function of the diameter is plotted in Figure 4.14. As shown in the figure, the buckling strain is sensitive to the section ratio (d_{CNT}/t) for tubes with small aspect ratio. There exists a inversely linear relation between the buckling strain and the tube diameter which is in agreement with the continuum theory of shell-buckling. For long tubes (large aspect ratio), the buckling strain is insensitive to the tube diameter (or section ratio). This is because the buckling mode for these CNTs is beam-buckling. This is in agreement with the Euler-buckling theory of beams.

The transition of buckling behavior of the SWNT from shell-buckling to mixed-buckling and beam-buckling modes can be described by a mechanism map proposed by Cao (2006). Extensive simulations of the compressive buckling of armchair SWNTs with different lengths and diameters have been performed. The transition points of buckling modes for each tube are found out and marked in the map (Figure 4.15). The tubes have chiralities from (5, 5) to (35,35). The tube aspect ratio ranges from ~2 to ~100. The diameters of the tubes go from 0.678nm to 4.747nm. The thickness of all tubes is fixed at 0.34nm.

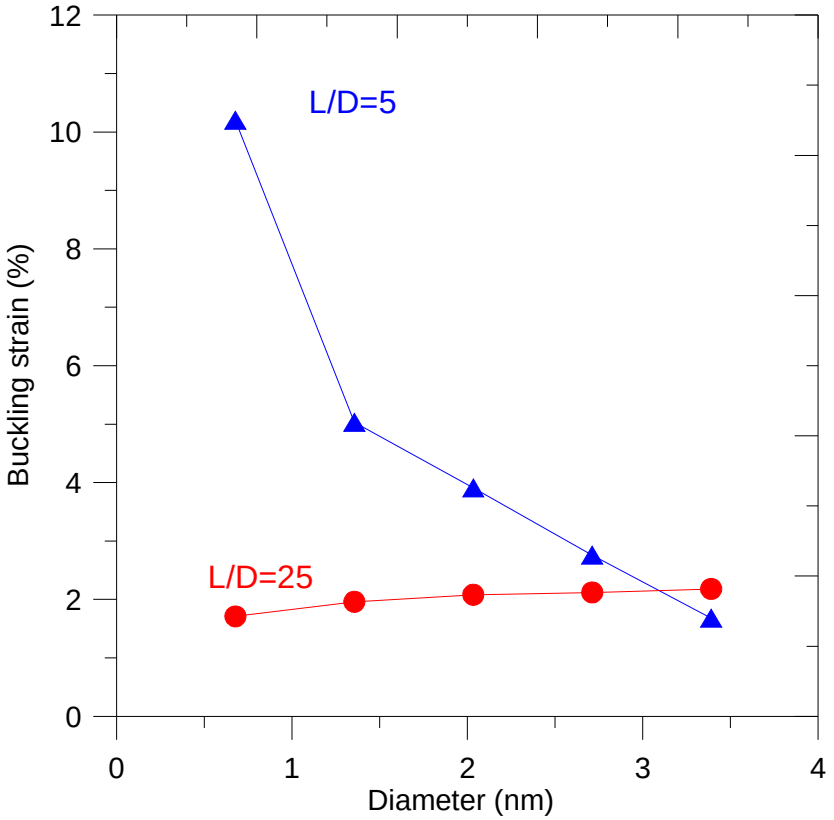

Figure 4.14:Critical strains vs tube diameter

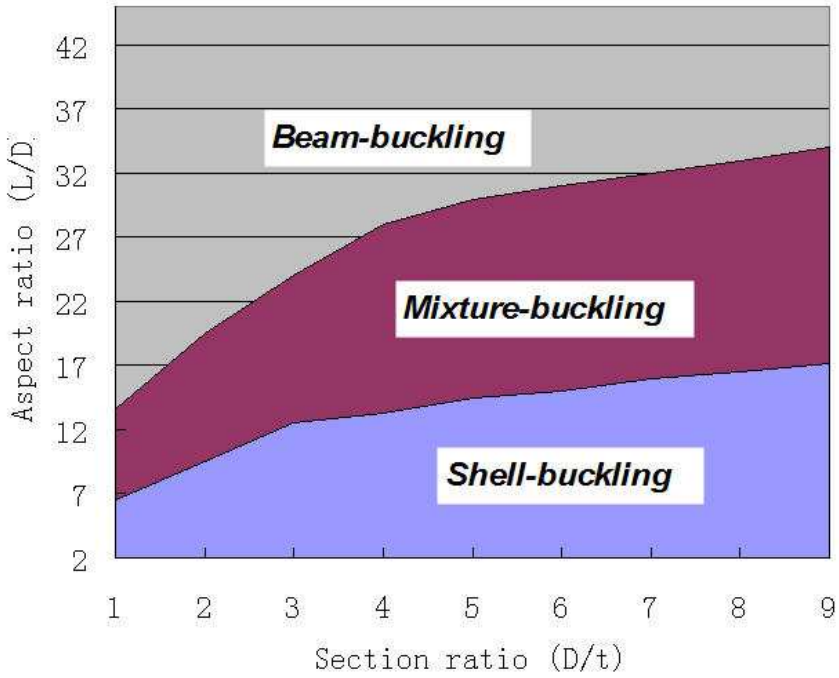

Figure 4.15: Mechanism map of buckling modes

4.2.5 The effect of chirality

The effect of chirality on the compressive buckling behavior of SWNTs is studied here. In most studies, the CNTs have symmetric chiral structures, armchair (n, n) and zigzag (n, 0). CNTs with other chiral angles have rarely been studied. By keeping the aspect ratio constant ($L/d_{CNT} \approx 5.2$), eight SWNTs with chiral angles varying from 0^o and 30^o were studied by MD simulations (Y. Zhang, 2006). The diameter of the SWNTs was about 1.3 nm. It was found out that the SWNTs displayed similar buckling modes except for the zigzag tube (17, 0) which has much higher buckling strain than others. Similar conclusion was drawn for long tubes ($L/d_{CNT} \approx 13.1$). In another report (G. Cao, 2007), five SWNTs with different chiral angles but similar dimensions were studied by molecular mechanics (MM). The diameters of the tubes were about 0.7 nm. Two different lengths (5nm and 19.2nm) of the tubes were considered. The results show that the buckling strain of the armchair SWNT is slightly higher than that of the zigzag SWNT. But the buckling strains of SWNTs with other chiral angles are much lower.

To resolve this discrepancy, two groups of SWNTs with different chiralities and aspect ratios are simulated. Three different lengths (aspect ratios) are considered to be able to address the different buckling modes (shell, beam and mixed modes). The results are shown in Figure 4.16. From the figure, it can be seen that the critical strains of SWNTs with symmetric structures (armchair and zigzag) are higher than others. This implies that symmetric structures are more efficient in resisting buckling. The buckling strains of armchair tubes are higher than those of zigzag tubes (about 10% higher). This conclusion is in contradiction with Y. Zhang's molecular simulation results but in agreement with G. Cao's molecular mechanics simulations. The conclusion is not affected by the buckling modes. However for long tubes which

behave like beams, the effect of the chirality is smaller compared to other buckling modes (shell-buckling and mixed-buckling).

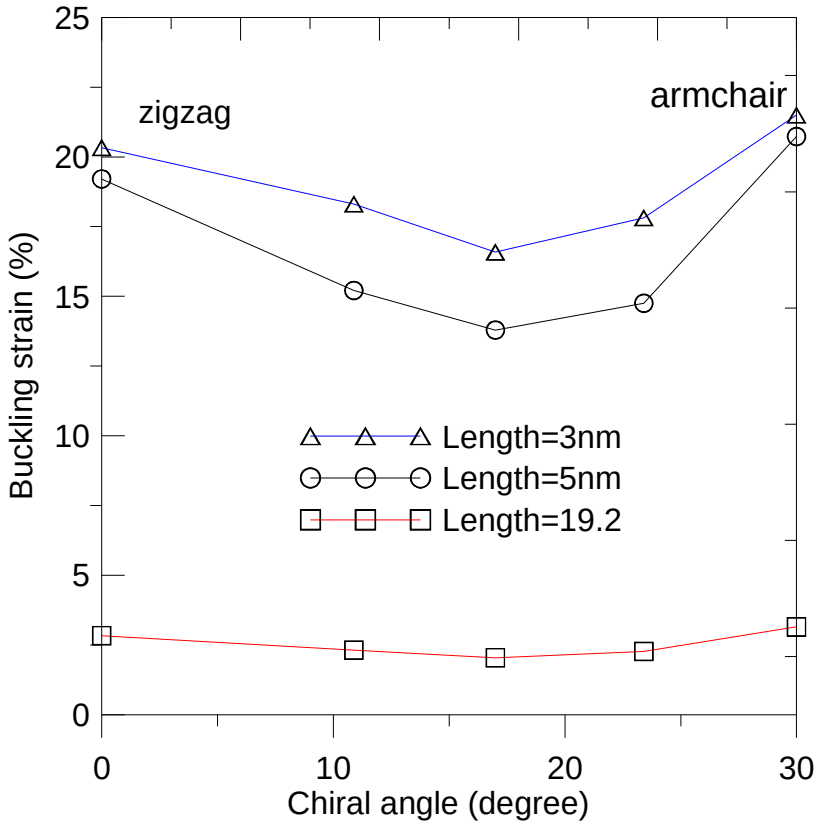

Figure 4.16: The effect of chirality on the buckling strain

4.3 Buckling of CNTs under Pure Bending

4.3.1 Literature review

For a SWNT under bending deformation, buckling (often referred to as wrinkling, kinking or rippling) can develop on the compressive side of the bend, leading to a significant reduction of the effective bending modulus of the tube. In practical applications (such as nano-valve or nano-transistor), bending buckling is much easier to realize and control compared with compression, although compressive buckling

seems more fundamental theoretically. In fact, bending (rather than tension or compression) is often used in experimental measurements of the mechanical properties of CNTs, to reduce the data to an effective elastic modulus of the nanotube. Although less studied than compressive buckling, both theoretical and numerical studies on the buckling behavior of SWNTs under bending have been undertaken to understand the phenomenon and complement the experiments. These studies can be divided into three main categories: (1) Atomistic simulations based on molecular dynamics (MD) (Iijima, 1996; Yakobson, 1996; Chang, 2006; Mylvaganam, 2006). (2) Continuum mechanics modeling (Yakobson, 1996; Arroyo and Belytschko, 2003; Pantano et al., 2003; Cao and Chen, 2006) where the CNTs are effectively modeled as thin shells with a fixed effective wall thickness, effective Young's modulus and Poisson's ratio (3) Analytical modeling based on molecular structural mechanics (C. Li, 2004; Chang, 2005).

To characterize the bending buckling of a SWNT, the critical curvature (κ_{cr}) is more often used than the critical bending angle (θ_{cr}). At the onset of buckling, the curvature is related to the bending angle of the tube axis by $\kappa_{cr} = \theta_{cr} / L$. Note that since κ_{cr} of a thin-shell tube is independent of the tube length according to thin-shell buckling theory ($\kappa_{cr} \propto t / d_{CNT}^{\,2}$), the use of κ_{cr} may eliminate the effect of the tube length in describing the bending buckling of the tube, although some researchers argue that κ_{cr} may be length dependent. The bending buckling behavior can be also characterized by the critical buckling strain (ε_{cr}^{bend}), which is related to the curvature by $\varepsilon_{cr}^{bend} = \kappa_{cr} d_{CNT} / 2$. The compressive buckling strain in a bending case can be assumed to be equal to the critical strain of compressive buckling, as was done by Yakobson, et. al. (1996). However, it was argued by Cao and Chen (2006) that the two critical strains are not comparable and the snap buckling behavior of a SWNT under bending can not be derived from axial compressive buckling. The effect of tube length and diameter on the bending buckling behavior has been investigated by some in the

literature, however, many of the findings are in contradiction with each other. For example, using MD simulation, Iijima et al. (1996) studied the bending buckling of SWNTs of different lengths and concluded that the critical bending buckling curvature is independent of tube length. And for a zigzag tube of 1.2nm in diameter, the critical bending angle was predicted to be around 30 degrees which agreed with the theoretical modeling work of Q. Wang *et al.* (2005) using continuum shell model. However, G. Cao et al. (2006) again using MD simulations argued that the buckling behavior is length-sensitive especially for relative shorter tubes. It was then argued that the tube length used in the work of Iijima et al. may be inside the length-insensitive region.

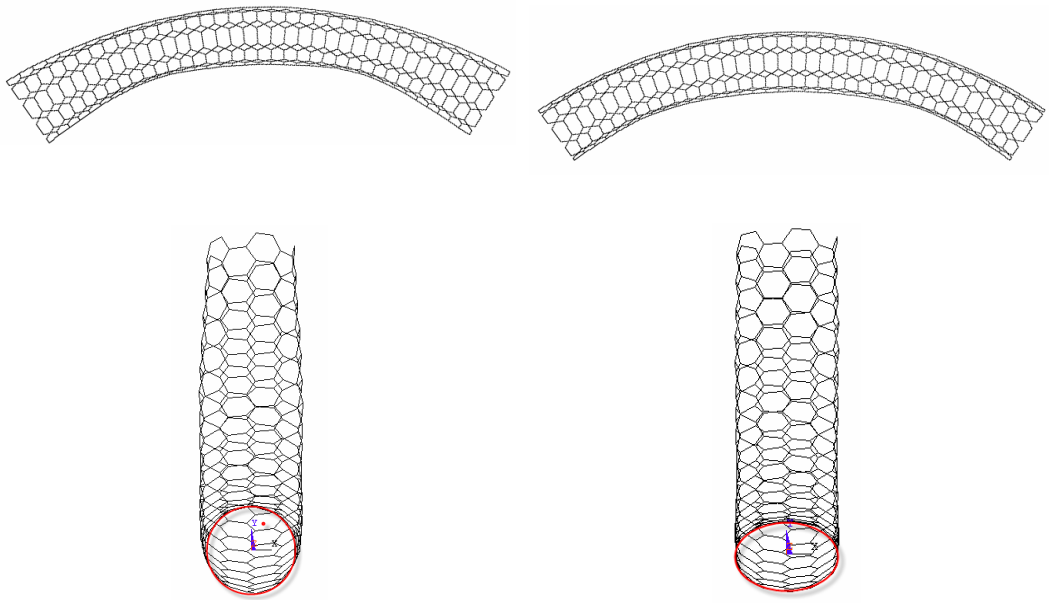

Figure 4.17: Traditional bending and pure bending cases

Moreover, during the simulation of the deformation of a SWNT segment, displacement boundary conditions are usually imposed on both ends to keep the original circular shape of the tube throughout the deformation. Such widely used boundary conditions (refer to “traditional bending” in the text) are different from the ideal pure bending case and difficult to realize in experiment. In fact, the cross section

of a SWNT tends to become oval due to the bending moment applied at the ends (Figure 4.17). For pure bending, the deformations of cross-sections along the tube axis should be uniform. It is practically difficulty to simulate the pure bending case for a thin-tube since the deformed shape of cross-section of a SWNT is not known. The influence of such boundary conditions at the tube ends on the CNT buckling behavior of CNTs is not yet clear.

It is the aim of the current work to study the buckling behavior of SWNTs under bending by the molecular structural approach outlined in Chapter 2. In this chapter, a systematic simulation is carried out to discuss the effect of SWNT chirality and boundary conditions on the buckling behavior. In addition, the influence of tube length and diameter are also considered.

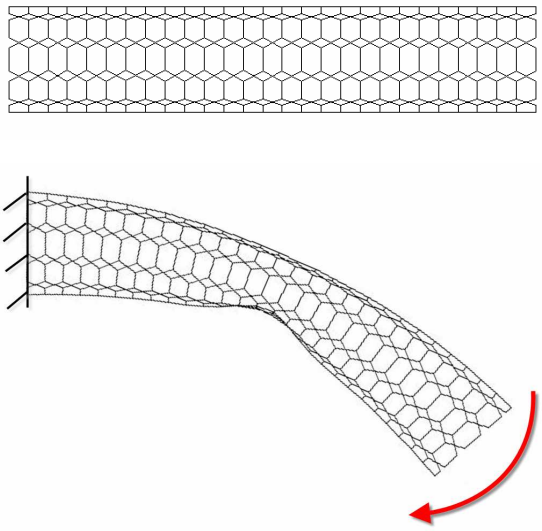

Figure 4.18: Bending buckling of a 3.3nm long (5, 5) armchair SWNT

4.3.2 Simulation method and procedure

The bending buckling behavior of SWNTs is studied numerically. For convenience and also to be able to compare our results with the results in literature, the “traditional bending” boundary conditions are used. As shown in Figure 4.18, the displacement

boundary conditions are applied on the atoms at the end rings in a way such that atoms at both ends remain circular and perpendicular to the deformed axis throughout the deformation. The length of the deformed tube axis remains unchanged and its curvature is essentially uniform during the solution. Atoms on the left end are fixed and those on the right end ring are rotated by a certain angle (θ) while their radial displacements are fixed to preserve the circular shape of the cross-section. During the simulation, the bending angle is increased by a small increment (~1 degree) to accurately simulate the large rotation problem.

In order to pinpoint κ_{cr}, the system's strain energy as a function of the bending angle (θ) is plotted in Figure 4.19 as obtained from the current simulation. It is observed that as θ increases initially the strain energy scales with θ^2. Once buckling is triggered, the strain energy decreases abruptly. The critical angle is then denoted by θ_{cr}, and the critical curvature is then obtained by $\kappa_{cr} = \theta_{cr} / L$.

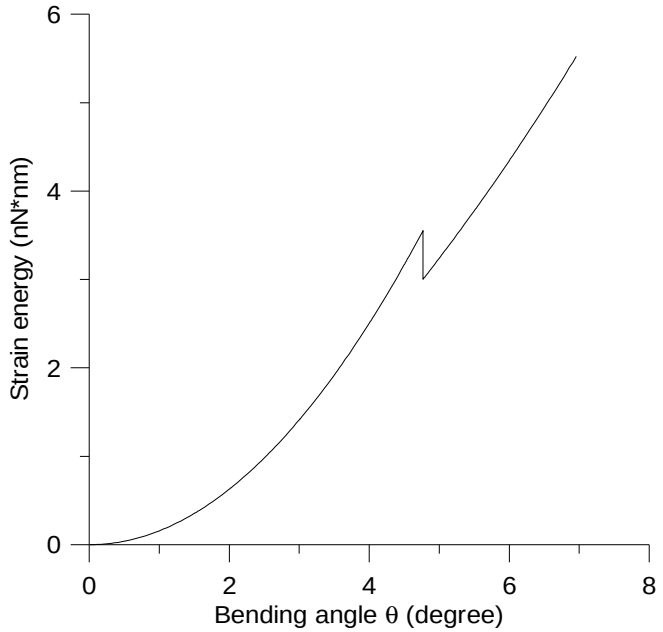

Figure 4.19: Strain energy of a (17, 0) zigzag SWNT subjected to bending

4.3.3 The effect of tube length

If a SWNT can be viewed as a thin-shell cylinder and the buckling behavior can be modeled by classical thin-shell buckling theory, then the critical curvature is length independent and expressed as,

$$\kappa_{cr} = \frac{4}{\sqrt{3(1-\nu^2)}} \frac{t}{{d_{CNT}}^2}$$

where, ν is the Poisson's ratio of the tube (about 0.16) and t is the effective thickness of the nanotube layer. A small effective thickness ($t = 0.066 \sim 0.089\text{nm}$) other than $t = 0.34\text{nm}$ has to be used in the above formula in order to fit the MD predictions. The length independence of κ_{cr} was affirmed by MD simulations (Iijima et al. 1996) of the bending of SWNTs with varying lengths, diameters and chiralities. However, the work by G. Cao (2006) suggests that the length/diameter aspect ratio of SWNTs affects the critical buckling behavior under bending. Their study of (9, 0) SWNTs with different lengths by MD simulations indicated that the variation of (κ_{cr}) is about 20% when L/d reduces from roughly 10 to 6. And for longer tubes, such dependence becomes very weak.

To solve this discrepancy, the bending buckling behavior of a series of SWNTs with different lengths are simulated here by the current model and approach. The SWNTs studied here are (5, 5) and (10, 10) with lengths ranging from 3nm to 25nm and aspect ratios ranging from about 3 to 20. The critical curvature versus the aspect ratio of SWNTs is plotted in Figure 4.20 a,b. From the plot, it can be seen that the bending buckling behavior is slightly dependent on the tube aspect ratio (or length) for short tubes. However for longer tubes, the critical buckling strain is insensitive to the tube length. This is in agreement with the conclusion of G. Cao, et. al (2006). Also noticed is that the length-dependence for (10, 10) SWNT is not as strong as that for (5, 5)

SWNT. This implies that for SWNTs with larger diameter, the buckling behavior is slightly length dependent. As for the buckling shape, it is observed from the simulation that for short tubes, there is one-kink in the middle of the tube, while there are two kinks near the ends for longer tubes (Figure 4.21). This is in agreement with other simulations (G. Cao, 2006; Iijima, 1996).

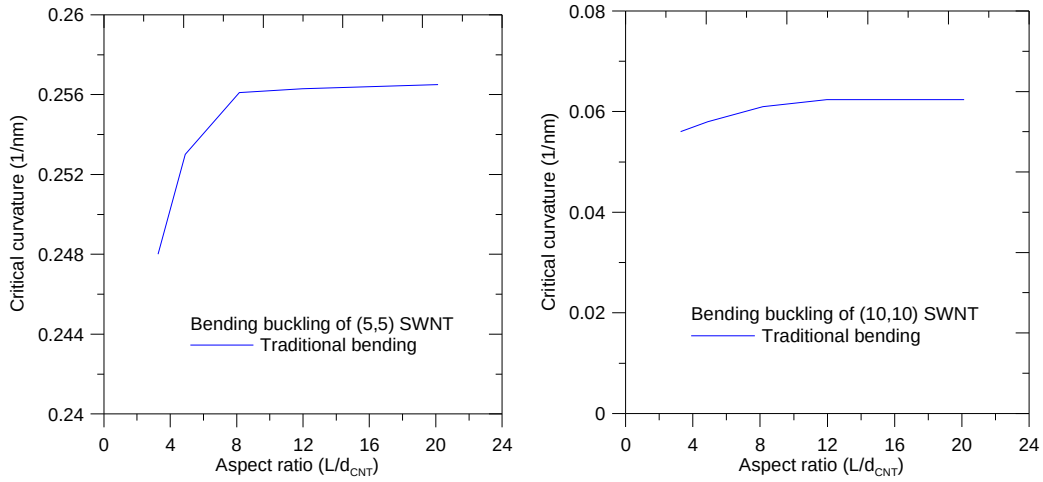

(a) SWNT (5, 5) (b) SWNT (10, 10)

Figure 4.20: Critical curvature of the SWNT under bending

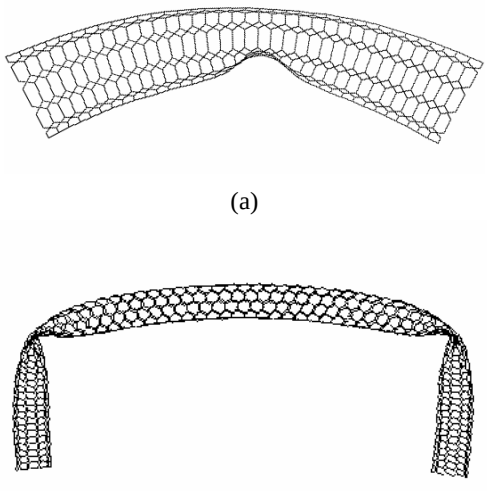

(a)

(b)

Figure 4.21: Kinks in the tube: (a) one kink; (b) two kinks

4.3.4 The effect of the boundary conditions

The length dependence described in the previous section may be related to the boundary conditions applied. Since the boundary conditions applied in the above simulations do not result in exactly “pure-bending”, the obtained results may not represent the true behavior of SWNTs under bending buckling. In order to study the effect of boundary conditions, the constraints at the tube ends are modified such that the whole SWNT deforms uniformly before buckling. It is practically difficult to simulate the pure bending case for a thin-tube since the deformed shape of the cross-section of a SWNT is not known. Nevertheless, the cross section shapes keep on changing during the bending deformation of the tube. In the current study, a multi-step procedure of updating the boundary conditions at the tube ends is developed. For each small load step, a small increment of the bending angle is applied. The shape of each end section is forced to resemble the shape of the middle section of the tube at the previous load step (Figure 4.22). If the load step is small enough, the deformation of the tube can be uniform during the procedure until buckling occurs.

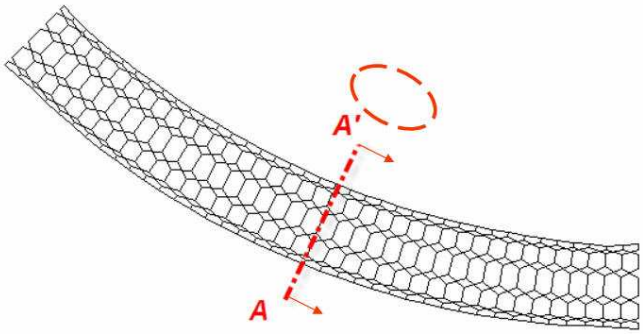

Figure 4.22: a (13, 0) zigzag SWNT subjected to pure bending

By comparing both types of boundary conditions (ie. traditional and pure bending), the effect of boundary conditions on the bending buckling behavior of SWNTs can be ascertained. Two groups of SWNTs: (5,5) and (10, 10) with different lengths (aspect

ratios) were studied. The critical curvature (κ_{cr}) is plotted versus the aspect ratio in Figure 4.23. The plot shows that the critical curvature is increased under "pure bending" which means that a SWNT under pure bending is more buckling resistive. This phenomenon is more significant for SWNTs with small diameter (SWNT (5,5) for example) than those with larger diameters (SWNT (10, 10) for example). For larger SWNTs such as (10, 10), the difference between predictions using different boundary conditions (traditional bending and pure bending) is smaller (about 3%) as seen in Figure 4.23 b. This suggests that only for long SWNTs with larger diameters, the traditional boundary condition can be approximately considered as pure bending.

As for the length dependence, the bending buckling upon pure bending load is less dependent on the tube length but still shows some length-dependent for short tubes. This size dependence of buckling behavior is different from the continuum thin-shell theory of buckling.

The effect of the boundary conditions is also embodied in the difference of buckling shapes. For all SWNTs with "pure bending" boundary conditions, only one-kink can be generated in the middle of the tube, in contrast to the two-kinks generated for long SWNTs using "traditional bending" boundary conditions (Figure 4.24 a b). Note that the two kinks in Figure 4.24a are close to the tube ends which indicates the effect of the incorrect boundary conditions applied in the "traditional bending" case.

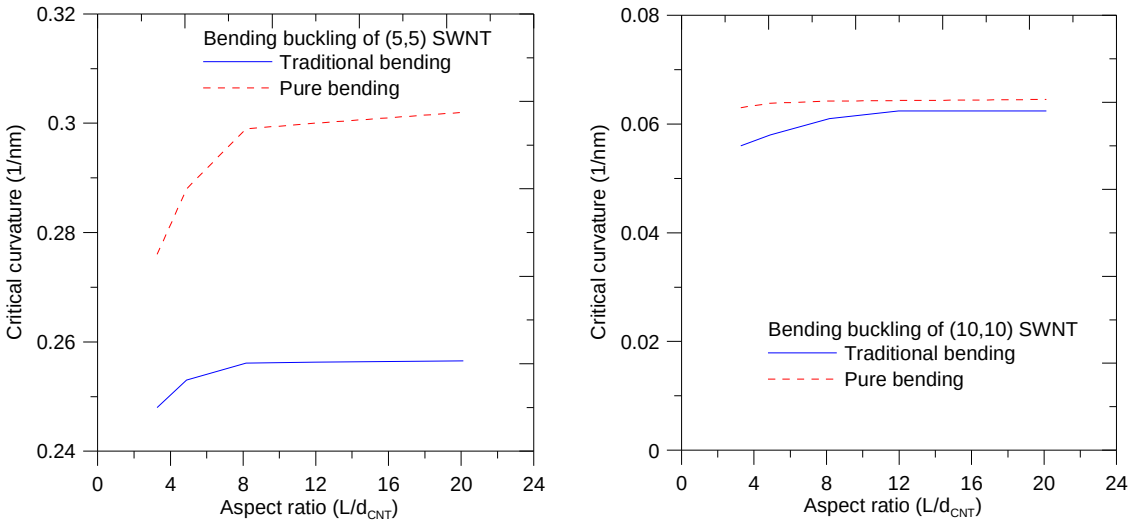

(a) (5,5) SWNT (b) (10, 10) SWNT

Figure 4.23: Influence of boundary conditions on the critical curvature of bending buckling

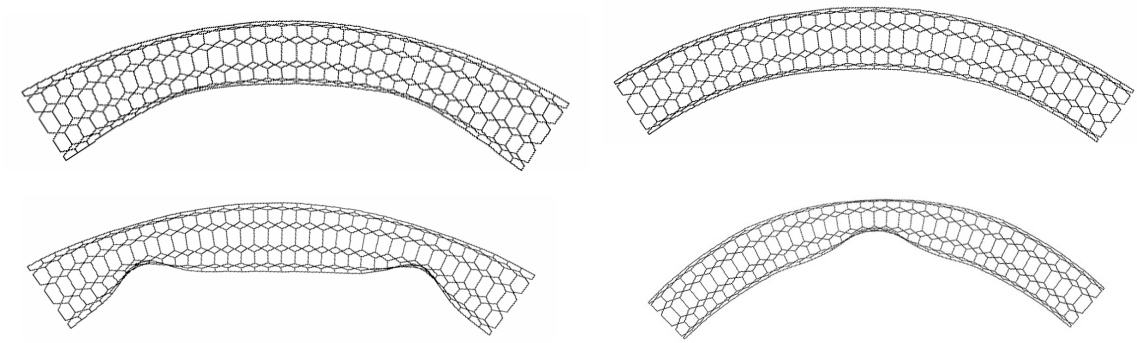

(a) Traditional bending (b) Pure bending

Figure 4.24: Effect of the boundary conditions on the bending buckling behavior

4.3.5 The effect of tube diameter

From the thin-shell buckling theory, the critical curvature is inversely proportional to the square of the tube diameter $(1/d_{CNT}{}^2)$,

$$\kappa_{cr} = \frac{4}{\sqrt{3(1-\nu^2)}} \frac{t}{d_{CNT}{}^2}.$$

Note that the thickness t in the above equation is an effect thickness of the SWNT,

which is usually in a range of (0.066nm~0.089nm) to fit the MD simulations in the literature. The dependence of $(1/d_{CNT}{}^2)$ has been confirmed by several MD simulations (Yakobson, 1996; Cao, 2006). However, the value of the critical curvature predicted by different simulations is different due to the different simulation approaches used. To study the relationship between the critical curvature of a SWNT and its diameter, various simulations have been carried out for SWNTs with different diameters. The critical curvature as a function of the nanotube diameter is plotted in Figure 4.25. Here, the effect of the tube length is eliminated by fixing the tube aspect ratio. For convenience, the traditional boundary conditions are applied in which the tube ends' radial displacements are fixed. Long tubes (aspect ratio about 12) are selected so that the effect of boundary conditions can be avoided and the results can be treated as the buckling behavior of SWNTs under pure bending. From the figure, it can be seen that the critical curvature decreases with increasing tube diameter. If fitted with a quadratic function of diameter, the critical curvature can be expressed as,

$$\kappa_{cr} = 0.115/d_{CNT}{}^2$$

Therefore, the critical curvature of the bending buckling is proportional to $(1/d_{CNT}{}^2)$. It is also noticed that for SWNTs with small diameters, the fitting is relatively inaccurate.

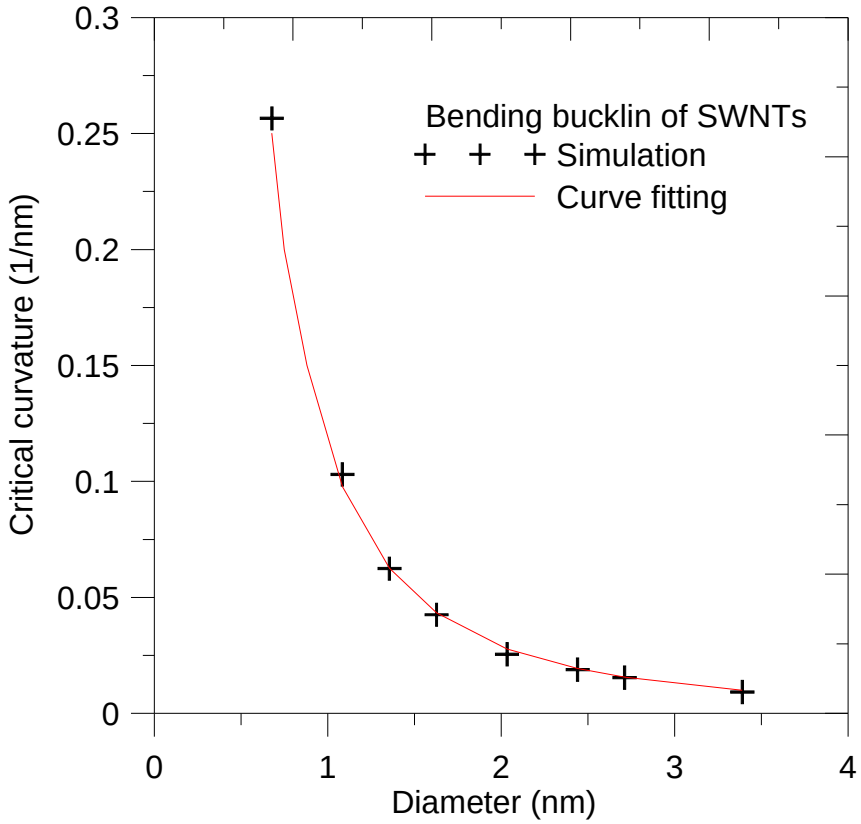

Figure 4.25: Dependence of critical curvature on the tube diameter

4.4 Compressive Buckling of Multi-Walled Carbon Nanotubes (MWNTs)

4.4.1 Literature review

Compared to those of SWNTs, there are fewer theoretical studies dealing with the buckling of multi-walled carbon nanotubes (MWNTs). The earliest investigation is a MD simulation by Iijima (1996) in which the buckling of a double-walled carbon nanotube (DWNT) subjected to bending deformation was studied. The MD simulation of MWNTs with 4 layers was performed by Srivatava (1997) where the axial compressive buckling was predicted. MD simulations of MWNTs with 3 and 4 layers under compressive buckling have been reported by K. Liew (2004) where the compressive buckling of the tube with aspect ratio less than 3 was studied. Recently, MD simulations of MWNTs with up to 7 layers subjected to bending were reported (T.

Chang, 2006). Molecular mechanics (MM) simulation has been performed for the compressive buckling of MWNTs with up to 3 layers (A. Sears, 2006). The computational cost of the buckling behavior of a MWNT scales up with the number of graphite layers in a MWNT, mainly due to the difficulty in evaluating the interlayer potentials (van der Waals potentials). The covalent bond potential has a shorter cut-off length. In contrast, evaluating the interlayer potential for one atom in a layer with the use of pairwise potentials can result in including the interactions with many neighboring atoms.

There are also a few continuum mechanics simulations of the buckling behavior of MWNTs. Finite element simulations with MWNTs constructed by thin-shell elements were performed to study the bending buckling behavior of MWNT of up to 14 layers (Panato, 2004). The thin-shell element used in the analysis has an effective thickness of 0.075nm to address the bending stiffness of the graphite layer in the CNT. The interlayer interaction was simulated by interaction elements with a self-defined constitutive relationship. Finite element analysis of MWNTs under four-point bending was studied by X. Wang (2004) in which the MWNT was treated as a solid medium with special material properties. It must be noted that these simulations neglected the lattice structure and chiralities of the CNTs

Analytical continuum models have also been developed, such as multi-shell and multi-beam (or multi-column) models. A multiple-column model based on continuum theory of beam buckling was used to study the axial buckling behavior of DWNTs (C. Ru, 2000). His approach was extended to MWNTs with more layers by his coworkers (C. Wang, 2004). Arroyo and Belytschko (2003) developed a generalized local quasicontinuum method which enables both interlayer vdW interactions and interlayer bonded potentials to be incorporated into the calculations. Continuum thin-shell models (multi-shell) have also been used in the work of X. He (2005). Although these models can predict the buckling behavior of MWNTs with many layers, the validity of the results should be confirmed by atomistic simulations. A few other continuum mechanics approaches based on molecular mechanics have been

used to study the buckling behavior of MWNTs. An analytical model based on molecular mechanics was developed by T. Chang (2006) to study the compressive and bending buckling behavior of MWNTs. However, the length effect can not be addressed by their model since only small segment of a MWNT is considered. Finite element simulation of compression buckling has been performed for DWNTs by C. Li (2004) using their molecular structural model of the CNT. The van der Waals forces between the graphite layers are simulated by truss rods with non-linear material properties. However, as stated in Chapter 2, the bending stiffness of the graphite layer in a CNT can not be correctly represented in C. Li's model.

From the above review, it can be seen that for numerical simulations considering both the lattice structure and tube length of a MWNT, the maximum number of layers being studied is 7. Nevertheless, the length of these MWNTs is very short. For example, in the MD simulations of K. Liew (2004), the tube aspect ratio is less than 3, and in T. Chang's MD simulation of bending buckling, the aspect ratio is even smaller (about 2.5). Obviously, this is not enough to reveal the buckling behavior of long MWNTs with more layers.

Therefore, it is the objective of the current study to develop a more efficient method by implementing the "modified beam model" we developed and incorporate it in the finite element analysis (ABAQUS). The van der Waals interaction is simulated with the approach presented in Section 3.3. Both compressive and bending buckling behaviors of MWNTs are simulated.

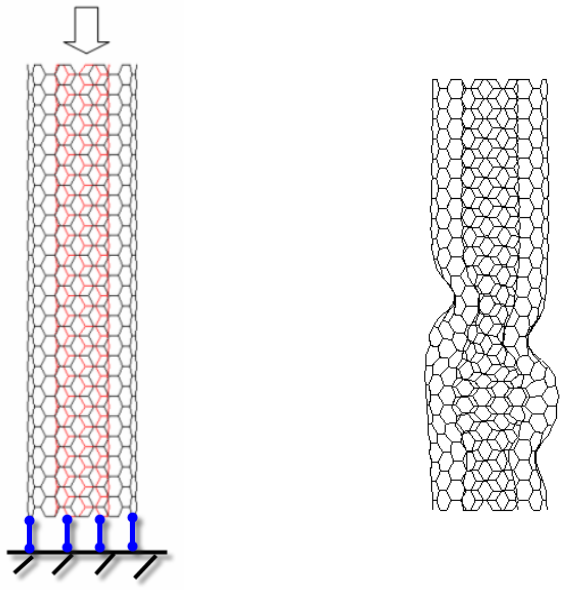

(a) Before buckling (b) At buckling

Figure 4.26: Axial compressive buckling of a DWNT: (5, 5)@(10, 10)

4.4.2 Simulation method and procedure

The MWNTs are constructed of beam elements with sectional properties derived in Chapter 2. The van der Waals interaction between the neighboring graphite layers is simulated by non-linear spring elements (SPRINGA in ABAQUS). The nonlinear $f-L$ (force vs distance) relationship is established by the user defined material subroutine (UMAT).

The boundary condition of the axial compression model is shown in Figure 4.26. The axial displacement of one end of the tube is fixed. An axial compression is applied at the other end. The radial displacements of both ends are freed in order to simulate simply supported buckling. The axial compression is gradually applied to ensure the equilibrium iteration of the nonlinear reaction of the van der Waals force.

Since the interlayer deformations may cause sliding between different graphite layers in a MWNT, the effective distance of van der Waals force is set up to be very long. A

cutoff length (0.68 nm) is chosen in all simulations.

4.4.3 Compressive buckling of double-walled carbon nanotubes (DWNTs)

In this section, the buckling behaviors of DWNTs under compression is simulated. A series of DWNTs with armchair chiralities are chosen with the outer diameter ranging from 1.356nm to 4.747nm. The index difference between the neighboring layers is five. In total, six types of DWNTs were studied: (5,5)@(10,10), (10,10)@(15,15), (15,15)@(20,20), (20,20)@(25,25), (25,25)@(30,30), and (30,30)@(35,35). The aspect ratio of each DWNT is fixed to about 4. The sinusoidal perturbation is applied for all tubes with fixed amplitude of 0.01% even though the buckling stain of DWNTs is less sensitive than that of SWNTs. The critical buckling strain as a function of the outer diameter is plotted in Figure 4.27. The results for SWNTs are also included to enable comparison with MWNTs.

From the figure, it is seen that the critical strain of a DWNT under compression decreases as the out diameter increases. The critical strain of DWNTs is between the values obtained for its SWNT constituents. In other words, less than that for the inner tube but larger than that for the outer tube. In the other word, the buckling resistance of the outer tube can be enhanced by the inner tube.

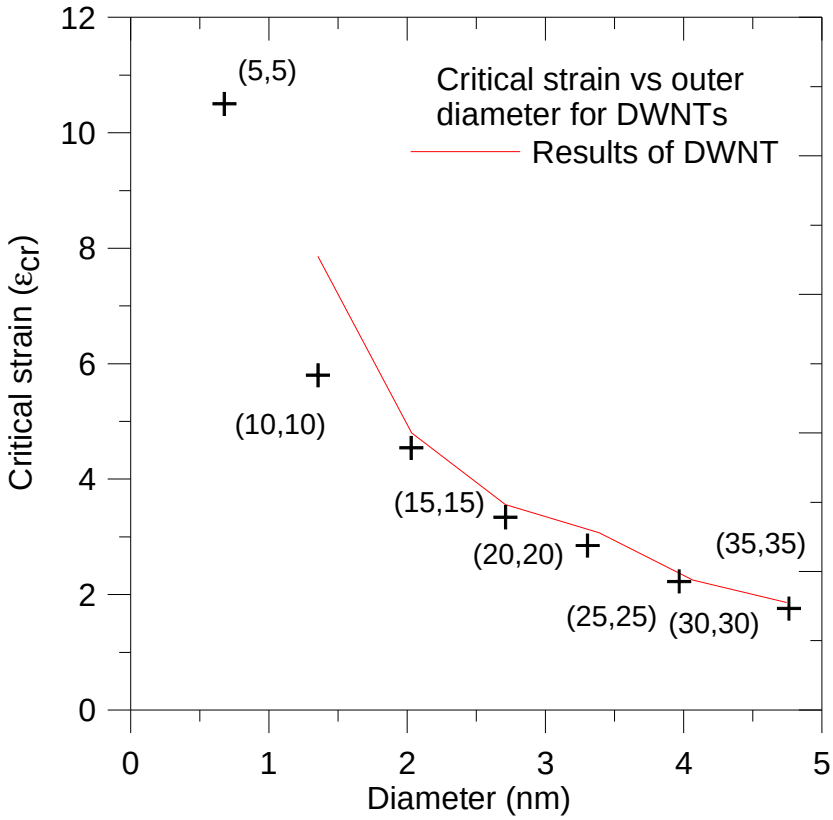

Figure 4.27: Critical strain vs outer diameter for DWNTs under compression

The buckling mode of DWNTs seems to be controlled by the buckling mode of the inner tube. When the DWNT is short (small aspect ratio), the buckling mode is shell-buckling (Figure 4.28a). For longer DWNTs, the buckling mode is mixed mode (Figure 4.28b). Note that for the latter (aspect ratio about 5) the buckling mode of the individual SWNT (5, 5) is mixed mode but for SWNT (10, 10) it is shell-buckling. In another case ((30, 30)@(35, 35)) studied, the buckling mode is shell-mode which agrees with the buckling mode of the inner tube (30, 30) (Figure 4.28c). For all DWNTs simulated, the spacing between the inner tube and outer tube remains approximately 0.34nm (Figure 4.28 a, b), which agree with the experimental observation of buckled MWNTs.

To study the effect of the van der Waals forces between the layers, simulation is also

performed for a DWNT (5,5)@(10,10) in the absence of vdw interactions. The plot (Figure 4.29) shows that the two graphite layers behave differently. The outer tube buckled at a smaller compressive strain than that of the inner tube. Because of the absence of vdw forces, the buckling is not transferred to the inner tube, leaving the inner tube intact.

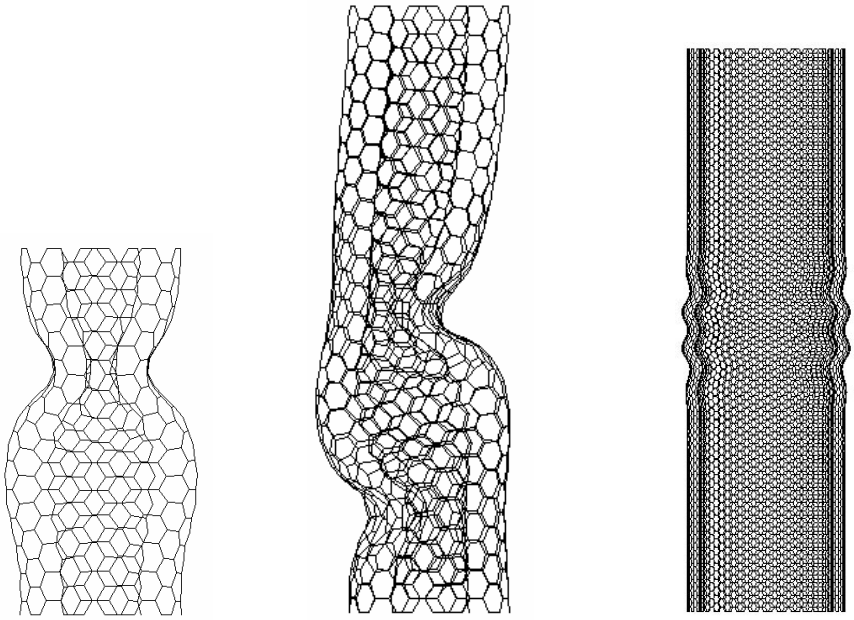

(a) short DWNT, (5,5)@(10,10); (b) long DWNT (5,5)@(10,10); (c) DWNT (30, 30)@(35,35)

Figure 4.28: Buckling modes of DWNTs

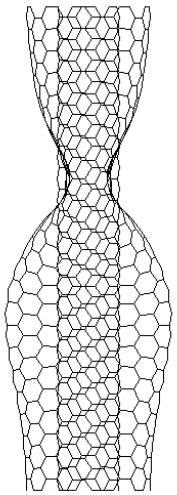

Figure 4.29:The buckling of DWNT (5,5)@(10,10) in the absence of van der Waals forces

4.4.4 Compressive buckling of Muti-walled carbon nanotubes

In this section, the compressive buckling behavior of MWNTs with more than two graphite layers is simulated. First, two examples of three-walled carbon nanotubes (TWNTs), (5, 5)@(10, 10)@(15, 15) and (25, 25)@(30, 30)@(35, 35) are simulated to reveal the effect of thickness on the buckling behavior. Then a series of MWNTs with the outer tube as (35,35) are studied.

Compressive buckling of TWNTs

The TWNT nanotubes are:

TWNT #1: (5,5)@(10,10)@(15,15) and

TWNT#2: (25,25)@(30,30)@(35,35) .

The buckling modes are shown in Figure 4.30 a-c and Figure 4.31 a-c. Compared with TWNT #2, TWNT #1 has a small section ratio (d_{CNT}/t) which makes the buckling mode different from that of TWNT#2. From Figure 4.30, it is seen that the outmost tube (15, 15) of the TWNT#1 buckles first under compressive deformation (initial buckling strain ε is about 5.5%), while the inner two tubes (5, 5) and (10, 10) are almost intact at the onset of buckling (Figure 4.30b). Upon further compression to $\varepsilon = 6.2\%$, all three layers buckle. For the second TWNT (TWNT#2), the bending behavior is different from that of TWNT#1. As shown in Figure 4.31 b c, at a critical strain $\varepsilon = 2.4\%$, buckling is initiated in all three layers of the TWNT. Further deformation only enhances the buckling waves (Figure 4.31c). If the buckling behavior of TWNT #1 can be called as “part-forward” mode, the behavior of the TWNT #2 is called “all-together” mode. Therefore, the thickness (or section ratio d_{CNT}/t) of MWNTs plays an important role in determining their buckling mode.

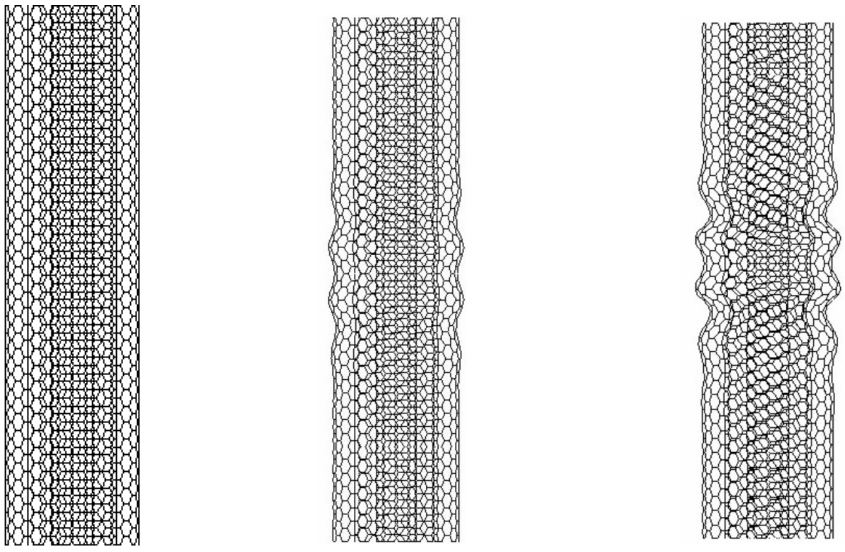

(a) Original (b) initial buckling $\varepsilon_{cr} = 3.4\%$ (c) Full buckling $\varepsilon_{cr} = 3.9\%$

Figure 4.30: Compressive buckling of a TWNT: (5,5)@(10,10)@(15,15)

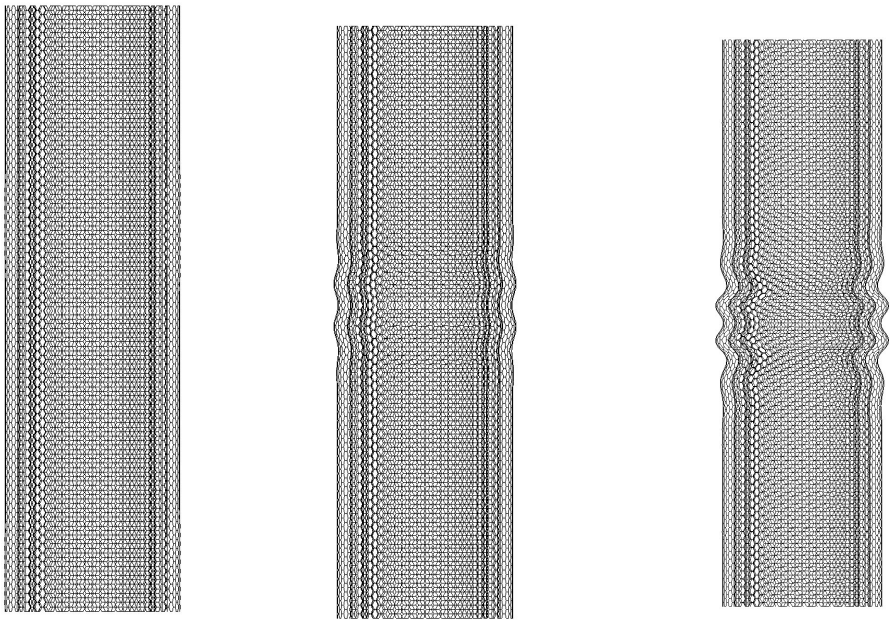

(a) Original (b) initial buckling $\varepsilon_{cr} = 2.8\%$ (c) Full buckling $\varepsilon_{cr} = 3.1\%$

Figure 4.31: Compressive buckling of a TWNT: (25,25)@(30,30)@(35,35)

Compressive buckling of MWNTs with more than three layers

A similar phenomenon is also observed for MWNTW with more than three layers. In this section, a series of MWNTs $(5n,5n)_{n=3,4..7}$ with the same outer tube (35, 35) are studied. The aspect ratio of each MWNT is set to be about 4. The initial buckling strain as a function of the number of layers is plotted in Figure 4.32. From the figure, it can be seen that the initial critical strain of MWNTs increases significantly from SWNT to DWNT. For MWNTs with more than three layers, the initial critical strain shows hardly any increase which indicates that only several outmost layers buckle initially.

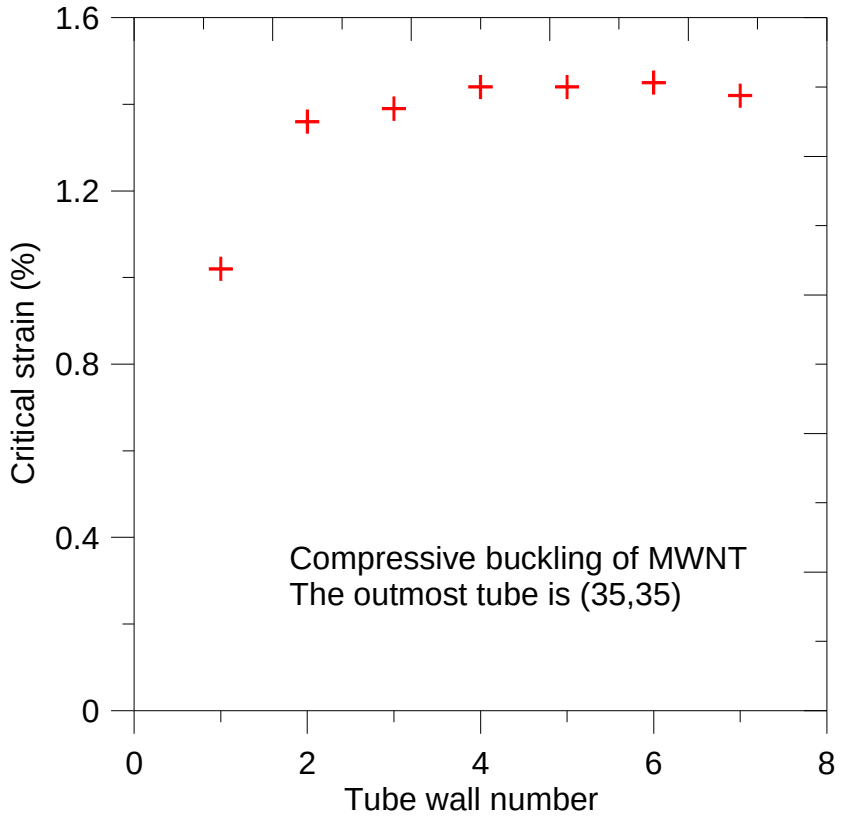

Figure 4.32: The buckling strain vs the number of layers in a MWNT

The phenomenon can also be observed from the different initial buckling modes. All-together and part-forward modes, for thin and thick tubes are shown in Figure

4.33 a and b. All individual tubes buckle simultaneously (all-together mode) in a thin MWCNT (3 layers for example) once the compressive strain reaches a critical buckling value. However, in a thick MWCNT (7 layers for example), only the outmost layers buckle. Further increase of the compressive strain can finally induce more inner tubes to buckle.

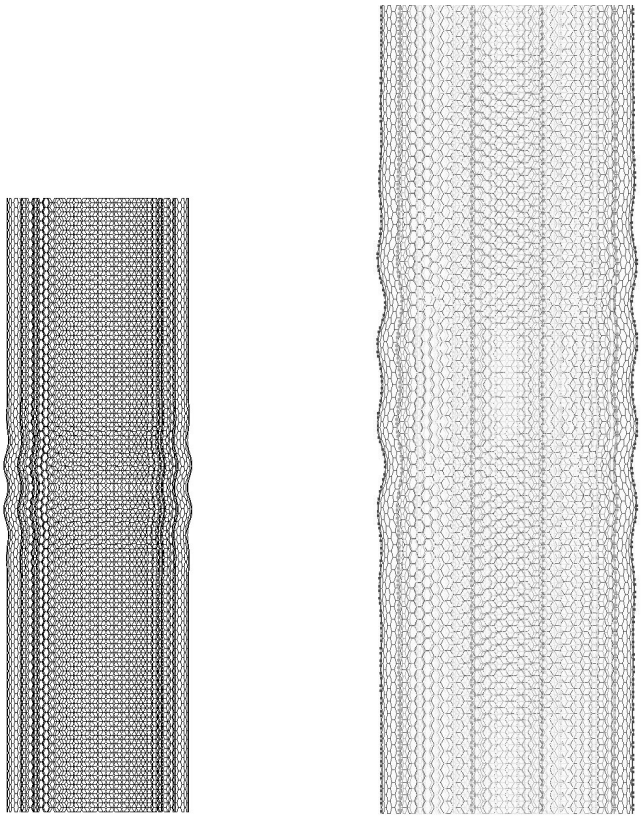

(a) Three-walled CNT; (b) Seven-walled CNT

Figure 4.33: Rippling of three and seven walled carbon nanotube under compression.

4.5 Bending Buckling of Multi-Walled Carbon Nanotubes

4.5.1 Simulation method and procedure

The buckling of MWNTs under bending is simulated similar to that of compression. Displacement boundary conditions are applied at one end of the MWNT such that the atoms at this end rotate as a whole by θ (Figure 4.34). The other end of the MWNT is fixed. The initial increment of the applied bending angle is set to be 1 degree. Automatic increment algorithm is chosen by the program itself. The onset of buckling can be observed both from the strain energy curve and the deformed shape.

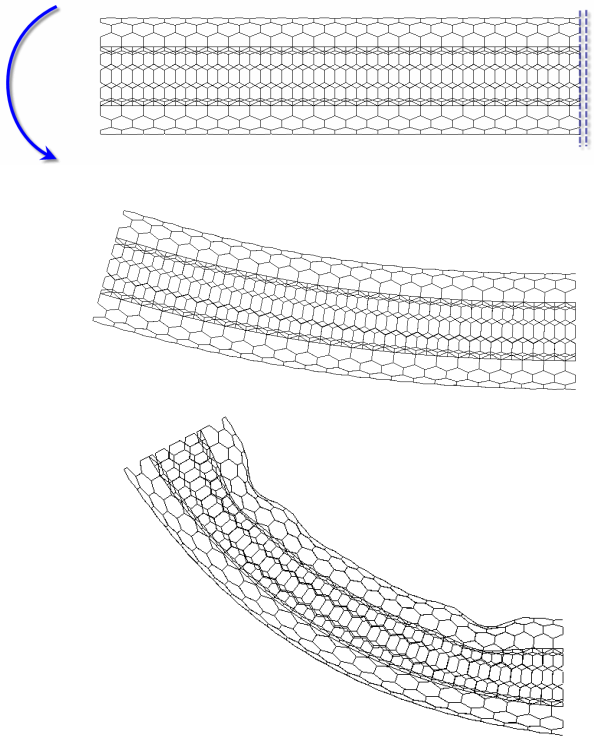

Figure 4.34: Bending of a DWNT (5,5)@(10,10)

4.5.2 Bending buckling of double-walled carbon nanotubes

The buckling of a double-walled nanotube (DWNT) under bending is studied here. A series of DWNTs with different diameters are considered: (5,5)@(10,10), (10,10)@(15,15), (15,15)@(20,20), (20,20)2(25,25), (25,25)@(30,30) and (30,30)@(35,35). The outer diameters range from 1.36nm to 4.75nm. The aspect ratio of all tubes is fixed to about 4. Two different buckling modes are observed for DWNTs with different section ratio (D/t). For example, the bending buckling modes of (5,5)@(10,10) and (30,30)@(35,35) are shown in Figure 4.35, 4.36.

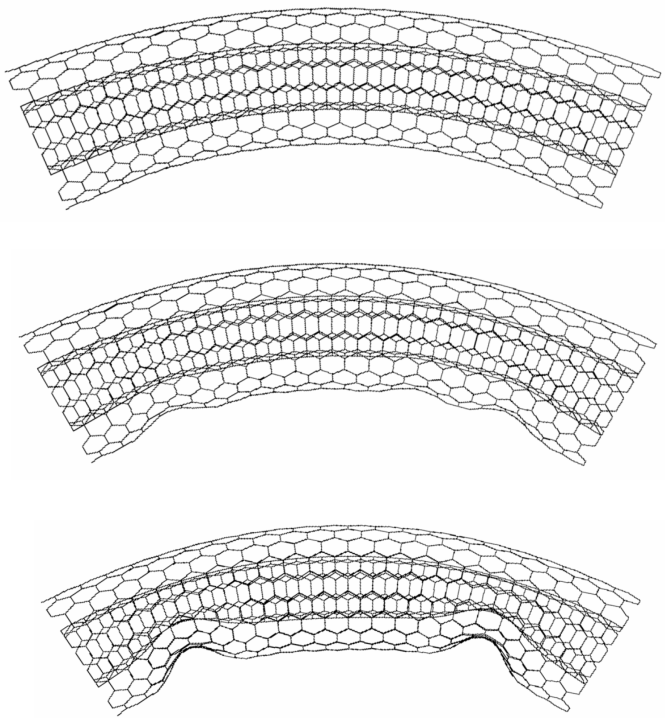

Figure 4.35: The bending buckling of a DWNT (5,5)@(10,10), aspect ratio=4.

As can be clearly seen in Figure 4.35b, the outer tube in the (5,5)@(10,10) DWNT buckles first, whereas the inner tube remains intact. This is because the critical curvature of SWNT decreases with the tube diameter ($\propto 1/d_{CNT}$). Further increase in global curvature can finally drive the inner tube into buckling (Figure 4.35c). This phenomenon of buckling transferring is called “part-forward model” in T. Chang and

J. Hou's report (2006). For the (30, 30)@(35,35) DWNT, a different buckling mode is found from the simulation. As seen in Figure 4.36b, both the inner tube and the outer tube buckle simultaneously (so calledthe "all-together mode"). The mode difference in buckling of the DWNTs indicates that the section ratio (d_{CNT}/t) of is critical. For larger section ratios, the tubes in a MWNT can buckle together, whereas the tubes buckle part-forwardly for small section ratios. The same phenomenon is found for MWNTs with more layers, as shown later.

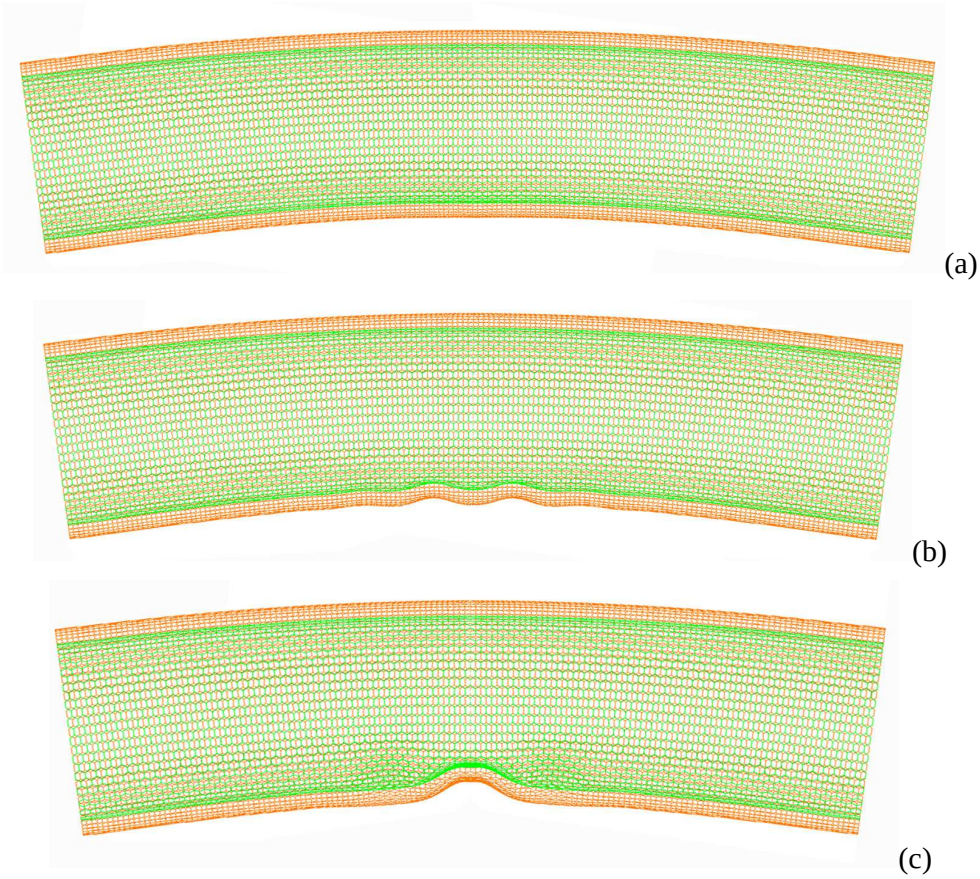

Figure 4.36: The bending buckling of a DWNT (30, 30)@(35,35), aspect ratio=4

The effect of van der Waals forced on the bending buckling of the DWNT is also studied. For the DWNT (5,5)@(10,10), if the interlayer van der Waals interactions are neglected, the buckling mode shows that the inner tube remains intact throughout

the bending deformation (Figure 4.37). Also, note that when the van der Waals forces are considered in the DWNT (5,5)@(10,10), the outer tube buckles first and the interlayer space decreases around the buckling site. Since the magnitude of the van der Waals force is small initially, the inner tube (5,5) can withstand it. With the decrease of interlayer space, the inner tube also buckles.

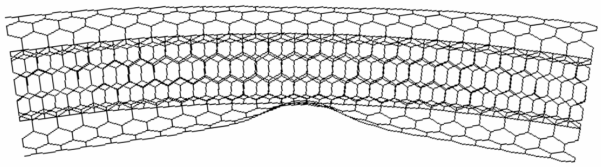

Figure 4.37: The bending buckling of a DWNT with the absence of van der Waals force

4.5.3 Bending buckling of MWNTs with more than three layers

In this section, the bending buckling of MWNTs with more than three layers is simulated. To study the effect of wall number on the bending buckling behavior, a series of MWNTs with the same outer diameter are considered. For convenience, the outmost tube of each MWNT is (35,35). The variation of critical bending curvature (κ_{cr}) versus the wall number is plotted in Figure 4.38. The figure shows that κ_{cr} of MWNTs is much higher than that of a SWNT with the same outer diameter. From DWNT to three-walled nanotube, κ_{cr} increases slightly. While for MWNT with more than three layers, no apparent change of κ_{cr} is found.

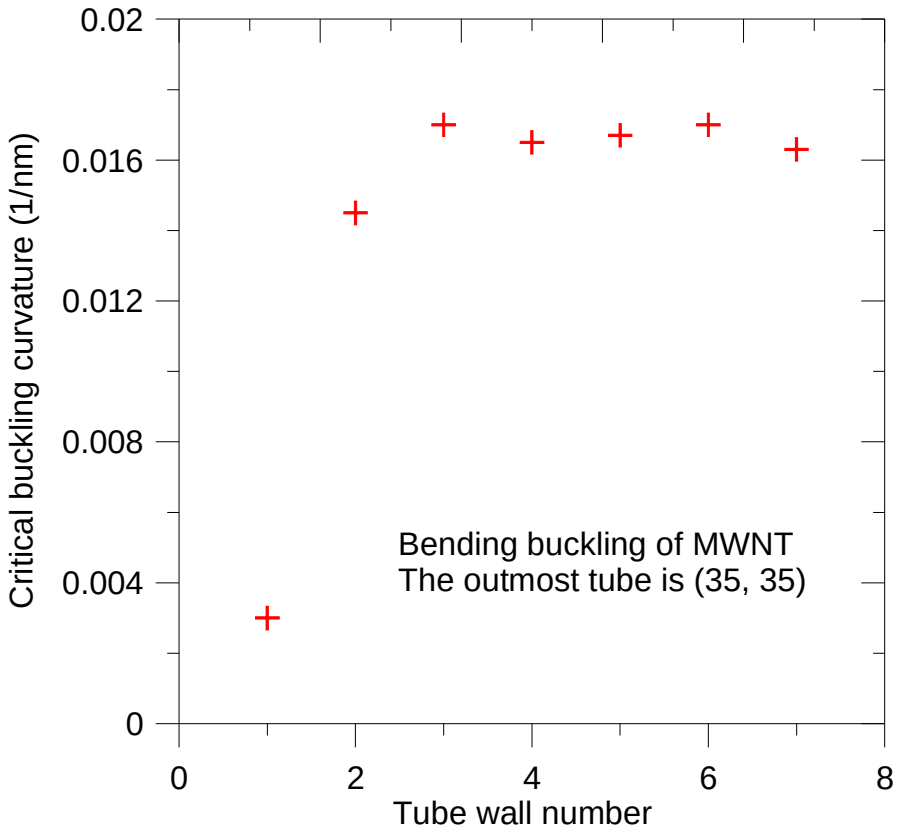

Figure 4.38: The variation of critical bending buckling curvature versus wall number

From observation of the buckling mode, it is found that, similar to compressive buckling, MWNTs with high section ratios (d_{CNT}/t) buckle "part-forwardly" whereas MWNTs with small section ratios buckle "all-together". As an example, the "part-forward" buckling phenomenon is shown in Figure 4.39. The outmost two layers (instead of only one layer) buckle first (Figure 4.39a) when bending angle is applied. Further increase of the global bending angle will gradually cause the rest of the layers to buckle. The above mentioned variation of κ_{cr} with the wall number can be explained by the buckling mode difference between SWNTs and MWNTs. For the case studied here, the section ratio is small so that the buckling mode of the DWNT is "all-together" mode. While for MWNTs with more than 3 layers, the buckling mode is "part-forward" mode with the outmost two layers buckle initially. It is the κ_{cr} of

DWNT that determines κ_{cr} of MWNTs with more than three layers (shown in Figure 4.38).

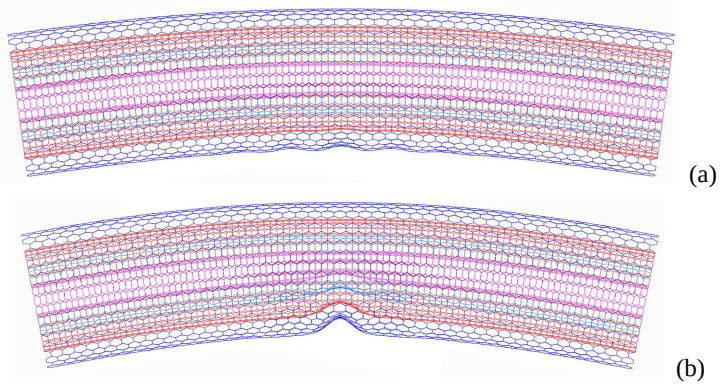

Figure 4.39: The bending buckling modes of MWNTs with four layers

4.6 Summary

In this chapter, the buckling behavior of carbon nanotubes (including SWNTs and MWNTs) is studied. Using the structural model developed in Chapter 2, numerical experiments such as axial compression and bending are performed to predict the initial buckling and post-buckling behavior of CNTs. The conclusions are listed below:

(a) The axial compressive buckling behavior is sensitive to the artificial perturbation imposed on the SWNT. Note that a perturbation, no matter what kind, is needed to initiate compressive buckling. To be able to compare various theoretical predictions, it is necessary to give the amplitude and mode of perturbation.

(b) Axial compressive buckling of SWNTs is size dependent. The aspect ratio

(L/d_{CNT}) and section ratio (d_{CNT}/t) are critical in determining both the buckling mode and the corresponding buckling strain. Three distinct buckling modes are predicted from the simulations: shell-buckling, mixed-buckling and beam-buckling for long, medium and short SWNTs, respectively.

(c) Bending buckling of SWNTs also shows some dependence on the nanotube size, especially for shorter tubes. The critical bending curvature and the buckling mode (number of kinks) are affected by the boundary conditions (BCs) applied to the tube. SWNTs are found to be more resistive to bending if pure bending BCs are applied. However, due to the difficulty in apply such displacement BCs on a hollow tube, "traditional bending" BCs are a good approximation but only for long tubes.

(d) Axial compressive buckling of MWNTs shows that two distinct buckling patterns can be predicted: "all-together" and "part-forward", depending on the section ratio (D/t) of the tube. Correspondingly, the critical compressive strain of a MWNT is comparable to the buckling strain of the outmost few tubes.

(e) A similar phenomenon of buckling difference for MWNTs with different section ratios is also found in studying the bending buckling.

CHAPTER 5 : EFFECT OF INTERPHACE ON EFFECTIVE MECHANICAL PROPERTIES OF CNTS REINFORCED COMPOSITES

5.1. Introduction

The combination of high stiffness, strength and aspect ratio makes carbon nanotubes (CNTs) ideal reinforcements for ultra high strength composites. Stiffness of carbon nanotube measured experimentally and calculated from simulations is of the order of 1000 GPa, while the nearest competitive fiber (SiC whiskers) has utmost 400 GPa in stiffness. CNTs have tensile strength of up to 200 GPa and can absorb large quantities of energy during elastic and inelastic deformations. Furthermore, the excellent electrical and optical properties of CNTs facilitate the development of multifunctional products. To take advantage of the remarkable properties of the CNTs, several key issues should be well solved, such as dispersion, alignment of CNTs in the host material, load transfer between the tube and the matrix. Through years, many theoretical and experimental practices have been given in addressing these issues. For example, techniques of dispersing and aligning the CNTs in the polymer matrix have been greatly improved. However, a comprehensive understanding of the load transfer mechanism between the nanotube and matrix is still limited. Especially, the effect of the tube-matrix interfacial properties on the bulk properties of the CNTs reinforced composites has to be studied which will benefit both the manufacture and application of these nanocomposite materials.

In order to make use of the very high stiffness and strength of the CNTs, the mechanical load must be transferred efficiently between matrix and CNTs in the composite. The adhesion between carbon nanotubes and matrix plays a key role in mechanical properties such as strength, stiffness and fracture resistance. Many experimental studies show evidence of good adhesion between the CNTs and the matrix; however, several other experiments suggest a discrepant conclusion. Tension and compression tests of multi-walled carbon nanotube (MWNT) reinforced epoxy composites show that the load carrying capacity of nanotubes is significant in such composites, and is much higher in compression than in tension (Schadler, 1998). The poor load transfer in tension may possibly be attributed to the extremely low interfacial shear stresses between the tubes and the matrix (Ajayan 2000). Studies of stress-induced fragmentation of carbon nanotubes in a polymer matrix suggest very good adhesion between CNT and polymer (Wagner, 1998). But it is unclear if the failures observed in the single-walled nanotube (SWNT) and MWNT composites are failures of individual tubes or local instabilities of the aggregates (MWNT or nanotube bundles). Clearly for SWNTs, the failure could result either from nanotubes pulling out of bundles or from the actual fracture of individual nanotubes in the bundles. Tensile tests of MWNT reinforced polystyrene composite film and in-situ TEM observation of the crack area show that the MWNTs tend to bridge the matrix cracks, and that there is excellent bonding between the nanotube and the matrix material (Wagner, 1998). Also, approaches to enhance the CNT-matrix interactions by non-bonded wrapping of matrix molecules as well as by functionalization between nanotubes and matrix have been suggested (Ajayan, 2000; Qian, 2000; Star, 2001; Jia, 1999). All these studies demonstrate efficient stress transfer between CNTs and matrices in composites, although a direct measurement of the nanotube interfacial properties may be more convincing.

Theoretical investigations of the load transfer in CNT reinforced composites usually adopt a nanotube-matrix interfacial shear mechanism and fiber pullout model at the

molecular level. Pullout processes of a single walled carbon nanotube (SWNT) from a polymer matrix were simulated by molecular dynamics, for both non-bond interface (Liao, 2001; Frankland, 2003) and interface with chemical cross-links (Frankland, 2002). The force balance of the CNT fiber under axial stretching and shearing was described by a simple interfacial shear model (Wagner, 2002), where also the relationships between the critical length and the shear strength of CNTs were discussed, including the effect of parameters such as CNT geometry and interfacial characteristics. The pullout process was described by a local density approximation model based on elastic shell theory (Lau, 2003). In the same study the relationship between interfacial shear stress and the embedding length was derived, and it was found that a long fiber length is necessary for a steady stress transfer. It must be noted that, even though the shear strength failure model gives a description of the CNT-matrix interaction, the determination of shear strength still remains unclear. In addition, the high surface area of nanotubes creates a large interfacial region (or interphase) which can have properties different from the bulk matrix (Figure 5.1). The effect of the properties of the interphase should be addressed.

There are also a few studies that focus on the stiffening effect of CNTs on composite moduli, using elastic continuum micromechanics. The effective moduli of the composite are determined by applying the finite element method (FEM) to a representative volume element (RVE) of the composite (Y. Liu, 2003). The influence of fiber waviness on the effective moduli is demonstrated, by analytically and via numerical simulation in (Fisher, 2002). These studies show the applicability of continuum mechanics and micromechanics in predicting the effective moduli of CNT reinforced composite materials. However, the load transfer mechanism along the CNT fiber is inadequately studied. Especially the effect of fiber length on the stiffening of the composite is not well understood.

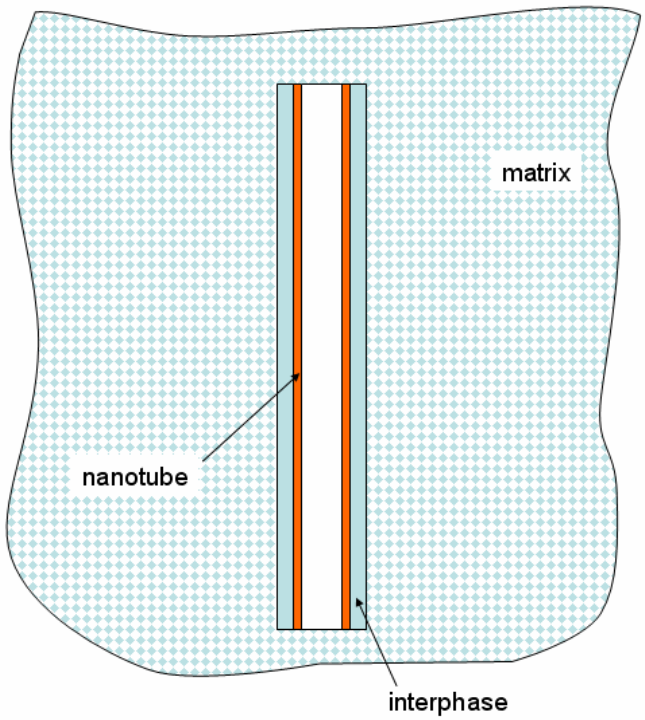

Figure 5.1: A single-walled carbon nanotube embedded in the polymer matrix

It is the objective of the present work to to investigate the effective moduli of the CNT reinforced polymer composite, with emphasis on the influence of CNT length and CNT-matrix interphase on the stiffening of the composite. First, the strain energy change due to the inclusion of a single CNT in an infinite matrix is calculated using the finite element method analysis (FEA). Then the "critical" fiber length for full load transfer between the CNT and the matrix is determined by evaluating the changes in strain energy for different fiber lengths. The effective moduli of the composite are then obtained through a dilute solution method. Two different loadings, namely longitudinal stretching and hydrostatic tension are studied for the computations of effective Young's modulus and bulk modulus respectively.

5.2 The Strain-Energy-Change Due to a SWNT Inclusion in an Infinite Matrix

Under certain loading conditions, the introduction of a stiff fiber into an infinite soft matrix can lead to a decrease in strain energy, while a hole or a crack in the matrix can cause an increase. The determination of the strain-energy-change in an infinite matrix due to the presence of a single fiber is essential to calculating the effective elastic moduli of the corresponding composites based on various micromechanics models (Shen and Yi, 2001; Shen and Li, 2003). In the present study, the strain energy of a single-walled carbon nanotube (SWNT) embedded in an infinite matrix (Figure 5.2) is solved by FEM because an analytical solution appears to be hopelessly complicated. The change in the strain energy then can easily be obtained by comparing the result with that of a pure matrix where the solution is known analytically.

5.2.1 The finite element model

The SWNT is treated as a continuum homogeneous isotropic hollow cylinder with closed caps at both ends. This hollow cylinder is then embedded into a homogeneous isotropic matrix which is subject to a far field stress (Figure 5.2). For simplicity, two different far field loading conditions, namely longitudinal stretching and hydrostatic tension are studied, although three more loading conditions may be needed for a complete evaluation of the problem (Shen and Yi, 2001; Shen and Li, 2003). Making use of the axisymmetric of the geometry and loading conditions, only one quarter of the domain is modeled employing 2-D axisymmetric elements with the proper symmetry constraints (Figure 5.3).

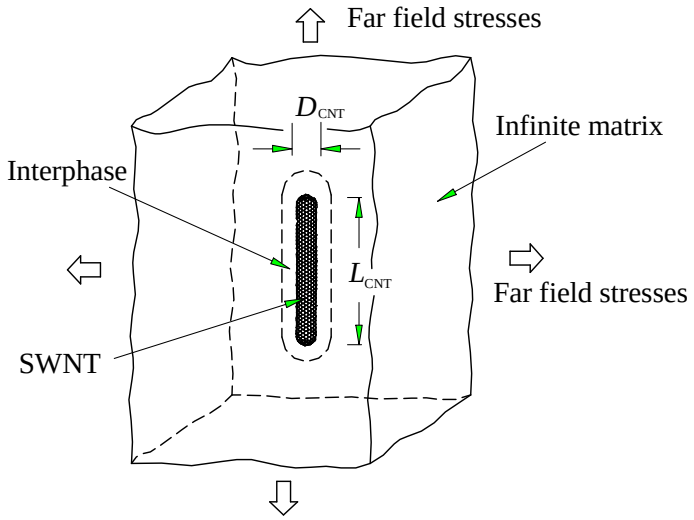

Figure 5.2: A single SWNT surrounded by an interphase in an infinite matrix.

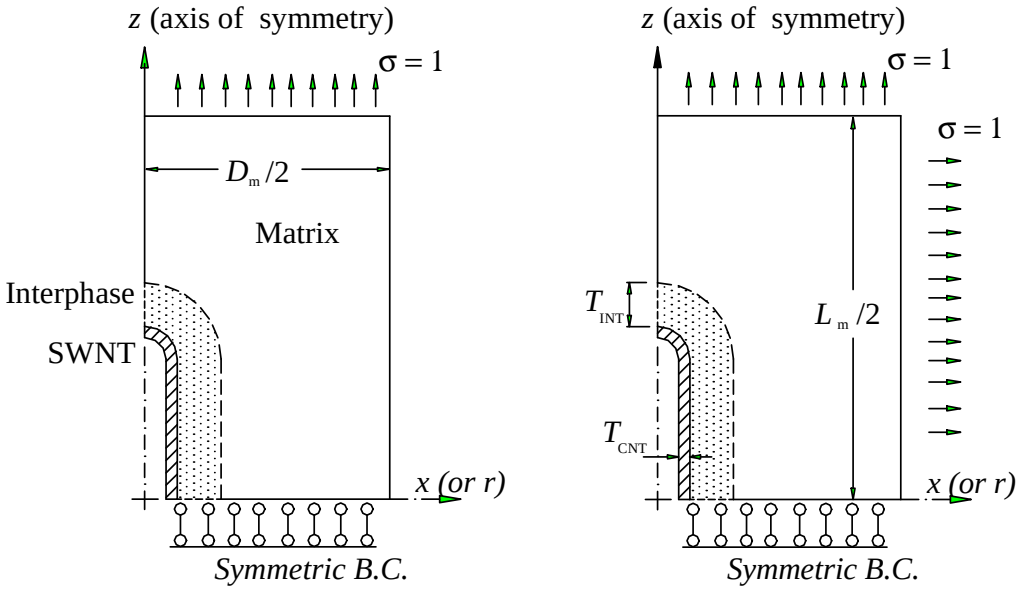

Figure 5.3: (a) FEM model with uniaxial loading; (b) FEM model with hydrostatic loading.

To simulate the infinite matrix, a sufficiently large volume has to be taken into computation. A satisfactory size for the matrix was determined by enlarging the matrix volume incrementally until the change in strain energy between increments

became negligible. As a result, the matrix can be treated as infinite if the diameter and length of the model are set as: $D_m = 30D_{CNT}$ and $L_m = L_{CNT} + 30D_{CNT}$, where L_{CNT} is the length of the SWNT (Figure 5.2-5.3).

The existence of an interphase between the CNT and the matrix is considered and it is thought to be of the same length scale as the width of a nanotube for a SWNT surrounded by polymer molecules (Wise, 2001), although the mechanical properties of the interphase are not known. In the present paper, a homogeneous isotropic interphase medium of the same shape as the SWNT is inserted between the SWNT and matrix. The thickness of the interphase (T_{INT}) is assumed to be equal to the mean radius (D_{CNT}) of SWNT (Figure 5.3). Both "hard" and "soft" interphases are studied, with the Young's moduli and Poisson's ratios listed in Table 5.1.

Table 5.1: Properties of SWNT and matrix

	Young's Modulus	Poisson's Ratio
SWNT	1,000 GPa	0.28
Matrix (Polymer)	5 GPa	0.4
Interphase	Hard: $E_{INT} = 10\,E_m$ Soft: $E_{INT} = 0.3\,E_m$	0.4

An armchair SWNT (10, 10) with diameter D_{CNT} = 1.357nm is chosen for the analysis. The thickness of the tube is assumed to be 0.34 nm, which is the distance between two graphite layers. The material properties of the SWNT, matrix and interphase are assumed to be isotropic and homogeneous (Table 5.1). The units of length and force are nanometer (nm) and nanoNewton (nN), respectively. Thus the stresses and moduli are expressed in GPa. The unit of strain energy is 10^{-18} J or

(nN*nm).

Because of the drastic differences in mechanical properties between the SWNT and matrix (interphase), special care has to be taken to ensure the accuracy of the results for the calculated stresses and strain energy. Therefore, in areas adjacent to the SWNT, elements of comparable size are used. An example mesh of the quarter model is shown in Figure 5.4.

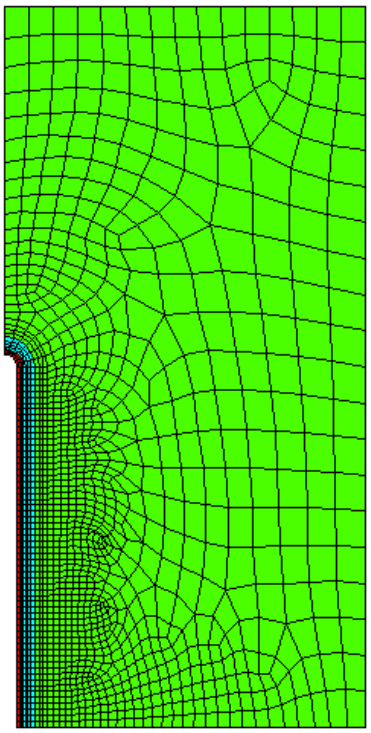

Figure 5.4: The finite element mesh of the quarter model

5.2.2 The evaluation of strain-energy-change

The strain energy of pure matrix can easily be obtained analytically. The strain energy expressions for a cylinder of diameter D_m and length L_m under uniaxial and hydrostatic loading conditions are:

$$U_1 = \frac{\sigma^2}{2E_m}\frac{\pi D_m{}^2 L_m}{4} \qquad \text{(uniaxial loading)}, \qquad (5.1)$$

$$U_2 = \frac{\sigma^2}{2K_m}\frac{\pi D_m{}^2 L_m}{4} \qquad \text{(Hydrostatic loading)}, \qquad (5.2)$$

where E_m and K_m are the Young's modulus and bulk modulus of the matrix, respectively, and σ is the far field stress. Subtracting (5.1) or (5.2) from the corresponding FEM results, the strain-energy-changes (ΔU_1 and ΔU_2) due to the SWNT inclusion can be obtained.

To study the influence of fiber length on the strain-energy-change, we vary the SWNT aspect ratio (L_{CNT}/D_{CNT}) from 5 to 800 (the length of the CNT varies from 6.785 nm to 1085.6 nm), and calculate the strain-energy-changes for each SWNT aspect ratio as explained above. Dividing the strain energy change by the corresponding fiber length, the strain-energy-changes per unit length are obtained as: $\Delta U_1 / L_{CNT}$ and $\Delta U_2 / L_{CNT}$. Figure 5.5 and 5.6 show the variation of $\Delta U_1 / L_{CNT}$ and $\Delta U_2 / L_{CNT}$ with the fiber aspect ratio. To study the influence of the interphase, three cases are considered: no interphase, "hard" interphase (Young's modulus $E_{INT} = 10E_m$) and "soft" interphase (Young's modulus $E_{INT} = 0.3E_m$).

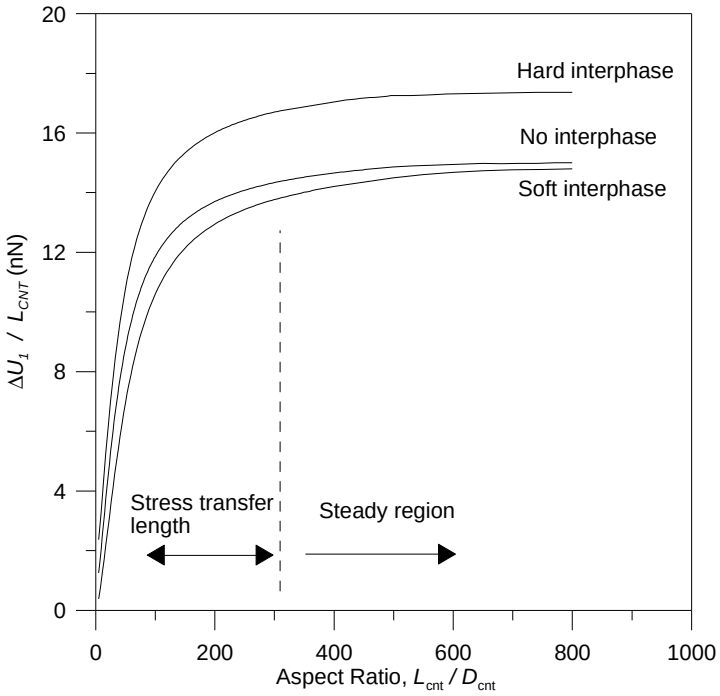

Figure 5.5: Strain-energy-change per unit length (uniaxial loading)

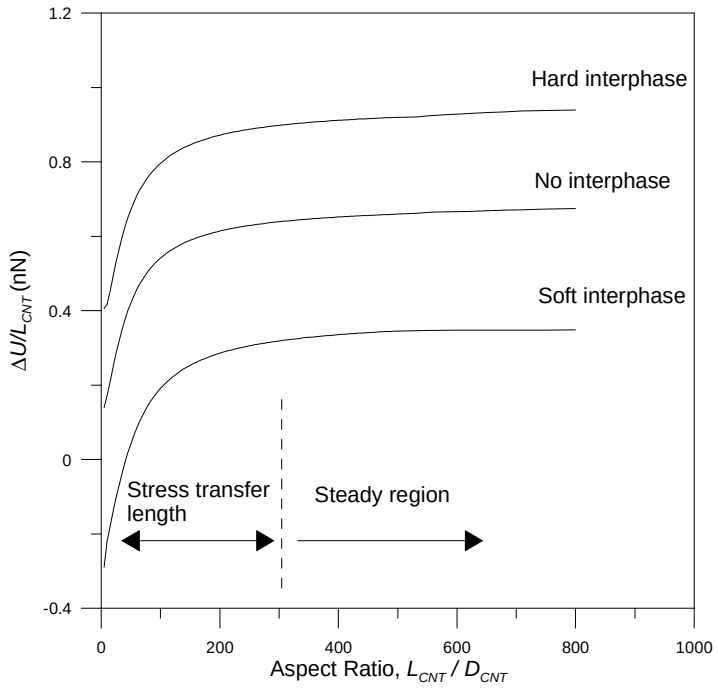

Figure 5.6: Strain-energy-change per unit length (hydrostatic loading)

From Figure 5.5 and 5.6, it can be seen that there exists a region where $\Delta U_1 / L_{\mathrm{CNT}}$ or $\Delta U_2 / L_{\mathrm{CNT}}$ increases dramatically with the increase of the aspect ratio ($L_{\mathrm{CNT}} / D_{\mathrm{CNT}}$), beyond which it steadily converges to a certain value. This value is closely related to the stress distribution along the SWNT fiber. It is well know that for a long fiber, a uniform distribution of stresses can be attained in the middle section of the fiber (see Figure 5.7 and 5.8 for example). For a very long fiber the range of this uniform region can become sufficiently larger than the non-uniform regions at the fiber ends. Thus the stresses in the uniform region are dominant compared to the non-uniform regions and a full stress transfer between the SWNT and the matrix is achieved. Therefore the strain-energy-change per unit length becomes a constant for a very long fiber. In other words, $\Delta U_1 / L_{\mathrm{CNT}}$ or $\Delta U_2 / L_{\mathrm{CNT}}$ can be used to quantitatively examine the efficiency of load transfer between the SWNT and the matrix.

If we denote the convergent value as $(\Delta U_i / L_{\mathrm{CNT}})^*$ (where i=1, 2), then a "critical" fiber length $(L_{\mathrm{CNT}})_{\mathrm{cr}}$ can be defined at the point where $(\Delta U_i / L_{\mathrm{CNT}})_{cr} = 90\% \cdot (\Delta U_i / L_{\mathrm{CNT}})^*$. This will give us a quantitative criterion as to whether load transfer occurred. The "critical" fiber lengths for various loadings and different interphase properties are listed in Table 5.2.

Table 5.2 shows that the "critical" fiber length for full tube-matrix load transfer is influenced by the interphase and its mechanical properties. In the longitudinal stretching case, for full load transfer a 25% longer fiber is needed for a soft interphase (E_{INT}=0.3 E_{m}). However, a hard interphase (E_{INT}=10 E_{m}) can shorten the "critical" length by more than 18%. This effect is even more pronounced for the hydrostatic loading condition. More than 40% longer SWNT fibers are needed for efficient load transfer if a soft tube-matrix interphase exists, while the hard interphase can reduce the length requirement by about 25%.

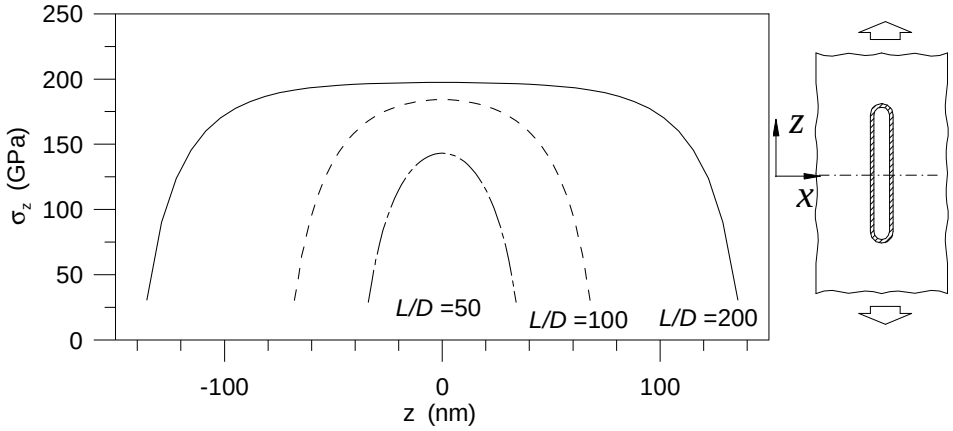

Figure 5.7: Longitudinal stress distributions along the SWNT wall for different fiber lengths.

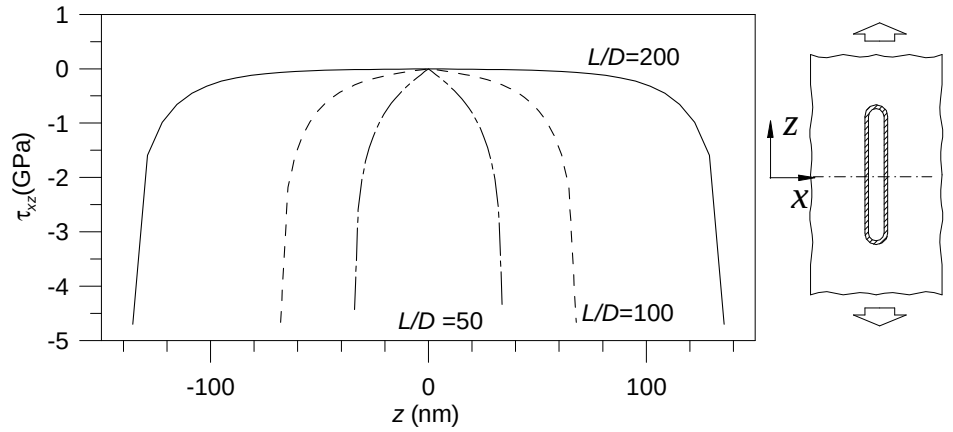

Figure 5.8: Shear stress distributions along the tube-matrix interface for different fiber lengths.

Table 5.2: Values of $(L_{\mathrm{CNT}}/D_{\mathrm{CNT}})_{cr}$, L_{cr} and $(\Delta U_i/L_{CNT})_{cr}$

Load Condition	Interphase Property	$(L_{\mathrm{CNT}}/D_{\mathrm{CNT}})_{cr}$	L_{cr} (nm)	$(\Delta U_i/L_{\mathrm{CNT}})_{cr}$
Longitudinal stretching	No interphase	198	233.4	13.687
	$E_{\mathrm{INT}}=10\,E_{\mathrm{m}}$	161	218.5	15.622
	$E_{\mathrm{INT}}=0.3\,E_{\mathrm{m}}$	246	333.8	13.32
Hydrostatic loading	No interphase	200	271.4	0.614
	$E_{\mathrm{INT}}=10\,E_{\mathrm{m}}$	150	230.55	0.846
	$E_{\mathrm{INT}}=0.3\,E_{\mathrm{m}}$	279	378.6	0.314

5.3 Effective Moduli Derived from Dilute Solution

The strain energy change due to the inclusion of a single fiber can be used to derive the effective moduli of the composite. If the SWNT fiber volume fraction (ϕ) is small and assume non-interaction between inclusions, dilute solutions of the effective moduli of the composite can be derived (Shen and Yi, 2001; Shen and Li, 2003).

For longitudinal stretching, the strain energy of the composite can be expressed in terms of the effective modulus E_c:

$$U_c=\frac{1}{2}\frac{\sigma^2 V_c}{E_c}, \tag{5.3}$$

where, V_c is the volume of the composite. Using the non-interaction assumption, the strain energy of the composite can be thought as the summation of strain energy of pure matrix and that of strain energy change due to the inclusion of SWNTs.

$$\frac{1}{2}\frac{\sigma^2 V_c}{E_c} = \frac{1}{2}\frac{\sigma^2 V_c}{E_m} - N(\Delta U_1) \quad , \tag{5.4}$$

where N is the number of SWNTs. Thus, the effective modulus can be expressed as,

$$\frac{1}{E_c} = \frac{1}{E_m} - \frac{8\left(\frac{\Delta U_1}{L}\right)\phi}{\pi D_{\mathrm{CNT}}{}^2 \sigma^2} \quad . \tag{5.5}$$

Because of small fiber volume fraction ($\phi << 1$), the above equation can be simplified as,

$$: E_c = E_m\left(1 + \frac{8E_m}{\pi D_{\mathrm{CNT}}{}^2 \sigma^2}\frac{\Delta U_1}{L}\phi\right). \tag{5.6}$$

Similarly, for hydrostatic loading, the effective bulk modulus of the composite is,

$$K_c = K_m\left(1 + \frac{8K_m}{\pi D_{\mathrm{CNT}}{}^2 \sigma^2}\frac{\Delta U_2}{L}\phi\right), \tag{5.7}$$

where E_m and K_m are the Young's modulus and bulk modulus of the matrix respectively, and σ is the applied far field stress. The values of $\Delta U_1 / L_{\mathrm{CNT}}$ and $\Delta U_2 / L_{\mathrm{CNT}}$ are known from Figure 5.5 and 5.6.

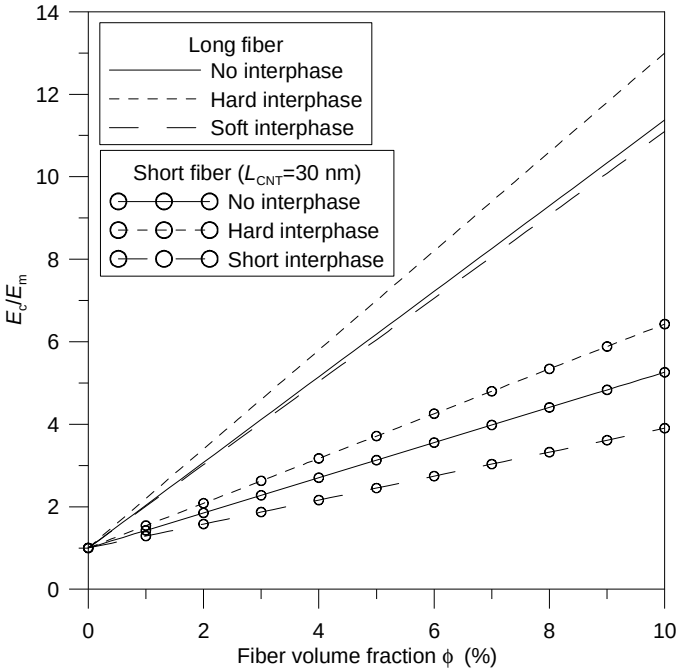

Figure 5.9: Effective Young's modulus

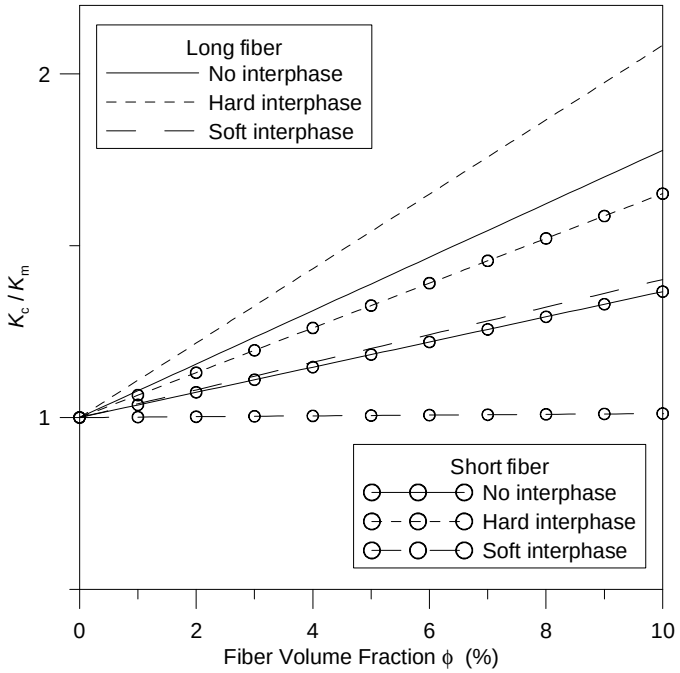

Figure 5.10: Effective bulk modulus.

As mentioned earlier, for a very long fiber, $\Delta U_1 / L_{CNT}$ and $\Delta U_2 / L_{CNT}$ will take the convergent values of the corresponding curves in Figure 5.5 and 5.6. To study the influence of fiber length, the calculations are carried out for both short and long fibers. The length of the short fiber is assumed to be 30 nm (aspect ratio L_{CNT} / D_{CNT} =22.1). The effective moduli (E_c and K_c) as functions of the fiber volume fraction are plotted in Figure 5.9 and 5.10.

From Figure 5.9, it can be seen that the longitudinal Young's modulus of the composite is significantly enhanced. With 2% addition of short SWNT fiber (no interphase), the composite modulus is increased by about 85%, which is in good agreement with the solutions obtained by the representative volume element (RVE) (Y. Liu 2003). Long fiber can greatly strengthen this reinforcing effect. With 2% addition of long SWNT fiber (no interphase), the composite modulus can be increased by about 200%. Although fabrication of very long SWNT fibers (in the order of μm) is quite trivial now, there are no data showing that the lengths of the SWNTs used in the composites are of the order of μm. Thus the effective longitudinal modulus can be much lower than the expected value, which may partially explain the discrepancy between the experimental data and the theoretically predicted values (other reasons are fiber waviness (Fisher, 2002), agglomeration, and so on).

Hard interphase (E_{INT} =10 E_m) can help the stiffening effect of the SWNT in the composite, however, with only a slight advantage over the non-interphase case (about 10%) and the soft interphase case (less than 15%) judging from E_c / E_m. This indicates that the effective moduli of the composite are not sensitive to the existence of interphase and its mechanical properties.

Figure 5.10 indicates that the enhancement of the bulk modulus by SWNT is less when compared to that of the longitudinal Young's modulus.

5.4 Summary

The solutions of the strain energy changes due to a SWNT embedded in an infinite matrix are obtained through numerical method. A “critical” SWNT fiber length is defined for full load transfer between the SWNT and the matrix, through the evaluation of the strain energy changes for different fiber lengths. The strain energy change is also used to derive the effective longitudinal Young’s modulus and effective bulk modulus of the composite, using a dilute solution. The following conclusions can be drawn:

The fiber SWNT length is critical to both the load transfer efficiency and the stiffening of the composite. To achieve full load transfer between the SWNT (10, 10) and the matrix, the length of SWNT fibers should be longer than a “critical” length (271 nm) if no weak interphase exists between the SWNT and the matrix. The effective modulus calculated for long SWNT fibers may be about twice as that calculated for short SWNT fibers. This can partially explain the discrepancy between experimental and theoretical results for nanocomposites, since the fibers may not be sufficiently long.

The SWNT-matrix interphase plays an important role in transferring the load between the SWNT and the matrix. Judging from the “critical” length for fully load transfer, the existence of a hard interphase ($E_{INT} = 10E_{\mathrm{m}}$) can help reduce the “critical” fiber length up to 46% compared with that of a soft interphase ($E_{\mathrm{INT}} = 0.3E_{\mathrm{m}}$). However, studies of the effective moduli of the composite suggest they are not sensitive to the interphase. This suggests that the improvement of tube-matrix interphase is very important for an efficient load transfer in the composite, but this will slightly affect its stiffness properties.

CHAPTER 6 : CONCLUSIONS AND FUTURE WORKS

6.1 Conclusions

In this thesis, the mechanical behavior of carbon nanotubes (CNTs) and their reinforced composites was studied using the continuum mechanics models. For single-walled nanotubes (SWNTs), a structural model based on molecular mechanics was developed. The model was then extended to study the mechanical behavior of multi-walled nanotubes (MWNTs). The validity of these models was confirmed through predicting effective mechanical constants such as Young's modulus, shear modulus and bending stiffness of CNTs, as well as the interlayer pressure and shear between graphite layers. The structural models were implemented for studying the buckling behavior of carbon nanotubes (SWNTs and MWNTs) under axial compression and bending deformations. Another portion of the thesis was contributed to the CNTs reinforced composites in which the effect of interphase between the tube and the host material was discussed. The major new contributions of the current work to carbon nanotube mechanics are summarized as follows.

The developed structural model of CNTs established an excellent relationship between the continuum mechanics and the molecular mechanics approaches. The potentials associated with the atomic interactions of covalent bonds within a CNT were evaluated by the strain energies of the beam element as a structural mimic of the bond. In contrast to the original model the out-of-plane deformation (inversion) of the bond was distinguished from the in-plane deformation in the current model. Consequently, the current model was able to study the bending of the graphite layer in a CNT. Therefore, the current model can be used to study the local buckling of CNTs under mechanical loads (compression and bending). Compared to molecular dynamics computations, the analysis based on the current continuum mechanics model is significantly cost economic.

Several key issues involved in the study of buckling behavior of CNTs under axial compression and bending loads were discussed. Both the onset of buckling and the mode of buckling shape were found to be sensitive to the perturbation (size and mode) superimposed onto a CNT to trigger the buckling. This explained the discrepancy of results from various approaches in the literature. The critical buckling strain of a CNT under compression was found to rely on the tube chirality. Nanotubes with symmetric structure (armchair, zigzag) are more efficient in resisting buckling compared to unsymmetrical nanotubes. For bending buckling, the critical curvature and the buckling mode were found to be sensitive to the boundary conditions (BCs) applied at the ends of the nanotube. While most simulations in literature used roughly "pure bending" BCs, the current work realized a better approximation of pure bending BCs through iteration strategies, which resulted in higher critical curvature upon buckling. Simulations of buckling behavior of MWNTs revealed two different buckling processes: "part-forward" and "all-together". For MWNTs with small section ratio (d_{CNT}/t), buckling is initiated at the outmost several layers and transmitted "part-forwardly" to the rest layers. Whereas for a MWNT with large section ratio, the tube buckles "all-together" at the onset of buckling.

Continuum mechanics was also used to model the CNTs reinforced composites in which the CNT, host material (matrix) and the CNT-matrix interphase were modeled by a representative volume element (RVE). The analysis of the RVE showed that a critical tube length is required in order to establish fully load transfer between the high stiffness tube and the matrix. This critical length was found to rely on the tube-matrix interphase properties. The effect of the tube length and the properties of the interphase on the other hand, the effective properties of the reinforced composite were also discussed

6.2 Future Works

The current developed mode of CNTs can be applied to future study of a wide range of topics. Several of them are listed below.

(1) The effective mechanical properties of CNTs with defects. As introduced previously in Chapter 1, a SWNT can have typical White-Stone (5-7-7-5) defects due to synthesis problems. Such defects may degrade the stiffness and strength of the nanotube to some extent. The effect of such defects can be studied by the current structural model with certain modification according to the defect physics (such as new bond length and force constants). Factors such as fraction and distribution of the defects can be investigated.

(2) Mechanical behavior of CNT bundles can also be studied by the current model. Because the interaction among nanotubes in a bundle is van der Waals force, which can be modeled by the same approach used for MWNTs in the current study. The effective mechanical properties and the buckling behavior of the CNT bundles can be predicted.

(3) Nanoindentation test of an array of SWNTs can be performed through numerical simulation in order to examine and verify the experimental results.

(4) The current model can also be used to study the mechanical behavior of CNTs within nanoelectromechanical systems (NEMS). These nanotube-based devices include: nanoresonator (oscillators) in which the CNT serves as a high-frequency component, nano-valves, nano-switches.

Bibliography

1. Ajayan, P.M., L.S. Shadler, C. Giannaris, and A. Rubio, *Single-Walled Carbon Nanotube - Polymer Composites: Strength and Weakness.* Advanced Materials, 2000. **12**: p. 750-753.

2. Akita, S. and Y. Nakayama, *Interlayer Sliding Force of Individual Multiwall Carbon Nanotubes.* Jpn. J. Appl. Phys. , 2003. **42**: p. 4830-4833.

3. Arroyo, M. and T. Belytschko, *Nonlinear Mechanical Response and Rippling of Thick Multiwalled Carbon Nanotubes.* Physical Review Letters, 2003. **91**: p. 215505.

4. Belytschko, T., S.P. Xiao, G.C. Schatz, and R.S. Ruoff, *Atomistic simulations of nanotube fracture.* Physical Review B, 2002. **65**(235430): p. 1-8.

5. Buehler, M.J., Y. Kong and H. Gao, *Deformation Mechanisms of Very Long Single-Wall Carbon Nanotubes Subject to Compressive Loading.* Journal of Engineering Materials and Technology, 2004. **126**(3): p. 245-249.

6. Cao, G. and X. Chen, *Buckling behavior of single-walled carbon nanotubes and a targeted molecular mechanics approach.* Physical Review B (Condensed Matter and Materials Physics), 2006. **74**(16): p. 165422-10.

7. Cao, G. and X. Chen, *Buckling of single-walled carbon nanotubes upon bending: Molecular dynamics simulations and finite element method.* Physical Review B (Condensed Matter and Materials Physics), 2006. **73**(15): p. 155435-10.

8. Cao, G. and X. Chen, *The effect of the displacement increment on the axial compressive buckling behaviours of single-walled carbon nanotubes.* Nanotechnology, 2006. **17**: p. 3844-3855.

9. Cao, G. and X. Chen, *Mechanisms of nanoindentation on single-walled carbon*

nanotubes: The effect of nanotube length. Journal of Materials Research, 2006. **21**(4): p. 1048-1070.

10. Cao, G. and X. Chen, *The effects of chirality and boundary conditions on the mechanical properties of single-walled carbon nanotubes.* International Journal of Solids and Structures 2007. **44**: p. 5447–5465.

11. Chang, T. and H. Gao, *Size-dependent elastic properties of a single-walled carbon nanotube via a molecular mechanics model.* Journal of the Mechanics and Physics of Solids, 2003. **51**: p. 1059-1074.

12. Chang, T., J. Geng and X. Guo, *Chirality- and size-dependent elastic properties of single-walled carbon nanotubes.* Applied Physics Letters, 2005. **87**(25): p. 251929-3.

13. Chang, T., W. Guo and X. Guo, *Buckling of multiwalled carbon nanotubes under axial compression and bending via a molecular mechanics model.* Physical Review B, 2005. **72**: p. 064101 1-11.

14. Chang, T. and J. Hou, *Molecular dynamics simulations on buckling of multiwalled carbon nanotubes under bending.* Journal of Applied Physics, 2006. **100**(11): p. 114327-5.

15. Chang, T., G. Li and X. Guo, *Elastic axial buckling of carbon nanotubes via a molecular mechanics model.* Carbon, 2005. **43**: p. 287–294.

16. Cornell, W.D., P. Cieplak, C.I. Bayly, I.R. Gould, K.M. Merz, D.M. Ferguson, and D.C. Spellmeyer, *A second generation force field for the simulation of proteins, nucleic acids, and organic molecules.* Journal of the American Chemical Society 1995. **117**: p. 5179-5197.

17. Falvo, M.R., G.J. Clary, R.M. Taylor, V. Chi, F.P. Brooks, S.W. Jr., and R. Superfine, *Bending and buckling of carbon nanotubes under large strain.*

Nature, 1997. **389**(582).

18. Fisher, F.T. and R.D. Bradshaw, *Effects of nanotube waviness on the modulus of nanotube-reinforced polymers.* Applied Physics Letters, 2002. **80**: p. 4647-4652

19. Frankland, S.J.V., D.W. Caglar, D.W. Brenner, and M. Griebel, *Molecular simulation of the influence of chemical cross-links on the shear strength of carbon nanotube-polymer interfaces.* Journal of Physical Chemistry B, 2002. **106**: p. 3046-3048.

20. Frankland, S.J.V. and V.M. Harik, *Analysis of carbon nanotube pull-out from a polymer matrix.* Surface Science Letters 2003. **525**: p. L103-L108.

21. Grujicic, M., G. Cao, B. Pandurangana, and W.N. Royb, *Finite element analysis-based design of a fluid-flow control nano-valve.* Mater. Sci. Eng., B 2005. **117**(53-61).

22. Guo, W., Y. Guo, H. Gao, Q. Zheng, and W. Zhong, *Energy Dissipation in Gigahertz Oscillators from Multiwalled Carbon Nanotubes.* Physical Review Letters, 2003. **91**(12): p. 125501 1-4.

23. Harik, V.M., *Ranges of applicability for the continuum beam model in the mechanics of carbon nanotubes and nanorods.* Solid State Communnication, 2001. **120**: p. 331–335.

24. He, X.Q., S. Kitipornchai and K.M. Liew, *Buckling analysis of multi-walled carbon nanotubes: a continuum model accounting for van der Waals interaction.* Journal of Mechanics and Physics of solids, 2005. **53**: p. 303-326.

25. Hernandez, E., C. Goze, P. Bernier, and A. Rubio, *Elastic Properties of C and BxCyNz Composite Nanotubes.* Physical Review Letters, 1998. **80**(20): p. 4502.

26. Huhtala, M., A.V. Krasheninnikov, J. Aittoniemi, S.J. Stuart, K. Nordlund, and K. Kaski, *Improved mechanical load transfer between shells of multiwalled carbon nanotubes.* Physical Review B, 2004. **70**: p. 045404 1-8.

27. Iijima, S., C. Brabec, A. Maiti, and J. Bernholc, *Structural flexibility of carbon nanotubes.* The Journal of Chemical Physics, 1996. **104**(5): p. 2089-2092.

28. Jia, Z., Z. Wang, C. Xu, J. Liang, B. Wei, D. Wu, and S. Zhu, *Study on poly(methyl methacrylate)/ carbon nanotube composites.* Materials Science and Engineering, 1999. **A271**: p. 395-400.

29. Krishnan, A., E. Dujardin, T.W. Ebbesen, P.N. Yianilos, and M.M.J. Treacy, *Young's modulus of single-walled nanotubes* PHYSICAL REVIEW B, 1998. **58**(20): p. 14013-14019.

30. Kurti, J., G. Kresse and H. Kuzmany, *First-principles calculations of the radial breathing mode of single-wall carbon nanotubes.* Physical Review B, 1998. **58**(14): p. R8869.

31. Lau, K.-T., *Interfacial Bonding Characteristics of Nanotube/Polymer Composites.* Chemical Physics Letters 2003. **37**: p. 399-405.

32. Lau, K.-t., C. Gu and D. Hui, *A critical review on nanotube and nanotube/nanoclay related polymer composite materials.* Composites : Part B, 2006. **37**: p. 425-436.

33. Lennard, J.E. and I. Jones, *On the determination of molecular fields.* Proc. R. Soc. London A, 1924. **106**: p. 441-462.

34. Leung, A.Y.T., X. Guo, X.Q. He, H. Jiang, and Y. Huang, *Postbuckling of carbon nanotubes by atomic-scale finite element.* Journal of Applied Physics, 2006. **99**(12): p. 124308-5.

35. Li, C. and T.-W. Chou, *Elastic moduli of multi-walled carbon nanotubes and*

the effect of van der Waals forces. Composites Science and Technology, 2003. **63**(11): p. 1517-1524.

36. Li, C. and T.-W. Chou, *Single-walled carbon nanotubes as ultrahigh frequency nanomechanical resonators*. Physical Review B (Condensed Matter and Materials Physics), 2003. **68**(7): p. 073405-3.

37. Li, C. and T.-W. Chou, *A structural mechanics approach for the analysis of carbon nanotubes.* International Journal of Solids and Structures, 2003. **40**(10): p. 2487-2499.

38. Li, C. and T.-W. Chou, *Elastic properties of single-walled carbon nanotubes in transverse directions.* Physical Review B (Condensed Matter and Materials Physics), 2004. **69**(7): p. 073401-3.

39. Li, C. and T.-W. Chou, *Modeling of elastic buckling of carbon nanotubes by molecular structural mechanics approach.* Mechanics of Materials, 2004. **36** p. 1047–1055.

40. Li, C. and T.-W. Chou, *Modeling of carbon nanotube clamping in tensile tests.* Composites Science and Technology, 2005. **65**: p. 2407-2415.

41. Liao, K. and S. Li, *Interfacial characteristics of a carbon nanotube-polystyrene composite system.* Applied Physics Letters, 2001. **79**(25): p. 4225-4227.

42. Liew, K.M., C.H. Wong, X.Q. He, M.J. Tan, and S.A. Meguid, *Nanomechanics of single and multiwalled carbon nanotubes.* Physical Review B, 2004. **69**(115429): p. 1-8.

43. Liew, K.M., C.H. Wong and M.J. Tan, *Buckling properties of carbon nanotube bundles.* Applied Physics Letters, 2005. **87**(4): p. 041901-3.

44. Liu, B., H. Jiang, Y. Huang, S. Qu, and M.-F. Yu, *Atomic-scale finite element*

method in multiscale computation with applications to carbon nanotubes. Physical Review B, 2005. **72**: p. 035435-1-8.

45. Liu, P., Y.W. Zhang, C. Lu, and K.Y. Lam, *Tensile and bending properties of double-walled carbon nanotubes.* J. Phys. D: Appl. Phys, 2004. **37**: p. 2358–2363.

46. Liu, Y.J. and X.L. Chen, *Evaluation of the effective material properties of carbon nanotube- based composites using a nanoscale representative volume element.* Mechanics of Materials 2003. **35**: p. 69-81.

47. Lourie, O., D.M. Cox and H.D. Wagner, *Buckling and Collapse of Embedded Carbon Nanotubes.* Physical Review Letters, 1998. **81**(8): p. 1638-1641.

48. Lu, J.P., *Elastic Properties of Carbon Nanotubes and Nanoropes.* Physical Review Letters, 1997. **79**(7): p. 1297-1300.

49. Miyamoto, Y., A. Rubio, M.L. Cohen, and S.G. Louie, *Chiral tubules of hexagonal BC_{2}N.* Physical Review B, 1994. **50**(7): p. 4976.

50. Miyamoto, Y., A. Rubio, S.G. Louie, and M.L. Cohen, *Electronic properties of tubule forms of hexagonal BC_{3}.* Physical Review B, 1994. **50**(24): p. 18360.

51. Mylvaganam, K., T. Vodenitcharova and L.C. Zhang, *The bending-kinking analysis of a single-walled carbon nanotube—a combined molecular dynamics and continuum mechanics technique.* Journal of Material Science, 2006. **41**: p. 3341-3347.

52. Odegard, G.M., T.S. Gates, L.M. Nicholson, and K.E. Wise, *Equivalent-continuum modeling of nano-structured materials.* Composites Science and Technology, 2002. **62**: p. 1869-1880.

53. Odegard, G.M., T.S. Gates, L.M. Nicholson, and K.E. Wise,

Equivalent-Continuum Modeling With Application to Carbon Nanotubes. 2002, Langley Research Center: Hampton, Virginia. p. 30.

54. Odegard, G.M., T.S. Gates, K.E. Wise, C. Park, and E.J. Siochi, *Constitutive modeling of nanotube–reinforced polymer composites.* Composites Science and Technology 2003. **63**: p. 1671-1687.

55. Pantano, A., M.C. Boyce and D.M. Parks, *Nonlinear Structural Mechanics Based Modeling of Carbon Nanotube Deformation.* Physical Review Letters, 2003. **91**(14): p. 145504-4.

56. Pantano, A., D. M. Parks and M.C. Boyce, *Mechanics of deformation of single- and multi-wall carbon nanotubes.* Journal of the Mechanics and Physics of Solids, 2004. **52**(4): p. 789-821.

57. Poncharal, P., Z.L. Wang, D. Ugarte, and W.A. de Heer, *Electrostatic Deflections and Electromechanical Resonances of Carbon Nanotubes.* Science, 1999. **283**(5407): p. 1513-1516.

58. Postma, H.W., T.F. Teepen, Z. Yao, M. Grifoni, and C. Dekker, *Carbon nanotubes single-electron transistors at room temperature.* Science, 2001. **293**(5527): p. 76-79.

59. Qi, H.J., K.B.K. Teo, K.K.S. Lau, M.C. Boyce, W.I. Milne, J. Robertson, and K.K. Gleason, *Determination of mechanical properties of carbon nanotubes and vertically aligned carbon nanotube forests using nanoindentation.* Journal of the Mechanics and Physics of Solids, 2003. **51**: p. 2213-2237.

60. Qian, D., E.C. Dickey, R. Andrews, and T. Rantell, *Load transfer and deformation mechanisms in carbon nanotube-polystyrene composites.* Applied Physics Letters 2000. **76**(20): p. 2868-2870.

61. Qian, D., W.K. Liu, S. Subramoney, and R.S. Ruoff, *Effect of Interlayer*

Potential on Mechanical Deformation of Multiwalled Carbon Nanotubes. Journal of Nanoscience and Nanotechnology, 2003. **3**: p. 185-191.

62. Rappi, A.K., C.J. Casewit, K.S. Colwell, W.A.G. III, and W.M. Skid, *A Full Periodic Table Force Field for Molecular Mechanics and Molecular Dynamics Simulations.* Journal of the American Chemical Society, 1992. **114**: p. 10024-10035.

63. Reiner, J.E., J.M. Wells, R.B. Kishore, C. Pfefferkorn, and K. Helmerson, *Stable and robust polymer nanotubes stretched from polymersomes.* PNAS, 2006. **103**(5): p. 1173-1177.

64. Robertson, D.H., D.W. Brenner and J.W. Mintmire, *Energetics of nanoscale graphitic tubules.* Physical Review B, 1992. **45**(21): p. 12592.

65. Ru, C.Q., *Column buckling of multiwalled carbon nanotubes with interlayer radial displacements.* Physical Review B, 2000. **62**(24): p. 16962.

66. Ru, C.Q., *Effect of van der Waals forces on axial buckling of a double-walled carbon nanotube.* Journal of Applied Physics, 2000. **87**(10): p. 7227-7231.

67. Ru, C.Q., *Effective bending stiffness of carbon nanotubes.* Physical Review B, 2000. **62**(15): p. 9973.

68. Ru, C.Q., *Degraded axial buckling strain of multiwalled carbon nanotubes due to interlayer slips.* Journal of Applied Phisics, 2001. **89**(6): p. 3426-3433.

69. Sanchez-Portal, D., E. Artacho, J.M. Soler, A. Rubio, and P. Ordejon, *Ab initio structural, elastic, and vibrational properties of carbon nanotubes.* Physical Review B, 1999. **59**(19): p. 12678.

70. Schadler, L.S., S.C. Giannaris and P.M. Ajayan, *Load transfer in carbon nanotube epoxy composites.* Applied Physics Letters, 1998. **73**(26): p. 3842-3844.

71. Sears, A. and R.C. Batra, *Macroscopic properties of carbon nanotubes from molecular-mechanics simulations.* Physical Review B (Condensed Matter and Materials Physics), 2004. **69**(23): p. 235406-10.

72. Sears, A. and R.C. Batra, *Buckling of multiwalled carbon nanotubes under axial compression.* Physical Review B (Condensed Matter and Materials Physics), 2006. **73**(8): p. 085410-11.

73. Shen, L. and J. Li, *Transversely isotropic elastic properties of single-walled carbon nanotubes.* Physical Review B (Condensed Matter and Materials Physics), 2004. **69**(4): p. 045414-10.

74. Shen, L. and J. Li, *Equilibrium structure and strain energy of single-walled carbon nanotubes.* Physical Review B (Condensed Matter and Materials Physics), 2005. **71**(16): p. 165427-8.

75. Shen, L. and J. Li, *Transversely isotropic elastic properties of multiwalled carbon nanotubes.* Physical Review B (Condensed Matter and Materials Physics), 2005. **71**(3): p. 035412-10.

76. Shen, L.X. and J. Li, *Effective elastic moduli of composites reinforced by particle or fiber with an inhomogeneous interphase.* International Journal of Solids and Structures, 2003. **40**(1393-1409).

77. Shen, L.-X. and S. Yi, *An effective inclusion model for effective moduli of heterogeneous materials with ellipsoidal inhomogeneities.* International Journal of Solids and Structures, 2001. **38**(32-33): p. 5789-5805.

78. Srivastava, D. and S.T. Barnard. *Molecular Dynamics Simulation of Large-Scale Carbon Nanotubes on a Shared-Memory Architecture*. in *Conference on High Performance Networking and Computing, Proceedings of the 1997 ACM/IEEE conference on Supercomputing (CDROM)*. 1997. San Jose, CA.

79. Star, A., J.F. Stoddart, D. Steuerman, M. Diehl, A. Boukai, E.W. Wong, X. Yang, S. Chung, H. Choi, and J. Heath, *Preparation and properties of polymer-wrapped single-walled carbon nanotubes.* Angewandte Chemie International Edition in English 2001. **40**(9): p. 1721-1725.

80. Stone, A.J. and D.J. Wales, *Theoretical studies of icosahedral C60 and some related species.* Chemical Physics Letters 1986. **128**(5-6): p. 501-503.

81. Tomanek, D., *Mesoscopic origami with graphite: scrolls, nanotubes, peapods.* Physica B: Condensed Matter, 2002. **323**(1-4): p. 86-89.

82. Tomanek, D., G. Overney, H. Miyazaki, S.D. Mahanti, and H.J. Guntherodt, *Theory for the Atomic Force Microscopy of Deformable Surface.* Physical Review Letters, 1989. **63**(8): p. 876-879.

83. Tomanek, D., W. Zhong and E. Krastev, *Stability of multishell fullerenes.* Physical Review B, 1993. **48**(20): p. 15461.

84. Tombler, T.W., C. Zhou, L. Alexseyev, J. Kong, H. Dai, L. Liu, C.S. Jayanthi, M. Tang, and S. Wu, *Reversible Electromechanical Characteristics of Carbon Nanotubes under Local Probe Manipulation.* Nature, 2000. **405**: p. 769-772.

85. Troya, D., S.L. Mielke and G.C. Schatz, *Carbon nanotube fracture – differences between quantum mechanical mechanisms and those of empirical potentials.* Chemical Physics Letters, 2003. **382**: p. 133-141.

86. Wagner, H.D., *Nanotube-polymer adhesion: a mechanics approach.* Chemical Physics Letters, 2002. **361**: p. 57-61.

87. Wagner, H.D., O. Lourie, Y. Feldman, and R. Tenne, *Stress-induced fragmentation of multiwall carbon nanotubes in a polymer matrix.* Applied Physics Letters, 1998. **72**: p. 188-190.

88. Wang, C.Y., C.Q. Ru and A. Mioduchowski, *Axially compressed buckling of*

pressured multiwall carbon nanotubes. International Journal of Solids and Structures, 2004. **40**: p. 3893–3911.

89. Wang, Q. and V.K. Varadan, *Stability analysis of carbon nanotubes via continuum models.* Smart Mater. Struct. , 2005. **14**: p. 281–286.

90. Wang, X., Y.C. Zhang, X.H. Xia, and C.H. Huang, *Effective bending modulus of carbon nanotubes with rippling deformation.* International Journal of Solids and Structures, 2004. **41**: p. 6429–6439.

91. Waters, J.F., L. Riester, M. Jouzi, P.R. Guduru, and J.M. Xu, *Buckling instabilities in multiwalled carbon nanotubes under uniaxial compression.* Applied Physics Letters, 2004. **85**(10): p. 1787-1789.

92. White, C.T., D.H. Robertson and J.W. Mintmire, *Helical and rotational symmetries of nanoscale graphitic tubules.* Physical Review B, 1992. **47**(9): p. 5485-5488.

93. Wise, K. and J. Hinkley. *Molecular dynamics simulations of nanotube-polymer composites.* in *American Physical Society Spring Meeting*. 2001. Seattle, WA.

94. Wong, E.W., P.E. Sheehan and C.M. Lieber, *Nanobeam Mechanics: Elasticity, Strength, and Toughness of Nanorods and Nanotubes.* Science, 1997. **277**(1971-1975).

95. xiao, T., X. Xu and K. Liao, *Characterization of nonlinear elasticity and elastic instability in single-walled carbon nanotubes.* Journal of Applied Physics, 2004. **95**(12): p. 8145-8148.

96. Yakobson, B.I., C.J. Brabec and J. Bernholc, *Nanomechanics of Carbon Tubes: Instabilities beyond Linear Response.* Physical Review Letters, 1996. **76**(14): p. 2511.

`` 97. Yu, M., B. Files, S. Arepalli, and R. Ruoff, *Tensile loading of ropes of single wall carbon nanotubes and their mechanical properties.* Physical Review Letters, 2000. **84**(24): p. 5552-5555.

98. Yu, M.-F., *Fundamental Mechanical Properties of Carbon Nanotubes: Current Understanding and the Related Experimental Studies.* Journal of Engineering Materials and Technology, 2004. **126**: p. 271-278.

99. Yu, M.-F., M.J. Dyer, J. Chen, D. Qian, W.K. Liu, and R.S. Ruoff, *Locked twist in multiwalled carbon-nanotube ribbons.* Physical Review B, 2001. **64**: p. 241403 1-4.

100. Yu, M.-F., O. Lourie, M.J. Dyer, K. Moloni, T.F. Kelly, and R.S. Ruoff, *Strength and Breaking Mechanism of Multiwalled Carbon Nanotubes Under Tensile Load.* Science, 2000. **287**: p. 637-640.

101. Zhang, Y.Y., V.B.C. Tan and C.M. Wang, *Effect of chirality on buckling behavior of single-walled carbon nanotubes.* Journal of Applied Phisics, 2006. **100**: p. 074304 1-6.

102. Zhang, Y.Y., C.M. Wang and V.B.C. Tan, *Buckling of Multiwalled Carbon Nanotubes Using Timoshenko Beam Theory.* Journal of Engineering Mechanics, 2006. **132**(9): p. 952-958.

103. Zhao, Y.X. and I.L. Spain, *X-ray diffraction data for graphite to 20 GPa.* Physical Review B, 1989. **40**(2): p. 993.